BEILSTEIN JOURNAL OF NANOTECHNOLOGY

Innovative nanomaterials for next-generation bio- and chemosensing

Edited by Thanh-Danh Nguyen, Duong Tuan Quang and Olga Guliy

Generated on 18 November 2026, 22:13

Imprint

Beilstein Journal of Nanotechnology
www.bjnano.org
ISSN 2190-4286
Email: journals-support@beilstein-institut.de

The *Beilstein Journal of Nanotechnology* is published by the Beilstein-Institut zur Förderung der Chemischen Wissenschaften.

Beilstein-Institut zur Förderung der Chemischen Wissenschaften
Trakehner Straße 7–9
60487 Frankfurt am Main
Germany
www.beilstein-institut.de

The copyright to this document as a whole, which is published in the *Beilstein Journal of Nanotechnology*, is held by the Beilstein-Institut zur Förderung der Chemischen Wissenschaften. The copyright to the individual articles in this document is held by the respective authors, subject to a Creative Commons Attribution license.

BEILSTEIN JOURNAL OF NANOTECHNOLOGY

Electrochemical sensing of sildenafil in pharmaceutical formulations using an (S,N)-doped reduced graphene oxide-modified electrode

Nguyen Quang Man[1], Ngo Thi Thanh Xuan[*2,3], Vo Thi Khanh Ly[1], Le Van Thanh Son[4], Le Duc Anh[5], Le Thi Hong Phong[6], Nguyen Hai Phong[2], Pham Khac Lieu[2], Le Lam Son[*2] and Dinh Quang Khieu[*2]

Full Research Paper

Open Access

Address:
[1]University of Medicine and Pharmacy, Hue University, 530000, Vietnam, [2]University of Sciences, Hue University, 530000, Vietnam, [3]Drug, Cosmetic, and Food Quality Control Center of Hue city, 530000, Vietnam, [4]University of Education and Science, The University of Danang, 550000, Vietnam, [5]Viet Nam National Institute of Occupational Safety and Health, Hanoi, Vietnam and [6]Institute of Materials Sciences, Vietnam Academy of Science and Technology, 18 Hoang Quoc Viet, Cau Giay, Hanoi City, 100000, Vietnam

Email:
Ngo Thi Thanh Xuan* - thanhxuanknh@gmail.com;
Le Lam Son* - lelamson@hueuni.edu.vn;
Dinh Quang Khieu* - dqkhieu@hueuni.edu.vn

* Corresponding author

Keywords:
differential pulse voltammetry; electrode modifier; rGO; (S,N)-rGO; sildenafil

Beilstein J. Nanotechnol. **2026,** *17,* 1087–1102.
https://doi.org/10.3762/bjnano.17.74

Received: 20 May 2026
Accepted: 22 July 2026
Published: 11 August 2026

This article is part of the thematic issue "Innovative nanomaterials for next-generation bio- and chemosensing".

Guest Editor: O. Guliy



© 2026 Man et al.; licensee Beilstein-Institut.
License and terms: see end of document.

Abstract

In this work, (S,N)-co-doped reduced graphene oxide ((S,N)-rGO) was successfully synthesized via thermal treatment and thoroughly characterized by X-ray diffraction, high-resolution transmission electron microscopy, elemental mapping, photoluminescence, and Raman spectroscopy, confirming the successful incorporation of nitrogen and sulfur into the graphene framework. The obtained (S,N)-rGO was used to modify a glassy carbon electrode for the electrochemical determination of sildenafil (SDN). The modified electrode exhibited enhanced electrocatalytic activity toward SDN oxidation, providing a well-defined current response. Under optimized conditions, the sensor showed a good linear relationship between peak current and SDN concentration in the range of 0.25–4.98 μM, with a low limit of detection of 0.24 μM and a limit of quantification of 0.78 μM. The proposed sensor demonstrated satisfactory repeatability, reproducibility, and stability, as well as good selectivity in the presence of potential interfering substances. The applicability of the method was validated by the determination of SDN in pharmaceutical samples. The results were in good agreement with those from high-performance liquid chromatography, indicating that the proposed electrochemical method is reliable and suitable for practical analysis.

Introduction

Sildenafil (SDN) is a widely prescribed phosphodiesterase type 5 (PDE-5) inhibitor used for the treatment of erectile dysfunction and pulmonary arterial hypertension. Its pharmacological activity is based on the selective inhibition of PDE-5, which increases the intracellular level of cyclic guanosine monophosphate (cGMP), resulting in smooth muscle relaxation and vasodilation. Phosphodiesterase-5 inhibitors, including SDN, are considered first-line therapeutic agents and have demonstrated significant efficacy in improving vascular function and clinical outcomes [1]. Furthermore, these agents enhance nitric oxide-mediated signaling pathways, thereby promoting increased blood flow in vascular tissues [2]. The widespread clinical use of SDN has led to a substantial increase in global consumption, which is accompanied by growing concerns regarding its misuse and illegal adulteration. Recent studies have reported that PDE-5 inhibitors are frequently detected as undeclared active ingredients in dietary supplements and counterfeit pharmaceutical products marketed as "natural" remedies [3]. This situation poses a serious public health risk as such products often evade regulatory control and may contain unpredictable or excessive dosages.

To date, various analytical techniques have been developed for the determination of SDN. Conventional methods such as gas chromatography/mass spectrometry (GC/MS) [4], liquid chromatography–tandem mass spectrometry (LC–MS/MS) [5], and high-performance liquid chromatography (HPLC) [6,7] are widely employed because of their high accuracy and sensitivity. In addition, advanced spectroscopic and hybrid approaches, including surface-enhanced Raman scattering (SERS) using Ag/UiO-66-decorated porous structures [8], thin-layer chromatography coupled with UV–SERS detection (TLC–UV–SERS) [9], dual-labeled probe time-resolved fluorescence immunochromatography assay [10], and fluorescence-based methods [11], have also been reported. Despite their excellent analytical performance, these techniques generally require sophisticated instrumentation, complex sample preparation, and relatively long analysis time.

In this context, electrochemical sensing has emerged as a promising alternative for SDN determination due to its inherent advantages, including operational simplicity, rapid response, low cost, and high sensitivity [12,13]. These features make electrochemical methods particularly suitable for on-site monitoring and routine analysis [14,15]. Importantly, the electrochemical oxidation of SDN can be effectively enhanced by tailoring the electrode surface with functional nanomaterials, thereby improving both sensitivity and selectivity.

Among various nanomaterials, graphene-based materials, especially reduced graphene oxide (rGO), have attracted considerable attention as electrode modifiers due to their excellent electrical conductivity, large specific surface area, and favorable electrocatalytic properties [16,17]. However, pristine rGO still suffers from a limited number of active sites and insufficient selectivity toward specific analytes. To overcome these limitations, heteroatom doping has been proposed as an effective strategy to modulate the electronic structure and enhance catalytic activity [18,19]. In particular, nitrogen and sulfur co-doping has been demonstrated to significantly improve electrochemical performance by introducing defects, redistributing charge density, and facilitating electron transfer processes [20,21].

In our previous study [22], nitrogen- and sulfur-doped reduced graphene oxide ((S,N)-rGO) was explored as a potential electrode modifier for the electrochemical detection of SDN, showing promising electrocatalytic behavior. However, that work was mainly limited to a proof-of-concept study and lacked a systematic investigation of the sensing mechanism, optimization of experimental conditions, and a comprehensive evaluation of analytical performance. Although various electrochemical sensors have been reported for SDN determination, many of them rely on multicomponent nanocomposites, noble-metal nanoparticles, or relatively complicated fabrication procedures. In contrast, the proposed (S,N)-rGO-modified electrode is prepared through a simple and facile synthesis strategy while providing enhanced electrocatalytic activity arising from the synergistic effects of nitrogen and sulfur co-doping. Together with its satisfactory analytical performance and successful application to pharmaceutical formulations, these features constitute the main novelty and practical advantage of the present work. To address these limitations, the present study builds on our previous findings and develops a more systematic electrochemical sensing strategy. In this work, (S,N)-co-doped reduced graphene oxide ((S,N)-rGO) was synthesized via a facile thermal treatment using ammonium persulfate as a dual heteroatom precursor. Incorporating nitrogen and sulfur heteroatoms is expected to generate abundant active sites, enhance electron transfer kinetics, and improve adsorption affinity for SDN molecules. The synthesized material was used to modify a glassy carbon electrode (GCE) for electrochemical detection. The fabricated (S,N)-rGO/GCE sensor exhibited significantly enhanced electrocatalytic activity toward the oxidation of SDN, resulting in improved sensitivity and selectivity compared with the bare electrode. The effects of key experimental parameters, including pH, scan rate, and accumulation conditions, were systematically investigated to elucidate the sensing mechanism. Furthermore, the analytical performance of the proposed sensor

was thoroughly evaluated in terms of linear range, limit of detection, reproducibility, and stability. Finally, the practical applicability of the method was demonstrated by determining SDN in real pharmaceutical samples, with satisfactory accuracy and recovery.

Experimental

Chemicals

Graphite powder, phosphoric acid (H_3PO_4, 85%), sulfuric acid (H_2SO_4, 98%), hydrochloric acid (HCl, 37%), potassium permanganate ($KMnO_4$, 99%), thiourea (CH_4N_2S, 99%), and hydrogen peroxide (H_2O_2, 30%) were obtained from Merck. Boric acid (H_3BO_3, 99.5%), phosphoric acid (H_3PO_4, 85%), acetic acid (CH_3COOH, 99.8%), and sodium hydroxide (NaOH, 98%) were purchased from Sigma-Aldrich and used for the preparation of Britton–Robinson (BR) buffer solutions with various pH values for electrochemical measurements. SDN citrate standard ($C_{28}H_{38}N_6O_{11}S$, 99%) was supplied by the National Institute of Drug Quality Control, Vietnam. All chemicals and reagents used throughout the study were of analytical grade and utilized without any further purification.

Apparatus

A conventional three-electrode system was used, consisting of a modified GCE as the working electrode, a platinum wire as the counter electrode, and an Ag/AgCl electrode as the reference electrode (CPA–HH5 Computerized Polarography Analyzer, Vietnam). Morphological and structural characterizations were performed using transmission electron microscopy (TEM) and energy-dispersive X-ray spectroscopy (EDX) mapping (JEM-2100, Jeol-Japan) at 200 kV, X-ray diffraction (XRD) (Bruker D8 Advance, Germany), Raman spectroscopy (XploRA™ PLUS, Horiba, Japan), FTIR (Shimadzu Prestige-21, Japan), and photoluminescence (PL) (Horiba Fluorolog 3 FL3-22 fluorometer).

Synthesis of graphene oxide

Graphene oxide (GO) was synthesized following a modified procedure based on the method reported by Diego C. Marcano and coworkers [23]. Briefly, 3 g of graphite powder was gradually added to a mixed acid solution containing 360 mL of concentrated H_2SO_4 and 40 mL of concentrated H_3PO_4 under continuous stirring. Subsequently, 18 g of $KMnO_4$ was slowly introduced into the mixture, resulting in a mildly exothermic reaction. The suspension was maintained under stirring for 72 h to allow for complete oxidation. Afterward, 17 mL of 30% H_2O_2 was added dropwise to terminate the reaction, and the mixture was allowed to cool to room temperature. The resulting product was separated by centrifugation at 5000 rpm for 15 min, and the supernatant was discarded to obtain a brownish-yellow solid. The solid was washed several times with 0.1 M HCl solution and deionized water to remove residual ions and impurities, followed by centrifugation. The purified material was then dried at 60 °C for 48 h to yield graphite oxide. This product was subsequently exfoliated by ultrasonic treatment in distilled water for 4 h. After centrifugation and drying at 60 °C for an additional 48 h, GO was obtained as a black solid.

Synthesis of (S,N)-doped graphene oxide ((S,N)-GO)

The synthesis of nitrogen and sulfur co-doped graphene oxide ((S,N)-GO) was carried out using a procedure similar to that described above. The key difference lies in the oxidation stage, where 1.5 g of thiourea was introduced into the reaction mixture immediately after the addition of $KMnO_4$, serving as a heteroatom dopant source.

Synthesis of (S,N)-doped reduced graphene oxide

To obtain reduced (S,N)-doped graphene oxide ((S,N)-rGO), 0.3 g of (S,N)-GO was dispersed in a mixture of 50 mL distilled water and 30 mL ethanol. The suspension was ultrasonicated for 60 min to ensure uniform dispersion, then transferred into a Teflon-lined autoclave. The hydrothermal reduction was conducted at 180 °C for 12 h. After naturally cooling to room temperature, the resulting black solid was collected by centrifugation, washed thoroughly with distilled water, and dried at 80 °C for 24 h. The final product was ground into a fine powder to obtain (S,N)-rGO.

Fabrication of the (S,N)-rGO-modified electrode

Prior to modification, the GCE surface was polished with an alumina slurry, thoroughly rinsed with deionized water, and sonicated sequentially in ethanol and water. A suspension of (S,N)-rGO (1 mg·mL^{-1}) was prepared by dispersing the material in water with ultrasonication. A defined volume of the suspension (5 µL) was drop-cast onto the cleaned GCE surface and dried at room temperature (≈30 min) to obtain the (S,N)-rGO/GCE.

Electrochemical measurements

The electrochemical behavior of SDN was investigated using cyclic voltammetry (CV) and differential pulse voltammetry (DPV) in a Britton–Robinson buffer solution at various pH values. Key experimental parameters, including accumulation potential, accumulation time, pulse amplitude, and scan rate, were optimized to achieve the best analytical performance. Calibration curves were constructed by measuring the peak current response at different concentrations of SDN. The limit of detection (LOD) and the limit of quantification (LOQ) were calcu-

lated based on the residual standard deviation of the calibration curve and its slope.

Sample preparation and analysis

Sample preparation

Ten SDN tablets were accurately weighed and the average tablet mass was determined. The tablets were then finely ground to obtain a homogeneous powder. An accurately weighed portion of the powder, equivalent to one tablet, was transferred into a 100 mL volumetric flask. Approximately 50 mL of distilled water was added, and the mixture was sonicated for 30 min to ensure complete extraction of SDN. The solution was then diluted to the mark with distilled water, thoroughly mixed, and filtered to obtain the stock sample solution. The obtained solution was further diluted with distilled water to an appropriate concentration depending on the SDN content in the pharmaceutical formulation (solution 1). An aliquot of solution 1 was then diluted with distilled water and Britton–Robinson buffer (0.1 M, pH 4.0) in the electrochemical cell to obtain a final SDN concentration of approximately 4.2 μM. The SDN content was determined using DPV with the standard addition technique.

Recovery study

For recovery evaluation, the prepared sample solution was diluted under the same conditions as described above. Subsequently, 20 μL of a 0.001 M SDN standard solution was added into a 20 mL electrochemical cell. The total SDN concentration was determined by DPV using the standard addition method. The original SDN content in the sample was subtracted, and the recovery was calculated by comparing the measured increase with the known added amount. All measurements were performed in triplicate. The recovery (%) was calculated according to the following equation:

$$\text{Recovery}(\%) = \frac{C_{\text{found}} - C_{\text{original}}}{C_{\text{added}}} \times 100$$

The relative standard deviation (RSD, %) was used to evaluate precision:

$$\text{RSD}(\%) = \frac{\text{SD}}{\text{mean}} \times 100$$

Results and Discussion

Characterization of materials

Figure 1 presents the characterization results for the obtained materials. The GO sample exhibits a characteristic diffraction peak at around 2θ ≈ 8.7°, corresponding to the (001) plane, indicating the presence of oxygen-containing functional groups and enlarged interlayer spacing [24]. After (S,N)-doping, the peak becomes broader and slightly shifted, suggesting partial disruption of the layered structure. For (S,N)-rGO, the disappearance of the GO peak and the emergence of a broad peak at ≈24.7° (002 plane) confirm the successful reduction process and partial restoration of graphitic domains [24]. The textural parameters in Table 1 and Figure 1b reveal a clear evolution of pore structure after doping and reduction. Pristine GO exhibits a very low BET surface area (6.93 $m^2 \cdot g^{-1}$) with no detectable microporosity, indicating a highly stacked structure with limited accessible surface. Upon (S,N)-co-doping, (S,N)-GO shows a significant increase in surface area (63.81 $m^2 \cdot g^{-1}$), mainly contributed by mesopores, suggesting that the introduction of heteroatoms and gas evolution during oxidation promotes exfoliation and pore formation. After reduction, rGO presents a hierarchical pore structure with both micropores (16.5 $m^2 \cdot g^{-1}$) and mesopores (43.8 $m^2 \cdot g^{-1}$). The formation of micropores can be attributed to the removal of oxygen-containing functional groups, which generates vacancy defects and creates nanoscale pores within the graphene sheets. Meanwhile, mesopores originate from the partial restacking and wrinkling of graphene layers. In contrast, (S,N)-rGO shows reduced microporous (13.1 $m^2 \cdot g^{-1}$) and mesoporous (29.6 $m^2 \cdot g^{-1}$) contributions compared to rGO. This decrease may result from structural rearrangement or partial pore collapse during hydrothermal treatment, as well as the occupation of pore sites by doped nitrogen and sulfur species.

The FTIR spectra (Figure 1c) confirm the successful oxidation and subsequent modification of GO. The broad band at ≈3400 cm^{-1} corresponds to O–H stretching vibrations, while peaks at ≈1728 cm^{-1} (C=O), ≈1619 cm^{-1} (C=C), and 1224–1053 cm^{-1} (C–O) are characteristic of oxygen-containing functional groups in GO [25]. After doping and reduction, the intensity of oxygen-related peaks decreases, indicating partial removal of oxygen functionalities [24]. New features observed at ≈1555 cm^{-1} and ≈1159 cm^{-1} suggest the incorporation of nitrogen- and sulfur-containing groups, confirming successful heteroatom. The Raman spectra (Figure 1d) display the typical D and G bands of graphene-based materials [26]. The I_D/I_G ratio increases from 0.82 (GO) to 1.21 ((S,N)-rGO), indicating an increase in structural defects and disorder after doping and reduction [27]. This increase is commonly attributed to the formation of smaller sp^2 domains and the introduction of defects by N and S heteroatoms. Such defects are beneficial for electrochemical applications, as they enhance electron transfer and provide more active sites. The combined results confirm that (S,N)-co-doping and reduction effectively modify the structural, textural, and electronic properties of GO, leading to enhanced electrochemical activity. These structural and surface modifications are expected to significantly improve the electrochemical performance of the (S,N)-rGO-modified electrode.

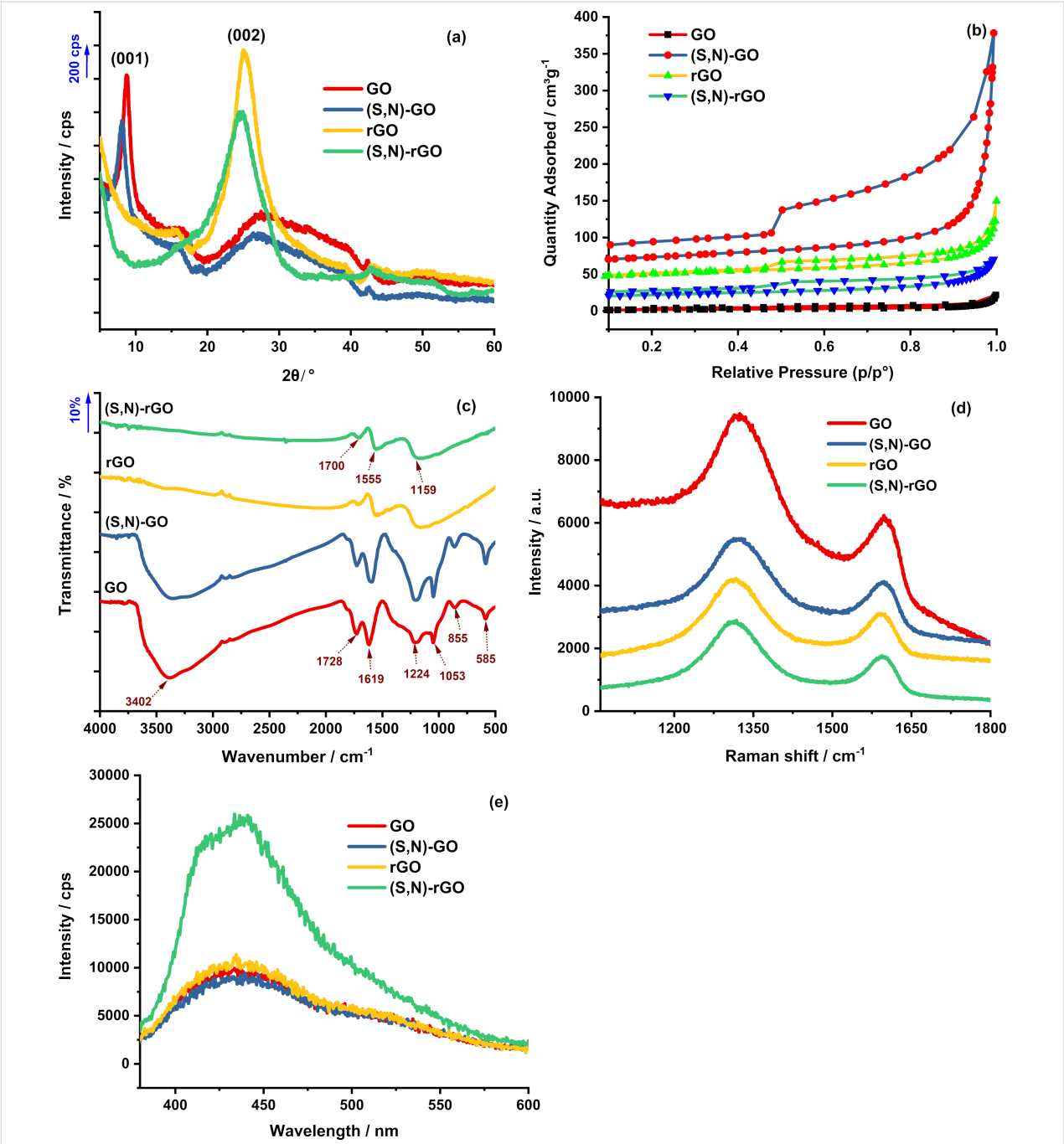


Figure 1: (a) XRD patterns, (b) nitrogen adsorption/desorption isotherms, (c) FTIR spectra, (d) Raman spectra, and (e) photoluminescence (PL) spectra of GO, (S,N)-GO, rGO and (S,N)-rGO.

Table 1: Textural properties and Raman intensity ratios (I_D/I_G) of GO, (S,N)-GO, rGO, and (S,N)-rGO.

Sample	BET ($m^2 \cdot g^{-1}$)	Micropores ($m^2 \cdot g^{-1}$)	Mesopores ($m^2 \cdot g^{-1}$)	I_D/I_G
GO	6.93	–	6.9	0.82
(S,N)-GO	63.81	–	63.8	0.98
rGO	60.31	16.5	43.8	1.05
(S,N)-rGO	42.63	13.1	29.6	1.21

The PL spectra of GO, (S,N)-GO, rGO, and (S,N)-rGO are shown in Figure 1e. All samples exhibit a broad emission band centered around 440–460 nm, which is commonly attributed to radiative recombination associated with oxygen-containing functional groups and defect states in graphene oxide-based materials. GO exhibits the highest PL intensity, indicating a high density of oxygenated defects that act as recombination centers for electron–hole pairs. After reduction and heteroatom doping, the PL intensity decreases significantly, especially for (S,N)-rGO. This quenching effect suggests the partial restoration of the conjugated sp^2 carbon network and improved charge mobility after removal of oxygen-containing groups. The reduced PL intensity of (S,N)-rGO indicates a lower recombination rate of charge carriers and more efficient electron transport capability. In addition, the incorporation of nitrogen and sulfur atoms can modify the electronic structure of graphene and introduce new electronic states, thereby facilitating charge-transfer processes. The PL results therefore further confirm the successful reduction and heteroatom functionalization of GO, in agreement with the XRD, FTIR, BET, and Raman analyses.

High-resolution transmission electron microscopy (HRTEM) images of (S,N)-GO and (S,N)-rGO are presented in Figure 2a and Figure 2b, respectively. The (S,N)-GO sample exhibits thin, transparent, and relatively smooth layered nanosheets with a typical wrinkled morphology characteristic of graphene oxide-based materials. The translucent appearance indicates the formation of few-layer graphene sheets with high exfoliation degree. After the reduction process, the morphology of (S,N)-rGO becomes more crumpled and corrugated, accompanied by partial restacking of graphene layers. The increased wrinkling and folding observed in Figure 2b can be attributed to the removal of oxygen-containing functional groups during reduction, which induces structural distortion and decreases electrostatic repulsion between graphene sheets. Such morphological changes are commonly observed in reduced graphene materials and indicate the partial restoration of the conjugated carbon network. Moreover, the highly wrinkled and defective structure of (S,N)-rGO is advantageous for electrochemical applications because it can prevent severe agglomeration of graphene sheets, expose more electroactive surface area, and facilitate electrolyte diffusion. The formation of folded nanosheet structures also creates abundant edge-plane-like defects and active sites, which are beneficial for electron-transfer reactions and analyte adsorption during electrochemical sensing.

The elemental mapping images and EDX spectrum of (S,N)-rGO are presented in Figure 3. The mapping results reveal the distribution of C, O, N, and S throughout the graphene framework, confirming the successful heteroatom functionalization of the reduced graphene oxide sheets. The strong carbon signal originates from the graphene backbone, while the oxygen signal indicates that a small amount of residual oxygen-containing functional groups remains after the reduction process. Notably, although the quantitative EDX analysis shows an extremely low nitrogen content (close to 0 atom %), the elemental mapping image still exhibits detectable N-related signals distributed over the graphene surface. This discrepancy can be attributed to the inherent limitation of EDX spectroscopy in quantitatively detecting light elements at ultralow concentrations. Because

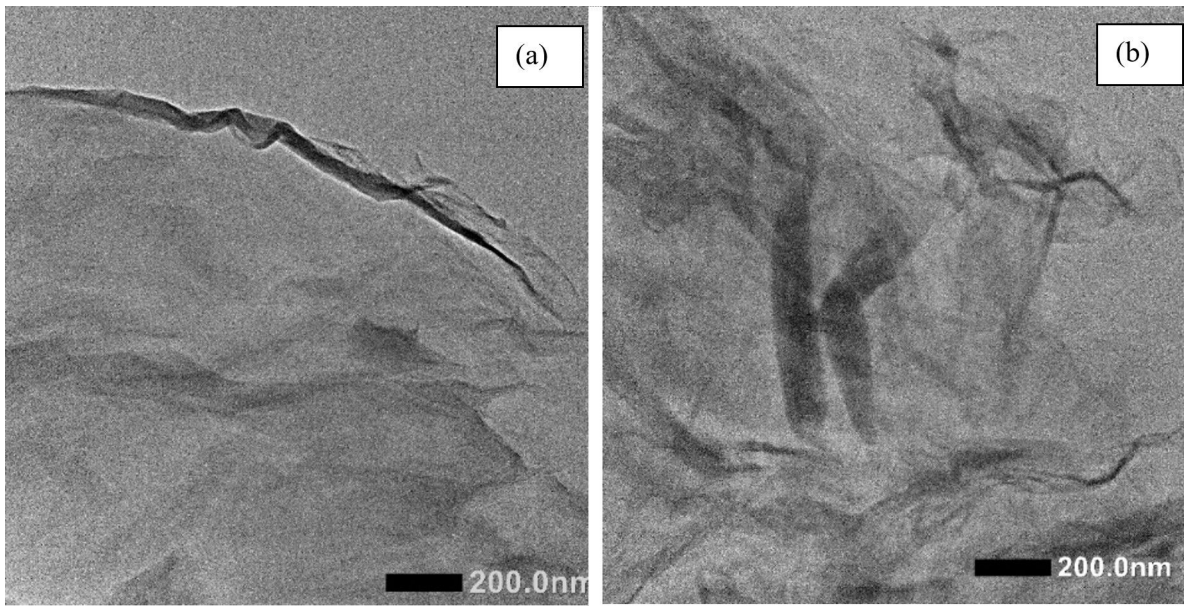


Figure 2: HRTEM observation of (S,N)-GO (a) and (S,N)-rGO (b).

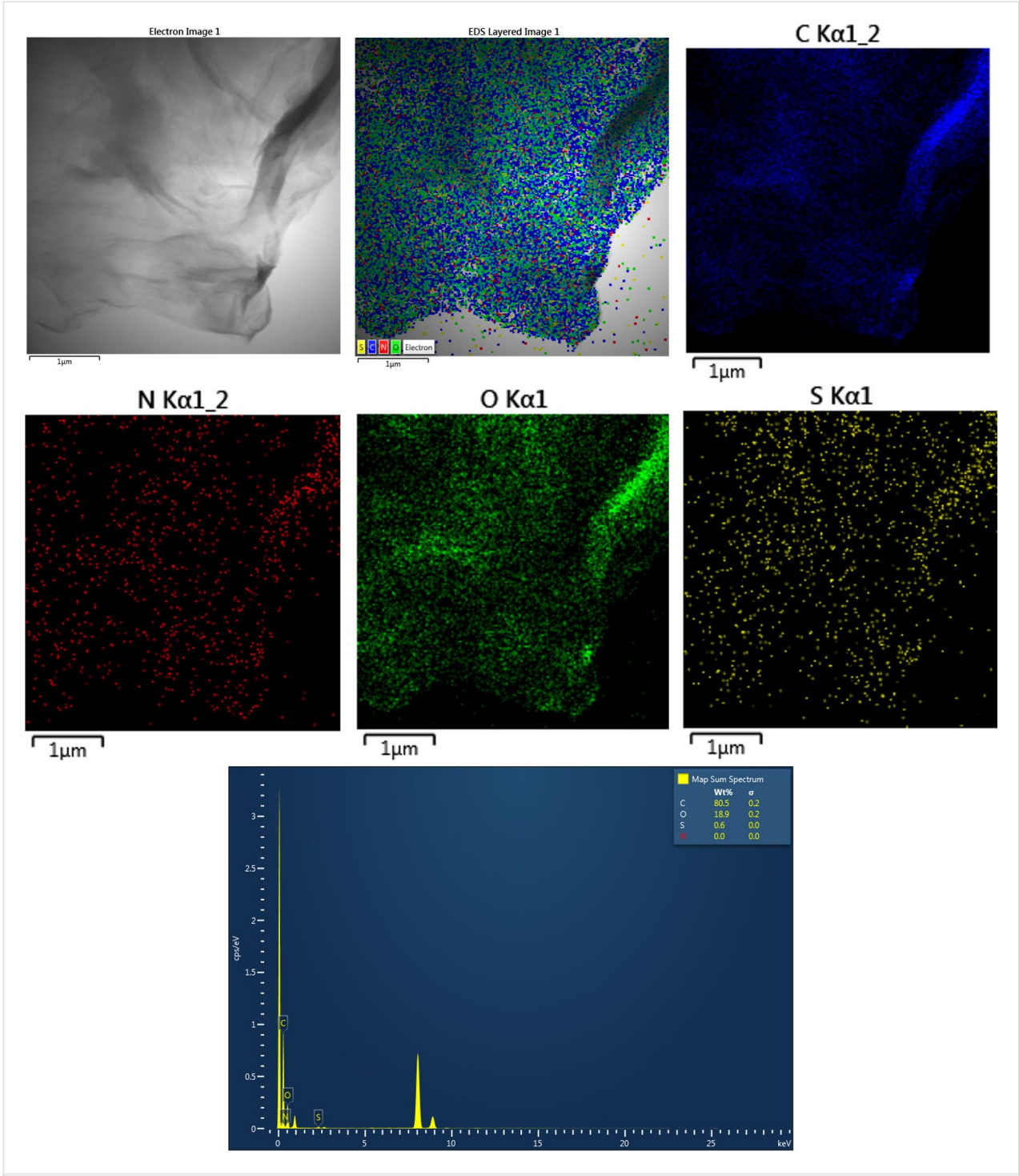


Figure 3: EDX mapping of (S,N)-rGO.

nitrogen has a low atomic number and weak X-ray emission intensity, its signal can easily fall below the reliable quantitative detection threshold, particularly in carbon-rich materials such as graphene derivatives [28,29]. Nevertheless, the mapping image qualitatively suggests the presence of trace nitrogen species distributed over the graphene surface. However, owing to the limited sensitivity of EDX for the quantitative analysis of light elements, particularly nitrogen in carbon-rich materials, this observation should be regarded as qualitative evidence rather than definitive proof of nitrogen incorporation. Therefore, the presence of nitrogen-containing species is suggested but cannot be conclusively confirmed by EDX alone. In contrast, sulfur

signals are more clearly observed and uniformly distributed across the graphene sheets, indicating more effective sulfur incorporation into the carbon framework.

Determination of SDN using a (S,N)-rGO modified electrode

Electrochemical behavior of SDN on different electrode

The electrochemical responses of SDN at different electrodes are presented in Figure 4a. The bare GCE exhibits a relatively weak oxidation current, indicating limited electron transfer kinetics. Upon modification with GO, the peak current increases slightly due to the larger surface area and presence of oxygen-containing functional groups. A more pronounced enhancement is observed for the (S,N)-GO/GCE, suggesting that heteroatom doping improves the electrical conductivity and introduces additional active sites for electron transfer. Notably, the (S,N)-rGO/GCE shows the highest current response, which can be attributed to the synergistic effect of (S,N)-co-doping and reduction. The reduction process restores the π-conjugated structure, facilitating faster electron transfer, while heteroatoms create defect sites that enhance electrocatalytic activity. As summarized in Figure 2b, the peak current increases in the order: GCE < GO/GCE < (S,N)-GO/GCE < rGO < (S,N)-rGO/GCE, confirming that the (S,N)-rGO-modified electrode exhibits the best electrochemical performance toward SDN detection.

The enhanced electrochemical response of the (S,N)-rGO/GCE can be attributed to the synergistic effects of reduced graphene oxide and nitrogen/sulfur heteroatom doping. The hydrothermal reduction restores the conjugated sp^2 carbon network, resulting in improved electrical conductivity and accelerated electron-transfer kinetics. Meanwhile, the incorporation of nitrogen and sulfur atoms introduces structural defects and heterogeneous electronic states, which act as additional electroactive sites for the oxidation of SDN. Nitrogen dopants increase the electron density of adjacent carbon atoms, whereas sulfur dopants induce charge polarization and further modulate the local electronic structure. These heteroatom-induced effects facilitate charge transfer across the electrode/electrolyte interface and lower the activation energy for the oxidation reaction. Furthermore, the aromatic structure of SDN can interact with the π-conjugated graphene surface through π–π stacking interactions, while residual oxygen-containing functional groups and heteroatom sites may promote adsorption through hydrogen bonding and electrostatic interactions. Consequently, the combination of improved conductivity, increased density of active sites, and enhanced adsorption affinity results in the significantly higher oxidation current observed at the (S,N)-rGO-modified electrode.

Effect of the pH value

The effect of pH on the electrochemical response of SDN at the (S,N)-rGO/GCE was investigated over the pH range of 2.0–8.0 (Figure 5a). The oxidation peak current initially increased with increasing pH, reached a maximum at pH 4.0, and then gradually decreased at higher pH values (Figure 5b). The oxidation peak current initially increased with increasing pH, reached a maximum at pH 4.0, and then gradually decreased at higher pH values (Figure 5b). During the pH study, only a single oxidation peak of SDN was observed in the pH range of 2.0–5.0. However, at pH 6.0–8.0, an additional oxidation peak appeared adjacent to the main SDN oxidation peak, which is likely associated with the formation of oxidation and/or degradation prod-

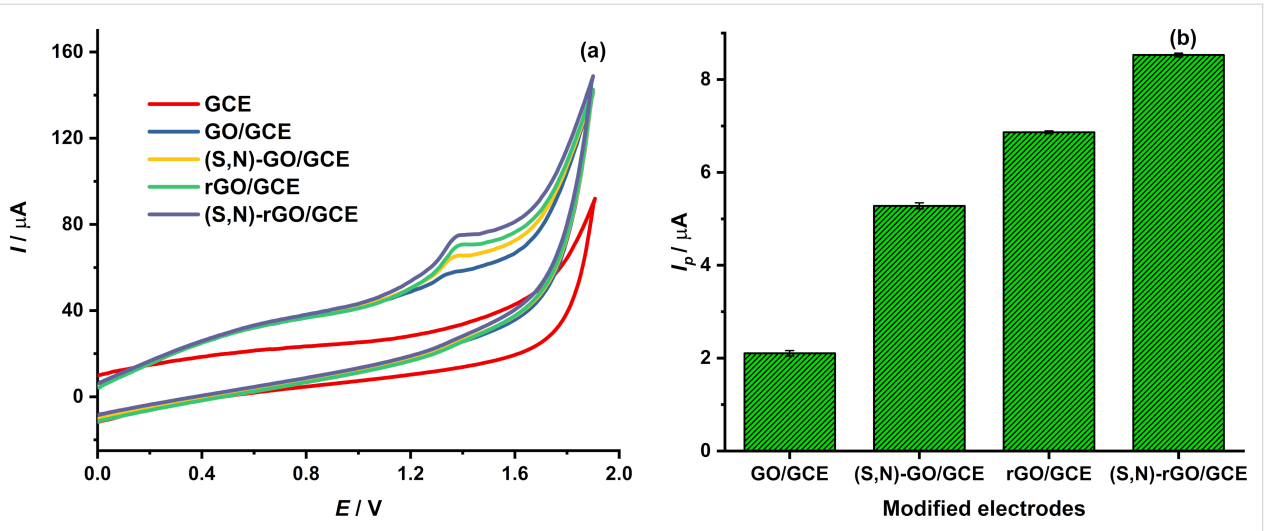


Figure 4: (a) Cyclic voltammograms (CVs) recorded at different electrodes (GCE, GO/GCE, (S,N)-GO/GCE, rGO/GCE and (S,N)-rGO/GCE) in 0.1 M BR buffer (pH 3.0) containing 20 μM SDN at a scan rate of 0.2 $V \cdot s^{-1}$; (b) corresponding peak currents obtained at different electrodes (n = 3).

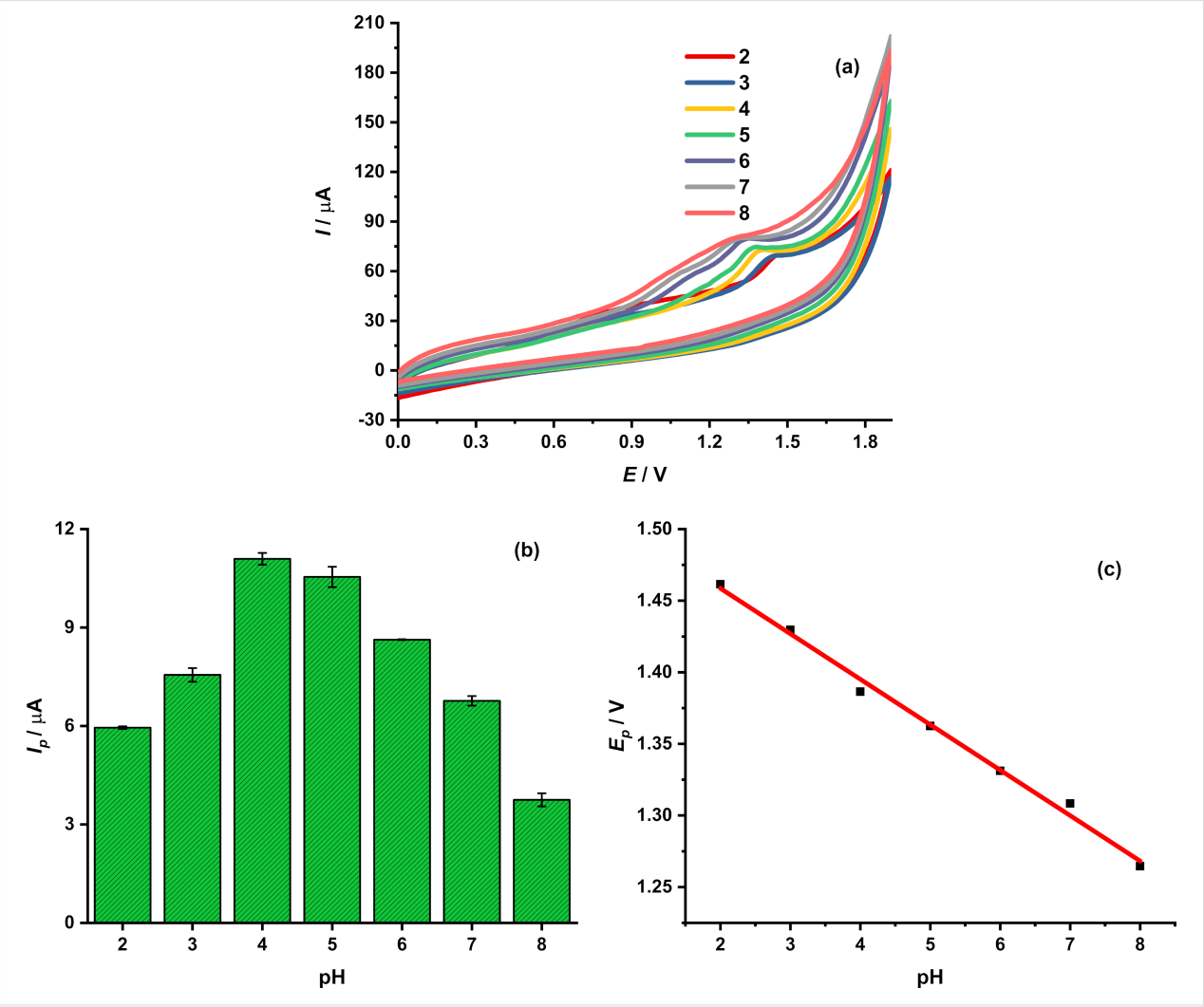


Figure 5: (a) CVs of (S,N)-rGO/GCE in 0.1 M Britton–Robinson buffer at different pH values (2.0–8.0) containing 20 μM SDN at a scan rate of 0.2 V·s^{-1}; (b) variation of anodic peak current with pH; (c) dependence of peak potential (E_p) on pH.

ucts. Consequently, the CV curves in Figure 5a represent the overall anodic response, whereas the quantitative values shown in Figure 5b were obtained by integrating only the main SDN oxidation peak using Origin software. The contribution of the additional oxidation peak was intentionally excluded from the quantitative analysis. Therefore, although the overall anodic current appears higher at pH 6.0–8.0, the current corresponding solely to the main SDN oxidation peak decreases, resulting in lower peak currents than those observed at pH 4.0 and 5.0. These results indicate that proton participation plays an important role in the electrochemical oxidation of SDN, and therefore pH 4.0 was selected as the optimum supporting electrolyte for subsequent experiments.

As shown in Figure 5c, the oxidation peak potential shifted linearly toward less positive values with increasing pH, following the equation:

$$E_{SDN} = (1.5221 \pm 0.0061) + (-0.0317 \pm 0.0011)\,\text{pH};$$
$$r^2 = 0.9937.$$

The slope of 0.0317 V·pH^{-1} is close to half of the theoretical Nernstian value of 0.059 V·pH^{-1}, suggesting that the number of protons involved in the electrochemical oxidation process is lower than the number of transferred electrons. Based on the Nernst relationship, the proton-to-electron ratio can be estimated to be approximately 0.5, indicating that the number of electrons participating in the oxidation process is likely twice that of protons. However, it should be noted that the reported pH dependence for SDN oxidation varies considerably in the literature. A study [30] has reported slopes close to the theoretical Nernstian value of 0.059 V·pH^{-1}, indicating an equal number of protons and electrons participating in the reaction, where-

as other [31] has described slopes near half of this theoretical value, corresponding to a proton-to-electron ratio of approximately 1:2. These discrepancies may arise from differences in electrode materials, surface interactions, and oxidation mechanisms. In the present study, the observed deviation may be attributed to the strong electronic interaction between SDN and the conductive (S,N)-rGO surface, together with possible adsorption effects and multistep oxidation pathways occurring at the electrode interface.

Scan rate effect

The effect of scan rate on the electrochemical behavior of SDN at the (S,N)-rGO/GCE was investigated in the range of 0.07–0.40·V s^{-1} (Figure 6a). The oxidation peak current increased with increasing scan rate, indicating enhanced mass transport toward the electrode surface. As shown in Figure 6b, the peak current exhibited a good linear relationship with the square root of scan rate:

$$I_{SDN} = (0.0802 \pm 0.1463) + (18.0462 \pm 0.3175)\nu^{1/2};$$
$$r^2 = 0.9978.$$

This result indicates that the electrochemical oxidation process is predominantly diffusion-controlled. Further insight was obtained from the log–log relationship (Figure 6c):

$$\log I_{SDN} = (1.2554 \pm 0.0056) + (0.4921 \pm 0.0070)\log \nu;$$
$$r^2 = 0.9986.$$

The slope value (≈0.49) is very close to the theoretical value of 0.5 expected for a diffusion-controlled process, further confirming that diffusion is the dominant transport mechanism. Nevertheless, considering the high surface area and π-electron-rich structure of (S,N)-rGO, surface interaction and partial adsorption of SDN on the electrode surface may also contribute to the overall electrochemical response.

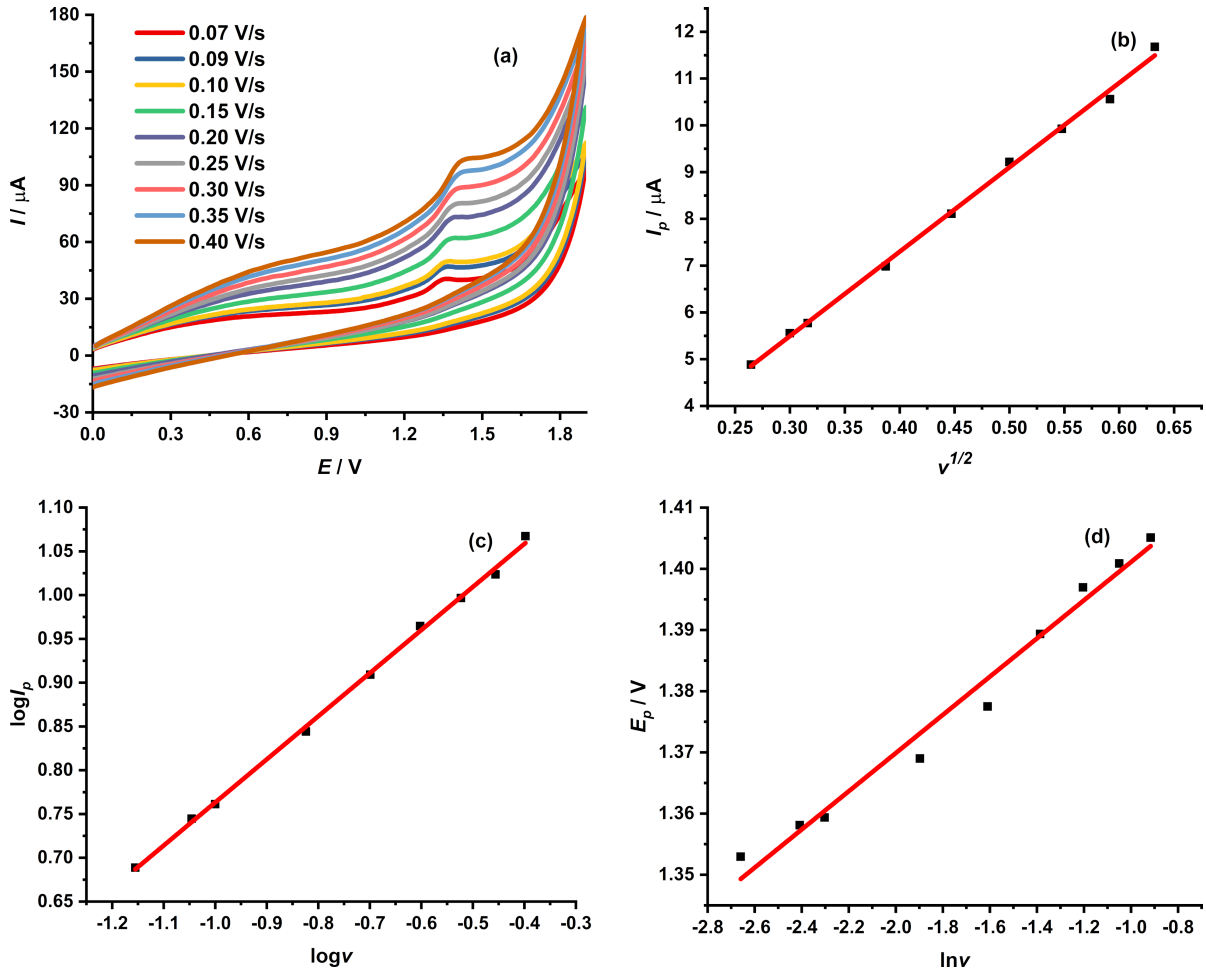


Figure 6: (a) CVs of (S,N)-rGO/GCE in 0.1 M Britton–Robinson buffer (pH 4.0) containing 20 μM SDN at different scan rates (0.07–0.40 V s^{-1}); (b) linear relationship between peak current (I_p) and the square root of scan rate ($v^{1/2}$); (c) linear plot of log I_p versus log v; (d) dependence of peak potential (E_p) on ln v.

For an irreversible electrochemical process, the relationship between peak potential and scan rate is described by the Laviron equation (Figure 6d):

$$E_{SDN} = (1.4323 \pm 0.0030) + (0.0312 \pm 0.00166) \ln \nu;$$
$$r^2 = 0.9807.$$

According to Laviron theory [32]:

$$\text{slope} = RT/\alpha nF$$

(R: molar gas constant (8.314 J·mol^{-1}·K^{-1}); T: the absolute temperature (K); α: the electron-transfer coefficient; n: the number of transferred electrons; F: the Faraday constant (96485 C·mol^{-1}). At 25 °C (RT/F ≈ 25.7 mV), the slope value of 0.0312 V gives: αn = 0.0257/0.0312 ≈ 0.823.

Assuming a typical transfer coefficient of α ≈ 0.5 for an irreversible process [33]:

$$n = 0.823/0.5 \approx 1.65 \approx 2.$$

Thus, the electrooxidation of SDN involves approximately two electrons. Although the exact molecular oxidation mechanism of SDN could not be conclusively established in the present work, the combined pH dependence, scan-rate investigation, and Laviron analysis consistently indicate the participation of approximately two electrons and one proton in the overall irreversible oxidation process. In addition, the cyclic voltammetric responses of SDN were compared with those of ciprofloxacin and ofloxacin (Figure 7), which are also nitrogen-containing heterocyclic pharmaceuticals. Ciprofloxacin and ofloxacin exhibited relatively sharp and well-defined oxidation peaks, whereas SDN showed a broader anodic response with less-defined peak characteristics. These observations suggest that the electrooxidation of SDN at the (S,N)-rGO/GCE may involve multistep electron-transfer reactions and/or adsorbed intermediates rather than a simple proton-coupled electron-transfer process. Furthermore, the presence of tertiary nitrogen centers and a flexible heterocyclic framework in SDN may promote strong interaction with the π-conjugated conductive surface, thereby altering the apparent proton participation during oxidation and contributing to the lower E_p–pH slope observed experimentally. Based on the E_p–pH relationship and Laviron analysis, the electrooxidation of SDN is hypothesized to involve an apparent two-electron/one-proton (2e$^-$/1H$^+$) transfer process. However, this interpretation should be considered a plausible hypothesis rather than a definitive reaction mechanism, as the oxidation of SDN is known to involve complex multistep electron-transfer reactions. Moreover, adsorption of SDN and/or its

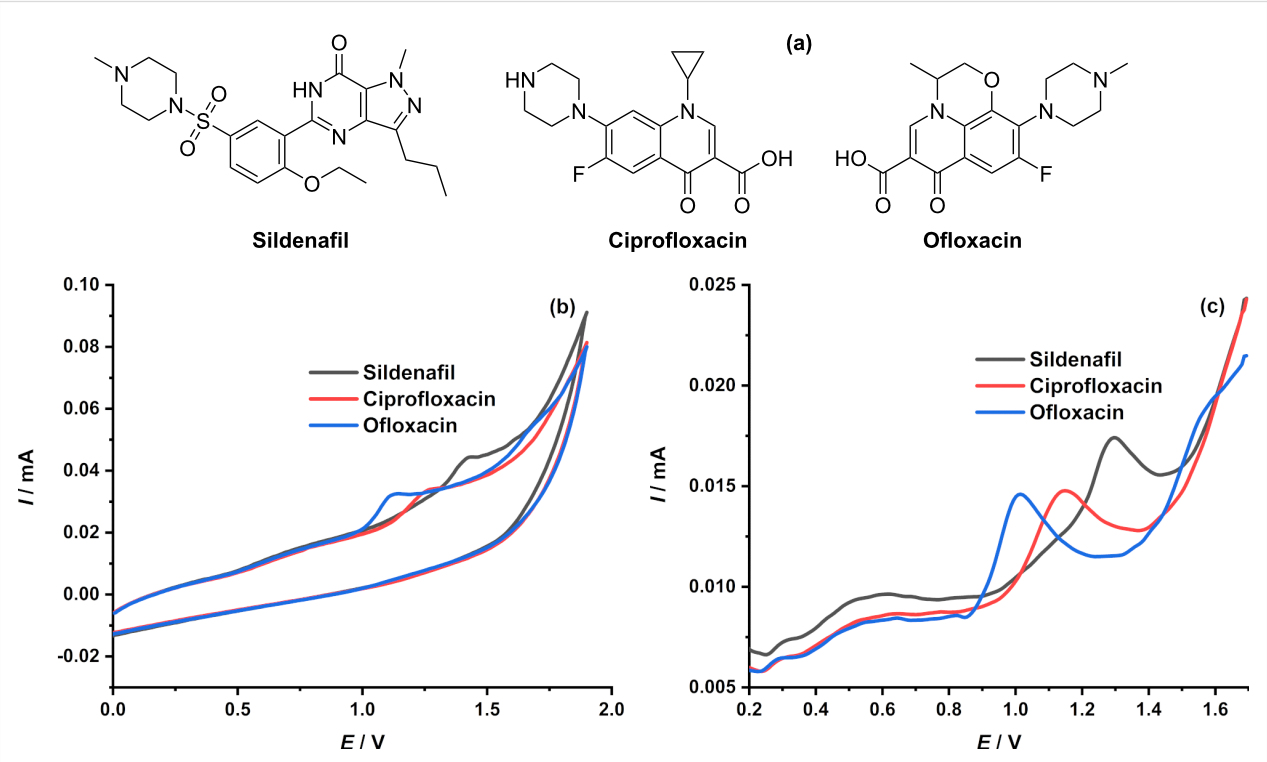


Figure 7: (a) Molecular structures, (b) CVs, and (c) DPVs of SDN, ciprofloxacin, and ofloxacin with concentration of 5.0 μM in 0.1 M BR buffer (pH 4.0).

oxidation intermediates on the (S,N)-rGO surface may influence the electrochemical response and the apparent kinetic parameters. Therefore, further mechanistic investigations, including in situ spectroelectrochemical measurements or identification of oxidation products, would be valuable for elucidating the detailed oxidation mechanism.

Optimizing operational parameters

The experimental parameters were optimized to achieve the best analytical performance (Supporting Information File 1, Figures S1–S4). The optimal conditions were determined as follows: accumulation potential of 0.4 V, accumulation time of 40 s, pulse amplitude of 0.10 V, and potential step of 0.007 V.

Linear range and limit of detection

The analytical performance of the proposed sensor was evaluated using DPV under the optimized conditions. As shown in Figure 8a, the oxidation peak current increases progressively with increasing SDN concentration from 0.25 to 19.61 µM. A good linear relationship between peak current and SDN concentration was obtained over this range (Figure 8b), described by the following equation:

$$I_{SDN} = (0.7945 \pm 0.0315) + (0.52501 \pm 0.0027) C_{SDN};$$
$$r^2 = 0.9993.$$

The LOD and the LOQ, calculated according to the criteria of 3S/b and 10S/b, respectively [34,35] were determined to be 0.49 and 1.61 µM. To further improve sensitivity at low concentrations, a narrower linear range (0.25–4.98 µM) was considered using eight concentration points near the origin. In this range, LOD and LOQ were significantly improved to 0.24 and 0.78 µM, respectively, demonstrating the enhanced detection capability of the sensor at trace levels.

As summarized in Table 2, the proposed (S,N)-rGO/GCE sensor exhibits a lower detection limit than most previously reported electrochemical sensors for SDN determination, while providing a wide linear range and satisfactory applicability for the analysis of pharmaceutical formulations.

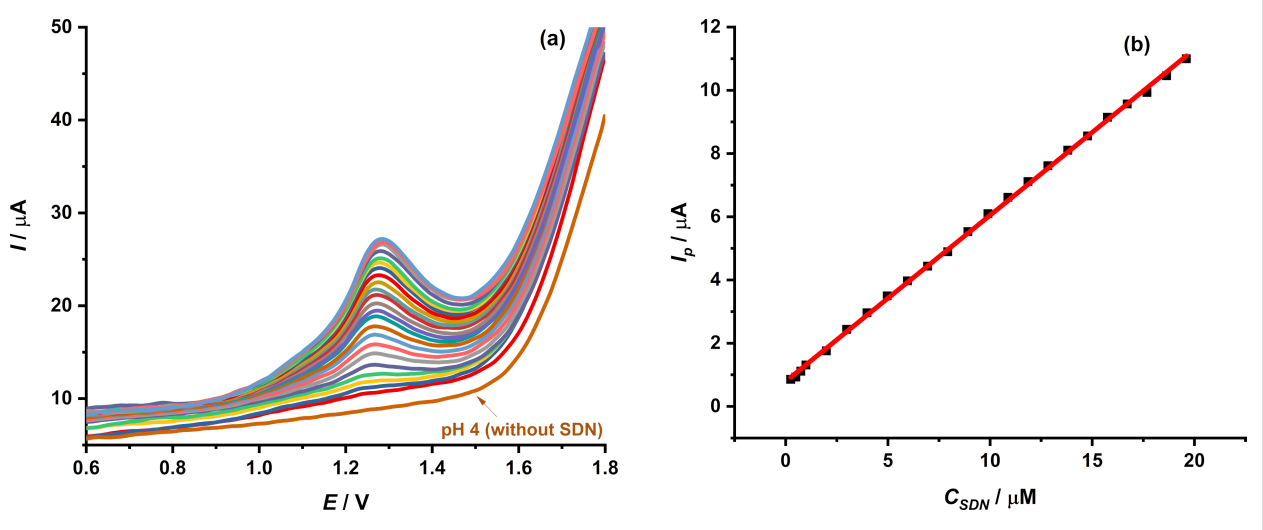


Figure 8: (a) DPV curves of (S,N)-rGO/GCE in 0.1 M Britton–Robinson buffer (pH 4.0) for different concentrations of C_{SDN} (0.25–19.61 µM); (b) corresponding calibration plot of peak current versus SDN concentration.

Table 2: Comparison of the analytical performance of electrochemical sensors for the determination of SDN.

Electrode	Method	Linear range (µM)	LOD (µM)	Application	Ref.
SPGCE	SWV	1.0–14.0	0.055	pharmaceutical and urine samples	[36]
SPCE	SWV	1.0–20.0	0.20	commercial and adulterated tablets	[37]
BDDE	DPV	0.730–7.3	0.64	pharmaceutical formulations	[38]
ABPUE-AgNP	DPV	1.0–10.0	0.89	pharmaceutical formulations and synthetic urine	[31]
Paraff-GE	SWV	25–250	9.0	pharmaceutical formulations	[39]
RuQT	DPV	12.5–500.0	10.7	pharmaceutical formulations	[40]
(S,N)-rGO/GCE	DPV	0.25–19.61	0.24	pharmaceutical formulations	this work

Repeatability, reproducibility, and long-term stability

Intra-day repeatability (within-electrode precision) of the proposed electrochemical method was evaluated at four representative concentration levels (1.0, 2.0, 13.8, and 19.6 µM) using replicate measurements (n = 3) (Figure 9a and Supporting Information File 1, Figure S5). At 1.0 µM, the peak current was 0.9585 ± 0.0469 µA, corresponding to an RSD of 4.90%, which is lower than the acceptable criterion of $0.5RSD_{Horwitz}$ = 8.50%. Similarly, at 2.0 µM, the peak current was 1.6990 ± 0.0732 µA with an RSD of 4.31%, also below the threshold ($0.5RSD_{Horwitz}$ = 7.66%). At higher concentrations, improved precision was observed, with RSD values of 1.30% and 1.02% for 13.8 and 19.6 µM, respectively, both significantly lower than the corresponding $0.5RSD_{Horwitz}$ values (5.73% and 5.43%) [41]. The electrode-to-electrode reproducibility of the sensor was further assessed using seven independently prepared electrodes at a fixed concentration of 13.8 µM (Figure 9b). The peak current was 7.9800 ± 0.1716 µA with an RSD of 2.15%, indicating good fabrication reproducibility. In addition, the long-term stability of the modified electrode was evaluated over seven consecutive days (Figure 9c). The average peak current was 7.8657 ± 0.1828 µA with an RSD of 2.32%, and the signal decreased by only 5.06% after seven days, demonstrating good storage stability. Overall, these results confirm that the proposed (S,N)-rGO/GCE sensor provides good precision, reproducibility, and stability, making it suitable for reliable electrochemical analysis.

Selectivity

The selectivity of the proposed electrochemical sensor was evaluated by investigating the effect of common inorganic ions and organic substances that may coexist with SDN (Supporting

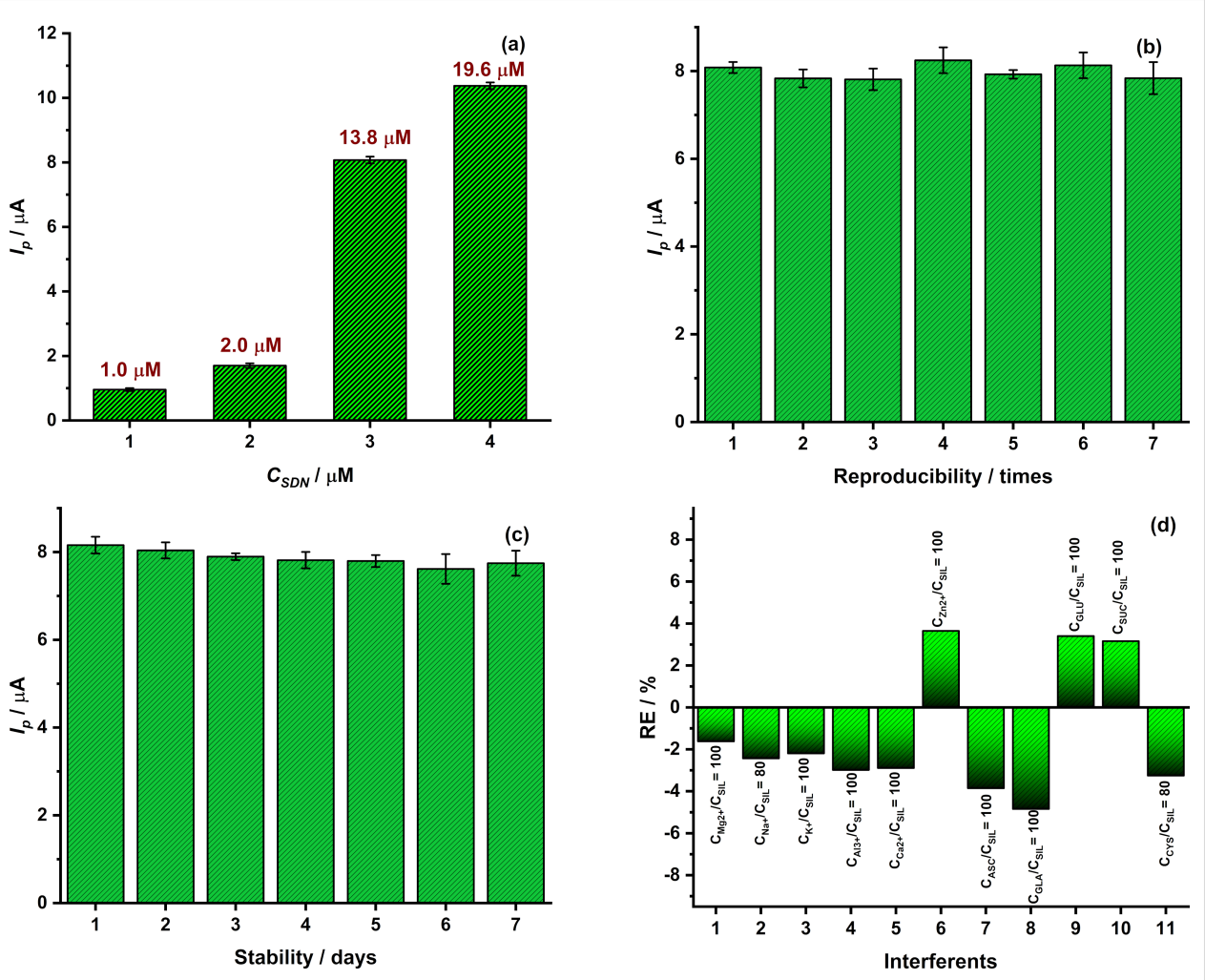


Figure 9: (a) Variation of peak current (I_p) for SDN at four concentrations (1.0, 2.0, 13.8, and 19.6 µM) recorded at the (S,N)-rGO/GCE in 0.1 M Britton–Robinson buffer (pH 4.0); (b) repeatability of the peak current at a fixed concentration (C_{SDN} = 13.8 µM) measured over seven successive determinations using the same electrode preparation procedure; (c) long-term stability of the sensor evaluated over seven consecutive days; (d) relative error (RE%) caused by interfering substances at different concentration ratios.

Information File 1, Table S1). Various potential interferents, including Mg^{2+}, Na^{+}, K^{+}, Al^{3+}, Zn^{2+}, and Ca^{2+}, as well as organic compounds such as ascorbic acid (ASC), glutamic acid (GLA), glucose (GLU), sucrose (SUC), and L-cysteine (CYS), were evaluated at concentration ratios ranging from 0 to 100-fold relative to SDN, except for Na^{+} and sucrose (SUC), which were investigated up to 80-fold (Figure 9d). As shown in Figure 9d, the presence of these interfering species caused only minor variations in the peak current of SDN. The relative error (RE) values were generally within ±5%, even at high interferent-to-analyte ratios (up to 100). In particular, most inorganic ions exhibited negligible interference, with RE values typically below ±3%. Organic compounds such as glucose and sucrose showed slight positive deviations, while ascorbic acid and L-cysteine resulted in small negative deviations, which can be attributed to their electroactive nature. However, these effects remained within acceptable analytical limits. According to commonly accepted criteria ($|RE| \leq 5\%$), these results demonstrate that the proposed (S,N)-rGO/GCE sensor possesses good selectivity for the determination of C_{SDN} in the presence of potential interfering substances. The high selectivity of the sensor suggests its strong potential for application in complex real samples.

Analysis of real sample

The applicability of the proposed (S,N)-rGO/GCE sensor was evaluated by determining SDN in commercial pharmaceutical samples using the DPV method. Three different products were analyzed, and the results are summarized in Table 3. The measured concentrations of C_{SDN} in the electrochemical cell were found to be 4.07 ± 0.07, 4.22 ± 0.08, and 4.05 ± 0.08 μM for samples 1–3, respectively. These values were converted to the corresponding SDN content per dosage unit, yielding 48.4, 102.5, and 47.6 mg, respectively. The analytical accuracy of the proposed sensor was evaluated using two complementary approaches. First, recovery experiments were carried out by the standard addition method, yielding satisfactory recoveries ranging from 97.6% to 103.5%. Second, the results obtained by the proposed DPV method were compared with those obtained using the reference HPLC method. No statistically significant difference was observed between the two methods, confirming the accuracy, reliability, and practical applicability of the developed electrochemical sensor for the determination of SDN in pharmaceutical formulations.

Although the developed (S,N)-rGO/GCE sensor demonstrated excellent analytical performance for the determination of SDN in pharmaceutical formulations, several limitations should be acknowledged. The present study focused exclusively on pharmaceutical samples, and therefore additional validation in more complex biological and environmental matrices is still required. Furthermore, while satisfactory stability was observed over a seven-day period, longer-term operational stability under routine analytical conditions remains to be investigated. The simple drop-casting fabrication procedure may also introduce slight variations in the modified film between independently prepared electrodes. In addition, although the sensor exhibited good selectivity toward the investigated interferents, structurally related electroactive compounds at relatively high concentrations could potentially influence the analytical response. Future work will focus on improving electrode fabrication reproducibility, extending the sensor lifetime, and evaluating its applicability in complex real-world samples.

Conclusion

In this study, an efficient electrochemical sensor based on a glassy carbon electrode modified with (S,N)-doped reduced graphene oxide ((S,N)-rGO) was successfully developed for the determination of SDN. The successful incorporation of nitrogen and sulfur into the graphene structure was confirmed by multiple characterization techniques, resulting in enhanced structural defects and improved electrochemical properties. The (S,N)-rGO/GCE exhibited excellent electrocatalytic activity toward SDN oxidation, enabling sensitive detection with a wide linear range (0.25–4.98 μM), a low limit of detection (0.24 μM), and a limit of quantification of 0.78 μM. The sensor also demonstrated good repeatability, reproducibility, and long-term stability, together with high selectivity in the presence of potential interfering species. Importantly, the proposed method was successfully applied to the analysis of pharmaceutical samples, and the results were in good agreement with those obtained by HPLC, confirming its accuracy and reliability. These

Table 3: Determination of SDN in commercial pharmaceutical samples using the proposed DPV method and comparison with the HPLC method.

Sample name	Found (μM)[a] ± SD (μM)	SDN (mg per unit, DPV)	SDN (mg per unit, HPLC)	Added (μM)	Found after spiking (μM) ± SD[a] (μM)	Recovery (%)
1	4.07 ± 0.07	48.4	51.5	1.00	5.06 ± 0.06	98.1
2	4.22 ± 0.08	102.5	102.0		5.36 ± 0.14	103.5
3	4.05 ± 0.08	47.6	48.7		5.06 ± 0.06	97.6

[a]Concentration calculated in the electrochemical cell.

findings indicate that the (S,N)-rGO-based electrochemical sensor provides a simple, cost-effective, and reliable alternative for the routine determination of SDN in real samples.

The proposed (S,N)-rGO-functionalized sensing platform offers several advantages, including a simple and low-cost fabrication process, enhanced electron-transfer capability, high electrocatalytic activity, satisfactory selectivity, and reliable determination of SDN in pharmaceutical formulations. Compared with conventional chromatographic techniques, the proposed electrochemical sensor provides rapid analysis with minimal sample preparation and lower instrumentation cost. Nevertheless, the current study is limited to pharmaceutical samples, and further investigations are required to evaluate long-term operational stability and its applicability to more complex biological and environmental matrices.

Supporting Information

Supporting Information File 1

Additional figures.
[https://www.beilstein-journals.org/bjnano/content/supplementary/2190-4286-17-74-S1.pdf]

Funding

Hue University partially funded this research under the Core Research Program No. NCTB.DHH.2025.05.

Author Contributions

Nguyen Quang Man: conceptualization; funding acquisition; writing – original draft. Ngo Thi Thanh Xuan: conceptualization; funding acquisition; writing – original draft. Vo Thi Khanh Ly: investigation; methodology; resources; validation; visualization. Le Van Thanh Son: investigation; methodology; resources; validation; visualization. Le Duc Anh: investigation; methodology; resources; validation; visualization. Le Thi Hong Phong: investigation; methodology; resources; validation; visualization. Nguyen Hai Phong: supervision. Pham Khac Lieu: investigation; methodology; resources; validation; visualization. Le Lam Son: investigation; methodology; resources; validation; visualization. Dinh Quang Khieu: writing – review & editing.

ORCID® iDs

Nguyen Quang Man - https://orcid.org/0000-0001-6511-1236
Ngo Thi Thanh Xuan - https://orcid.org/0009-0000-9270-5056
Vo Thi Khanh Ly - https://orcid.org/0009-0005-0854-3290
Le Van Thanh Son - https://orcid.org/0000-0002-2061-6983
Le Duc Anh - https://orcid.org/0000-0002-5940-8591
Le Thi Hong Phong - https://orcid.org/0000-0001-8825-6243
Nguyen Hai Phong - https://orcid.org/0000-0001-5354-1052
Pham Khac Lieu - https://orcid.org/0000-0002-9002-1416
Le Lam Son - https://orcid.org/0000-0002-8693-7472
Dinh Quang Khieu - https://orcid.org/0000-0003-3473-6377

Data Availability Statement

All data that supports the findings of this study is available in the published article and/or the supporting information of this article.

References

1. Ghantous, I.; Tlais, M.; El Khatib, A.; Ghantous, G.; Maroun, G.; Challita, A.; Ayek, M.; Barmo, G.; Sahyoun, M.; Kary, G. *Glob. Cardiol. Sci. Pract.* **2025,** *2025,* e202531. doi:10.21542/gcsp.2025.31
2. Maliyakal, J.; Vadnere, N.; Bherje, S.; Patel, M. *Trends Environ. Anal. Chem.* **2025,** *47,* e00273. doi:10.1016/j.teac.2025.e00273
3. Tian, X.-y.; Zhang, M.-m.; Sun, F.-r. *J. Chromatogr. A* **2026,** *1766,* 466581. doi:10.1016/j.chroma.2025.466581
4. Ahmed, A.; Abdellah, N.; Shaltout, E. *Mansoura J. Forensic Med. Clin. Toxicol.* **2019,** *27,* 43–56. doi:10.21608/mjfmct.2019.52475
5. Oltulu, Ç.; Çelik, S.; Daşman, M. *Istanbul J. Pharm.* **2023,** *53,* 219–228. doi:10.26650/istanbuljpharm.2023.1206425
6. Momtaz, M. A.; El-Desoky, H. S.; Rehab, A.; Belal, F. *Talanta Open* **2025,** *12,* 100540. doi:10.1016/j.talo.2025.100540
7. Al Dhakhri, H. H.; Alqassabi, F.; Alrasbi, I.; Alhinai, D.; Al Salty, S.; Pannu, S.; Al Balushi, S.; Khan, S. A.; Akhtar, M. J. *Int. J. Second. Metab.* **2025,** *12,* 297–305. doi:10.21448/ijsm.1518387
8. Zhang, Y.; Zhang, H.; Jia, Z.; Li, C.; Chen, L.; Jin, S. *ACS Appl. Nano Mater.* **2026,** *9,* 5576–5585. doi:10.1021/acsanm.6c00595
9. Minh, D. T. C.; Nhu, N. T. Q.; Thi, L. A.; Vu, L. V.; Lan, D. T. N.; Anh, N. T. K.; Ha, P. T. T. *J. Pharm. Biomed. Anal.* **2024,** *251,* 116392. doi:10.1016/j.jpba.2024.116392
10. Wei, T.; Zhang, Y.; Huang, J.; Yang, J.; Tian, Y.; Shen, Y. *Food Biosci.* **2024,** *59,* 103905. doi:10.1016/j.fbio.2024.103905
11. Li, G.; Pan, Q.; Zhang, C.; Wang, J.; Peng, C.; Wang, Z. *Anal. Chim. Acta* **2023,** *1280,* 341883. doi:10.1016/j.aca.2023.341883
12. Zeng, R.; Qiu, M.; Wan, Q.; Huang, Z.; Liu, X.; Tang, D.; Knopp, D. *Anal. Chem. (Washington, DC, U. S.)* **2022,** *94,* 15155–15161. doi:10.1021/acs.analchem.2c03606
13. Chen, S.; Tian, S.; Wang, Y.; Li, M.; Tang, D. *Biosens. Bioelectron.* **2025,** *278,* 117340. doi:10.1016/j.bios.2025.117340
14. Barzani, H. A. H.; Anwar Omer, R.; Salih Barzani, K. I.; Jawhar, Z. H.; Sulaiman, S. H. *Crit. Rev. Anal. Chem.* **2026,** 1–35. doi:10.1080/10408347.2025.2611097
15. Alarcon, R. T.; da Silva, R.; Bannach, G.; Cavalheiro, É. T. G. *ACS Omega* **2026,** *11,* 15452–15461. doi:10.1021/acsomega.5c13297
16. Mombeshora, E. T.; Muchuweni, E. *RSC Adv.* **2023,** *13,* 17633–17655. doi:10.1039/d3ra02098c
17. Boroujerdi, R.; Paul, R. *Nanomaterials* **2022,** *12,* 2250. doi:10.3390/nano12132250
18. Gong, H.; Hu, X.; Zeng, R.; Li, Y.; Xu, J.; Li, M.; Tang, D. *Sens. Actuators, B* **2022,** *369,* 132307. doi:10.1016/j.snb.2022.132307
19. Zhou, Q.; Lin, Y.; Zhang, K.; Li, M.; Tang, D. *Biosens. Bioelectron.* **2018,** *101,* 146–152. doi:10.1016/j.bios.2017.10.027

20. Turunc, E.; Ucar, A.; Binzet, R.; Martinez, F. *Microchem. J.* **2026,** *220,* 116697. doi:10.1016/j.microc.2025.116697
21. Periyasamy, G.; Annamalai, K.; Patil, I. M.; Kakade, B. *Diamond Relat. Mater.* **2021,** *114,* 108338. doi:10.1016/j.diamond.2021.108338
22. Ngô, T. T. X.; Lê, Đ. A.; Nguyn, Q. M. *Hue Univ. J. Sci. Nat. Sci.* **2025,** *134,* 91–100. doi:10.26459/hueunijns.v134i1c.7820
23. Marcano, D. C.; Kosynkin, D. V.; Berlin, J. M.; Sinitskii, A.; Sun, Z.; Slesarev, A.; Alemany, L. B.; Lu, W.; Tour, J. M. *ACS Nano* **2010,** *4,* 4806–4814. doi:10.1021/nn1006368
24. Amir Faiz, M. S.; Che Azurahanim, C. A.; Raba'ah, S. A.; Ruzniza, M. Z. *Results Phys.* **2020,** *16,* 102954. doi:10.1016/j.rinp.2020.102954
25. Rochman, R. A.; Wahyuningsih, S.; Ramelan, A. H.; Hanif, Q. A. Preparation of Nitrogen and Sulphur Co-Doped Reduced Graphene Oxide (RGO-NS) Using N and S Heteroatom of Thiourea. In *IOP Conference Series: Materials Science and Engineering, Vol. 509,* 2019. doi:10.1088/1757-899x/509/1/012119
26. Chang, Y.-S.; Chen, F.-K.; Tsai, D.-C.; Kuo, B.-H.; Shieu, F.-S. *Sci. Rep.* **2021,** *11,* 20719. doi:10.1038/s41598-021-99883-9
27. Bharath, G.; Anwer, S.; Mangalaraja, R. V.; Alhseinat, E.; Banat, F.; Ponpandian, N. *Sci. Rep.* **2018,** *8,* 5718. doi:10.1038/s41598-018-24066-y
28. Madbouly, L. A.; Mrkwitschka, P.; Stockmann, J. M.; Jones, E.; Radnik, J.; Hodoroaba, V.-D. *Surf. Interface Anal.* **2025,** *57,* 300–306. doi:10.1002/sia.7386
29. Tessier, F. *Materials* **2018,** *11,* 1331. doi:10.3390/ma11081331
30. Nguyen, V. T.; Manh, T. D.; Duyen, V. T.; Binh, N. T. M.; Van Duong, D.; Tu, N. T. T.; Toan, T. T. T.; Nhiem, D. N.; Son, L. L.; Nhan, D. Q.; Quyen, N. D. V.; Hoa, D. T. N.; Khieu, D. Q. *J. Nanopart. Res.* **2022,** *24,* 145. doi:10.1007/s11051-022-05522-3
31. da Silva, R.; Alarcon, R. T.; Cavalheiro, É. T. G. *J. Electroanal. Chem.* **2025,** *979,* 118938. doi:10.1016/j.jelechem.2025.118938
32. Laviron, E. *J. Electroanal. Chem. Interfacial Electrochem.* **1979,** *101,* 19–28. doi:10.1016/s0022-0728(79)80075-3
33. Li, C. *Colloids Surf., B* **2007,** *55,* 77–83. doi:10.1016/j.colsurfb.2006.11.009
34. Yu, Z.; Qiu, C.; Huang, L.; Gao, Y.; Tang, D. *Anal. Chem. (Washington, DC, U. S.)* **2023,** *95,* 4212–4219. doi:10.1021/acs.analchem.2c05617
35. Lin, Y.; Zhou, Q.; Tang, D.; Niessner, R.; Knopp, D. *Anal. Chem. (Washington, DC, U. S.)* **2017,** *89,* 5637–5645. doi:10.1021/acs.analchem.7b00942
36. Farghali, R. A.; Ahmed, R. A. *Int. J. Electrochem. Sci.* **2012,** *7,* 13008–13019. doi:10.1016/s1452-3981(23)16605-3
37. Rocha, D. S.; Silva-Neto, H. A.; de Oliveira, L. C.; Souza, S. G. G.; Santana, M. H. P.; Coltro, W. K. T. *Braz. J. Anal. Chem.* **2022,** *9,* 210–228. doi:10.30744/brjac.2179-3425.ar-65-2021
38. Batista, É. F.; Sartori, E. R.; Medeiros, R. A.; Rocha-Filho, R. C.; Fatibello-Filho, O. *Anal. Lett.* **2010,** *43,* 1046–1054. doi:10.1080/00032710903491153
39. Mendonça, R. X.; Buzzetti, P. H. M.; Silva, A. L.; Araújo, A. S.; Ponzio, E. A.; Semaan, F. S. *Rev. Virtual Quim.* **2015,** *7,* 1692–1708. doi:10.5935/1984-6835.20150096
40. Delolo, F. G.; Rodrigues, C.; da Silva, M. M.; Dinelli, L. R.; Delling, F. N.; Zukerman-Schpector, J.; Batista, A. A. *J. Braz. Chem. Soc.* **2014,** *25,* 550–559. doi:10.5935/0103-5053.20140031
41. Horwitz, W.; Albert, R. *J. AOAC Int.* **2006,** *89,* 1095–1109. doi:10.1093/jaoac/89.4.1095

License and Terms

This is an open access article licensed under the terms of the Beilstein-Institut Open Access License Agreement (https://www.beilstein-journals.org/bjnano/terms), which is identical to the Creative Commons Attribution 4.0 International License (https://creativecommons.org/licenses/by/4.0). The reuse of material under this license requires that the author(s), source and license are credited. Third-party material in this article could be subject to other licenses (typically indicated in the credit line), and in this case, users are required to obtain permission from the license holder to reuse the material.

The definitive version of this article is the electronic one which can be found at:
https://doi.org/10.3762/bjnano.17.74

BEILSTEIN JOURNAL OF NANOTECHNOLOGY

Synthesis of carbon dot-mediated gold nanostructures: experimental and quantum chemical insights into turn-on fluorescence sensing of *N*-acetylcysteine

Thuy-Huong Nguyen[1], Van-Nghia Nguyen[1], Ha Thi Thu Nguyen[1], Ha Ngoc Nguyen[2], Anh Duc Nguyen[3], Tuyen Viet Nguyen[4] and Truong Xuan Nguyen[*1]

Full Research Paper

Open Access

Address:
[1]School of Chemistry and Life Sciences, Hanoi University of Science and Technology, 01 Dai Co Viet, Hanoi, Vietnam, [2]Faculty of Chemistry, Hanoi National University of Education, 136 Xuan Thuy, Hanoi, Vietnam, [3]University of Science and Technology of Hanoi, Vietnam Academy of Science and Technology, 18 Hoang Quoc Viet, Hanoi, Vietnam and [4]University of Science, Vietnam National University, 334 Nguyen Trai, Hanoi, Vietnam

Email:
Thuy-Huong Nguyen - huong.NT221799@sis.hust.edu.vn;
Van-Nghia Nguyen - nghia.nguyenvan@hust.edu.vn;
Ha Thi Thu Nguyen - ha.nguyenthithu3@hust.edu.vn;
Ha Ngoc Nguyen - hann@hnue.edu.vn;
Anh Duc Nguyen - nguyen-duc.anh@usth.edu.vn;
Tuyen Viet Nguyen - nguyenviettuyen@hus.edu.vn;
Truong Xuan Nguyen[*] - truong.nguyenxuan@hust.edu.vn

* Corresponding author

Keywords:
fluorescence; gold nanoparticles; green synthesis; *N*-acetylcysteine; nitrogen-doped carbon dots

Beilstein J. Nanotechnol. **2026,** *17,* 1103–1116.
https://doi.org/10.3762/bjnano.17.75

Received: 09 May 2026
Accepted: 28 July 2026
Published: 12 August 2026

This article is part of the thematic issue "Innovative nanomaterials for next-generation bio- and chemosensing".

Guest Editor: Q. T. Duong



© 2026 Nguyen et al.; licensee Beilstein-Institut.
License and terms: see end of document.

Abstract

In this work, a green and sustainable hydrothermal approach was employed to synthesize nitrogen-doped carbon dots (NCDs) using lemon juice as a natural precursor. The as-prepared NCDs served as eco-friendly reducing agents and stabilizing scaffolds for the subsequent in situ synthesis of gold nanoparticles (Au@NCDs). The structural and optical properties of the nanocomposite were comprehensively characterized using various analytical techniques. The intrinsic fluorescence of NCDs was significantly quenched upon formation of the composite, mainly due to non-radiative energy transfer processes. Interestingly, the quenched fluorescence could be efficiently restored upon the addition of *N*-acetylcysteine (NAC), enabling the development of an “off-on” fluorescent sensing platform. The sensing mechanism was systematically elucidated through a combination of spectroscopic studies and density functional theory calculations, revealing that fluorescence recovery originates from a ligand exchange process driven by the stronger binding affinity of NAC toward the gold surface, particularly via Au–S interactions. Under optimized conditions, the assay exhibited a robust linear response for NAC concentrations ranging from 4.0 to 20.0 mg/L, with a detection limit of 0.863 mg/L. These results demonstrate that the Au@NCDs system can function as a sensitive and selective OFF–ON fluorescent probe for NAC

detection. This study provides a cost-effective and eco-friendly sensing platform with significant potential for analytical applications in pharmaceutical monitoring.

Introduction

N-acetylcysteine (NAC) has been widely employed for over four decades as an antidote in the treatment of paracetamol (acetaminophen) overdose [1-3] and as a mucolytic agent for chronic obstructive pulmonary disease (COPD) [4]. Careful dosage control of NAC is crucial to ensure effective treatment and prevent side effects. Several analytical methods have been conventionally used to determine NAC levels in biological or pharmaceutical samples, including chromatography [5,6] and spectroscopy [7-9]. Currently, electrochemical and optical sensors are gaining prominence in clinical analysis due to their simplicity, requirement for small sample volumes, cost-effectiveness, high specificity, and selectivity [10-16].

Carbon quantum dots (CQDs or CDs) have garnered significant attention due to their strong fluorescence and exhibit significant potential in applications such as photocatalysis, bioimaging, bioanalytical sensing, and pharmaceutical testing [17]. CDs can be synthesized from diverse precursors, including citric acid, carbohydrates, and organic molecules through two distinct methodologies, that are, bottom-up and top-down methods [18,19]. In recent years, carbon dots derived from natural sources have increasingly attracted interest as a sustainable and environmentally friendly approach [20-22]. Natural precursor sources, including plant extracts, fruits, and vegetables (e.g., orange juice [23], turmeric [24], lemon juice [25], mango leaves [26], and guava leaves [27]), are abundant, inexpensive, and renewable carbon sources. Furthermore, they contain various organic compounds with hydroxy, carboxyl, and amino groups. Consequently, natural-product-derived carbon dots frequently demonstrate high hydrophilicity, excellent biocompatibility, and a broader spectrum of surface functional groups compared with CDs synthesised from chemical precursors [28-30].

Among the various strategies aimed at improving the physicochemical properties of CDs, heteroatomic doping has been extensively studied [31]. Nitrogen-doped carbon dots (NCDs) are formed by introducing nitrogen atoms into carbon frameworks or functional groups on the surface. Nitrogen doping alters the electronic structure of the carbon core and creates surface functional groups such as amine and pyridinic groups. Compared with undoped carbon dots, NCDs featured excellent robust fluorescence stability and chemical resistance [32].

Fluorescent probes are powerful analytical tools favored for their rapid response, high sensitivity, simplicity, low cost, and real-time detection capabilities. To overcome the inherent limitations of organic dyes, nanomaterial-based sensing platforms have attracted considerable research interest. In particular, gold-based composite nanoparticles stand out as promising candidates for advanced fluorescent probes, owing to their exceptional optical properties, large specific surface area, excellent biocompatibility, and ease of surface functionalization [33]. A key feature of gold nanoparticles is their surface plasmon resonance, which generates strong light–matter interactions, amplifies optical signals, and underpins their extensive application in optical sensing [34].

This study developed an OFF–ON fluorescent sensor based on gold nanoparticles and nitrogen-doped carbon dots (Au@NCDs) for the determination of NAC. NCDs, possessing strong luminescence properties, served as both reducing agent and stabilizing agent for the synthesis of Au@NCDs [35]. Upon excitation of the NCDs, the energy was transferred to the gold nanoparticles, resulting in fluorescent quenching. With the addition of NAC, a ligand exchange occurred between the thiol groups of NAC and the NCDs on the gold nanoparticles surface, resulting in the formation of a stronger Au–S bond and the subsequent recovery of the fluorescent signal. The restored fluorescence intensity exhibited a proportional relationship with the concentration of the added NAC.

In addition to experimental characterization, density functional theory (DFT) calculations have emerged as a powerful approach for elucidating the molecular-level mechanisms governing the performance of nanomaterial-based fluorescent sensors [36-38]. DFT provides valuable insights into adsorption configurations, binding energies, charge redistribution, and electronic structures, thereby enabling the interpretation of analyte–nanomaterial interactions that are often difficult to resolve experimentally. In particular, for gold nanostructure-based sensing platforms, DFT has been widely employed to investigate the formation and stability of Au–S bonds [39,40], ligand exchange processes [41,42], and the associated electronic changes responsible for fluorescence quenching and recovery [43-45]. Therefore, integrating DFT calculations with experimental studies offers a comprehensive understanding of the sensing mechanism and facilitates the rational design of highly sensitive fluorescent nanosensors.

Although carbon dots and gold nanoparticles have been widely investigated for fluorescence sensing, the development of lime

juice-synthesized carbon dot-mediated gold nanostructures with mechanistic insight into their fluorescence response toward NAC remains limited. In particular, the relationship between the structural and electronic properties of Au@NCD nanocomposites and their fluorescence sensing behavior has not been fully understood. Therefore, the novelty of this study lies not only in using a natural source for synthesis of Au@NCD nanostructures but also in the combination of experimental and theoretical approaches to provide mechanistic insights into the fluorescence sensing process.

Experimental

Chemicals and instrumentation

Tetrachloroauric(III) acid trihydrate (99.5%), urea (99.5%), dimethylformamide (DMF, ≥99.8%), acetone (≥99.8%), and silicagel 60 (0.015–0.040 mm) were purchased from Merck, USA. *N*-Acetylcysteine ≥98% and ethanol 95% were supplied by ThermoFisher, USA. Acetonitrile (ACN, ≥99.9%) was bought from Fisher Scientific, England. Fresh lime juice was prepared from limes (*Citrus* × *aurantiifolia*) obtained from a local supermarket in Hanoi, Vietnam. The chemicals were used as received, and their solutions were prepared in double distilled water. Fluorescence measurements were carried out using a Jasco FP-6500 spectrofluorometer (Japan). Absorption spectra were collected on an Agilent 8453 UV–vis spectrophotometer (USA). Fourier-transform infrared (FTIR) spectra were recorded by a Nicolet iS50 spectrometer from Thermo Scientific (Japan). Morphologies and sizes of the products were characterized using a JEOL JEM-1010 Transmission electron microscope (TEM), and a JEOL JSM-IT800 field emission scanning electron microscope (FESEM) (Japan). The elemental analysis was carried out on an Oxford EDX Ultim Max 65 (England) coupled with the FESEM instrument. Raman spectra of the samples were taken with an acquisition time of 60 s in two cycles by using HR 800 spectrometer from Horiba Jobin Yvon (France). The size distribution was characterized using a dynamic light scattering (DLS) Instrument (Horiba SZ-100-Z2, Japan). The glass chromatographic column with 45 cm in length and 2 cm in diameter was purchased from Duran, Germany.

Synthesis of nitrogen-doped carbon dots

NCDs were synthesized via a modified hydrothermal method [46]. Typically, a mixture of 20 mL of fresh lemon juice and 0.8 g of urea was stirred, transferred into a 50 mL Teflon-lined autoclave, and heated at 180 °C for 3 h. Afterward, the autoclave was allowed to cool naturally to room temperature. The resulting mixture was purified by gradient silica gel column chromatography, using approximately 100 mL acetone followed by 250 mL acetone/distilled water mixture (4:1, v/v) as the mobile phase. The purified CD fractions were identified by collecting sequential eluates and monitoring their fluorescence under UV light (365 nm) and PL spectroscopy. Fractions exhibiting an intense characteristic fluorescence of CDs were combined, while non-fluorescent or weakly fluorescent fractions were discarded [47].

Preparation of Au@NCDs composite

The synthesis conditions of Au@NCDs composites were primarily optimized including NCDs/$HAuCl_4$ ratio, temperature, and reaction time (see section 2 in Supporting Information File 1). The Au@NCDs composite was obtained by adding 2.5 mL of a NCD solution (0.15 mg/mL) to 2.5 mL of 0.2 mM $HAuCl_4$ under continuous stirring and heating at 60 °C. After 5 min, the solution gradually changed in color from yellow to pink. The mixture was then left at room temperature for 15 min before use [16,48]. The resulting mixture was centrifuged at 10,000 rpm for 30 min, and the supernatant was discarded. The precipitate was redispersed in deionized water (DW) and stored for further use.

Optimization of the organic solvent composition

The effect of the organic solvent on the fluorescence response of the Au@NCDs sensing system was investigated using mixtures of aqueous and organic solvents. Methanol, ethanol, acetone, ACN, and DMF were individually mixed with DW at a volume ratio of 25:75 (v/v). NAC standard solutions (25 mg/L) were prepared in each solvent mixture under identical conditions.

For each experiment, an aliquot of the Au@NCDs probe was mixed with the corresponding NAC solution, and the fluorescence intensity was recorded after incubation under the optimized sensing conditions described in section “Preparation of Au@NCDs composite”. The fluorescence recovery was evaluated as the change in fluorescence intensity (ΔI), calculated from the difference between the fluorescence intensity of the Au@NCDs probe in the presence (I) and absence (I_0) of NAC ($\Delta I = I - I_0$). All measurements were performed in triplicate, and the average values were used for comparison.

After identifying DMF as the most suitable organic solvent, its proportion in the water/DMF mixture was further optimized. Water/DMF mixtures containing 5%, 10%, 15%, 20%, and 25% (v/v) DMF were prepared while maintaining the NAC concentration at 25 mg/L. Fluorescence measurements were carried out under identical experimental conditions, and the corresponding fluorescence recovery (ΔI) was compared to determine the optimal solvent composition. Based on these experiments, a water/DMF mixture containing 25% (v/v) DMF was selected and used for all subsequent fluorescence sensing experiments.

Assay of *N*-acetylcysteine

Fresh standard NAC solutions were prepared prior to analysis and only stable Au@NCDs dispersions prepared using the same synthesis protocol were used for measurements. A mixture of DW and DMF solvent was used as a blank to zero background signals. All fluorescence measurements were performed under identical instrumental conditions and each experiment was conducted in triplicate. A specific amount of DMF solvent was added to 1 mL of Au@CDs solution, followed by 0.5 mL of NAC standard solution at concentration ranging from 1.0 to 80.0 mg/L. The resulting mixture was then equilibrated for 5 min. Subsequently, the fluorescent spectra of the prepared solutions were recorded. All measurements were performed in triplicate, and the average values were used for calculation. The analytical linear range and limit of detection were calculated from the obtained data.

Computational details

All calculations were carried out within the framework of DFT using the SIESTA package [49]. The exchange–correlation energy was described by the generalized gradient approximation with the Perdew–Burke–Ernzerhof functional [50]. Dispersion interactions were included using the Grimme DFT-D3 dispersion correction scheme with default parameters [51,52]. Norm-conserving pseudopotentials were used to represent the ionic cores, and valence states were expanded in a double-ζ plus polarization (DZP) numerical atomic orbital basis set for all atoms. The real-space integration grid was defined by a mesh cutoff of 4761.99 eV, which was verified to ensure convergence of total energies. Electronic occupations were treated using a Fermi–Dirac distribution at 300 K. Self-consistent field calculations were performed using the diagonalization method with Pulay mixing (mixing weight 0.15). Spin-polarized calculations were employed throughout the study.

The simulated system consisted of a gold nanocluster containing 249 Au atoms, which serves as a representative model for metallic Au nanoparticles (Au NPs) [53], interacting with a NCD model and NAC (Figure 1). The optimized structure of NAC shows good agreement with experimental data, with calculated geometric parameters deviating from reported values by approximately 1.17–3.4% (see Figure S2 and Table S2 in Supporting Information File 1), confirming the reliability of the computational approach. The NCD structure was constructed based on reported structural models, incorporating surface functional groups such as $–NH_2$, –OH, and –COOH. The model consists of 54 atoms, with edge carbon atoms hydrogen-passivated to satisfy valence requirements. All systems were modeled under periodic boundary conditions using sufficiently large simulation cells to avoid interactions between periodic images. Owing to the presence of acidic functional groups (–COOH, –SH), the interactions between NAC/NCD and Au NPs were systematically investigated for both neutral species (NAC and NCD) and their corresponding deprotonated forms (NAC^- and NCD^-). This approach allowed for a comprehensive evaluation of binding behavior under different chemical environments and provides a basis for understanding the ligand exchange mechanism discussed in subsequent sections.

Results and Discussion

Structural and morphological analysis

Characteristic functional groups of NCDs such as hydroxy, amine, carboxyl and carbonyl groups [54-56] are evident in the FTIR spectrum in Figure 2. Specifically, the broad absorption band in the 3000 to 3500 cm^{-1} region can be attributed to the stretching vibration of –NH/–OH group ($\upsilon_{N–H}/\upsilon_{O–H}$). Absorption peaks around 1635 cm^{-1} (shoulder) and 1569 cm^{-1} are assigned to $\upsilon_{C=O}$, while peaks at 1390 cm^{-1} correspond to C–N

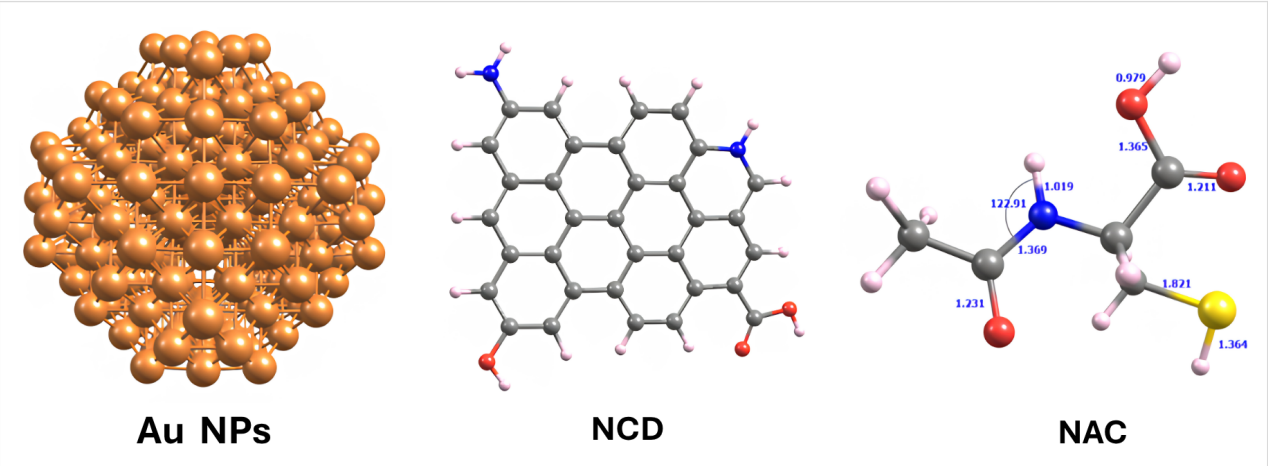


Figure 1: Optimized structures of (a) Au NPs, (b) NCD, (c) NAC. Color codes: light brown – Au, grey – C, blue – N, red – O, yellow – S, ivory – H. All key distances are in angstroms, angles are in degrees.

stretching vibrations. Vibration of –CO/CN/CH groups are responsible for the absorption peaks around 1078 cm^{-1}. The C–H stretching vibrations of benzene are represented by the peak at 786 cm^{-1}.

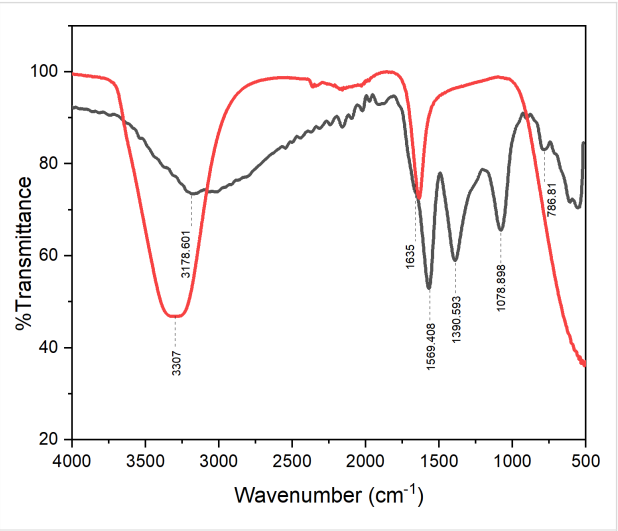


Figure 2: FTIR spectra of NCDs (black line) and Au@NCDs (red line).

Figure 3 shows the Raman spectra of NCDs and Au@NCDs. The NCD spectrum lacked discernible peaks due to significant fluorescence interference while Au@NCDs clearly shows the D band and the G band of carbon at 1360 and 1530 cm^{-1}, respectively [17]. Fluorescence quenching of carbon dots by Au nanostructures is a well-documented phenomenon where the fluorescence intensity of CDs decreases upon the addition of Au^{3+}. The quenching of the NCDs' photoluminescence can occur due to different mechanisms. The quenching can be attributed to a redox reaction where the Au^{3+} ions interact with the surface functional groups of the CDs, leading to a redox reaction, disrupting the normal radiative decay of the excited state in the CDs and thus reducing fluorescence [57]. Another mechanism for quenching is aggregation [58]. Reaction with Au^{3+} can also induce aggregation of the CDs, leading to a reduction of surface area and increased non-radiative decay pathways, while suppressing the fluorescence process. Moreover, the fluorescence of CDs might be quenched through fluorescence resonance energy transfer (FRET), a process involving energy transfer from the CD donor to the AuNP acceptor [59,60].

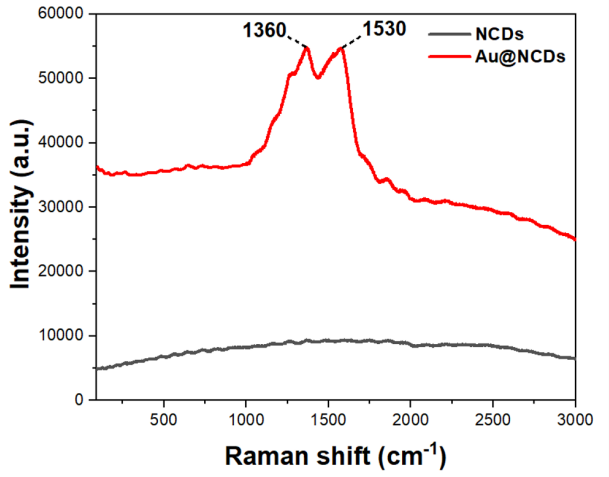


Figure 3: Raman spectra of NCDs and Au@NCDs.

As can be seen in Figure 4a, NCDs tend to form clusters with an average size of 30 nm size. In contrast, a mixture of spherical, polyhedral, triangular, and rod-like Au nanostructures is observed with Au@NCDs (Figure 4b). The diameter of Au NPs was approximately 35 nm, which is in agreement with dynamic laser scattering (DLS) analysis (Figure 4c). Indeed, the DLS results showed that the Au@NCD nanoparticles have sizes from 20 to 90 nm, while the average value is 35 ± 16.4 nm. The recorded PDI of 0.35 for the Au@NCDs indicated a highly polydispersed system resulting from a mixture of different structural Au nanoparticles. In addition, the zeta potential of

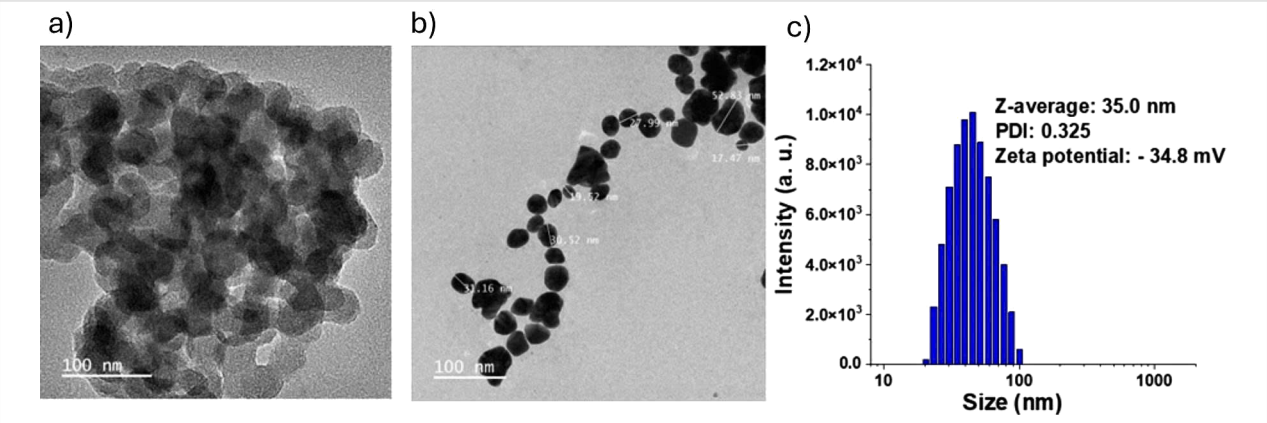


Figure 4: TEM images of (a) NCDs and (b) Au@NCDs and (c) DLS size distribution analysis of Au@NCDs.

−34.8 mV indicated a stable colloidal solution of Au@NCDs in water.

The element distribution on Au@NCDs and Au@NCDs-NAC were analyzed by FESEM in combination with energy dispersed X-ray spectroscopy as shown in Figure 5 and Figure 6, respectively. The spectra indicated that there were Au and C in Au@NCDs and Au, C, N, and S in Au@NCDs-NAC. The Au and C mapping images revealed the strong interaction between Au nanoparticles and NCDs in all samples. The presence of S in the EDX spectra of Au@NCDs-NAC suggested that the NAC molecules have interacted closely with NCDs.

Photophysical properties

Figure 7a shows the absorption spectra of NCDs and Au@NCDs. A distinct peak at 340 nm can be assigned to the π→π* transition of carbonyl C=O bonds present on the surface of NCDs. In the absorption spectrum of the Au@NCDs composite, this characteristic peak vanished due to the strong electronic interactions between the gold nanoparticles and NCDs [16]. Furthermore, the formation of Au NPs is confirmed by the presence of a broad surface plasmon resonance band centered around 550 nm.

Figure 7b presents photoluminescence (PL) spectra of NCDs and Au@NCDs when excited at 355 nm. It can be seen clearly that the Au nanoparticles quenched the fluorescence of NCDs, which is in agreement with the Raman data. Fluorescence quenching of NCDs can be attributed to several factors. The fluorescence of NCDs might be quenched through FRET. Such mechanism is reasonable as evidence by the spectral overlap of NCDs emission and Au@NCDs absorption.

Application of Au@NCDs as a fluorescent probe for detection of *N*-acetylcysteine

Sensing mechanism

The mechanism of NAC detection by the Au@NCDs probe is schematically illustrated in Figure 8a. In this system, NCDs act as light-harvesting antennae, efficiently absorbing incident photons and generating excited electronic states. The calculated

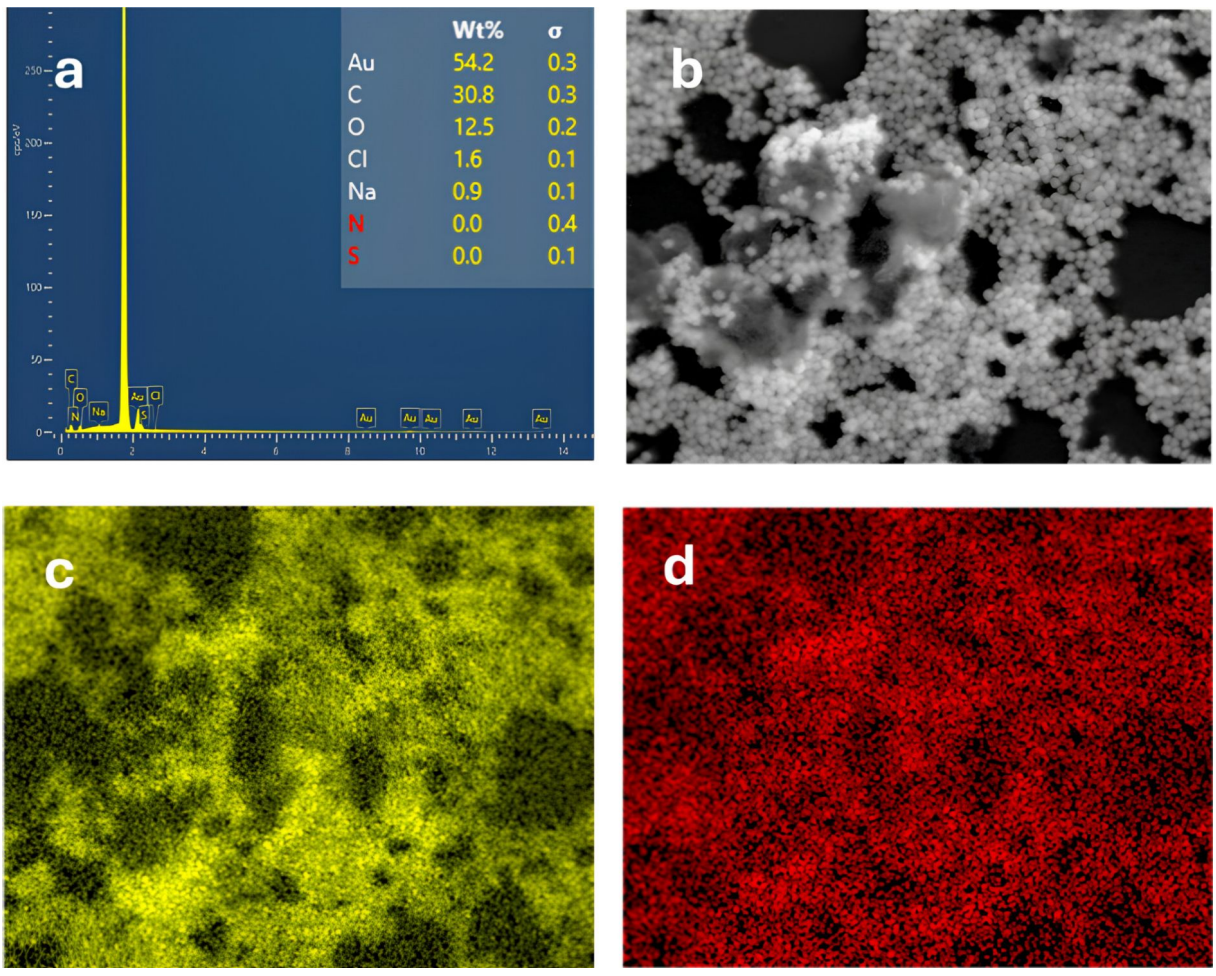


Figure 5: (a) EDX spectrum with elemental weight percentages, (b) SEM image, and elemental mapping of (c) Au and (d) C in Au@NCDs.

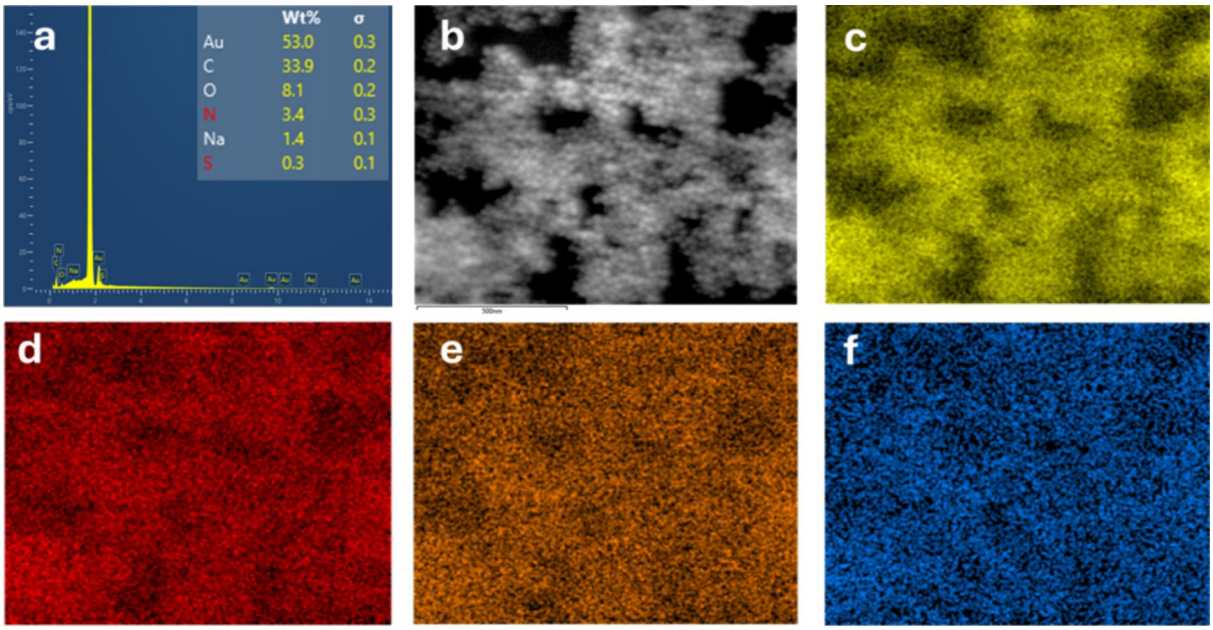


Figure 6: (a) EDX spectrum with elemental weight percentages, (b) SEM image, and elemental mapping of (c) Au, (d) C, (e) S, and (f) N in Au@NCDs-NAC.

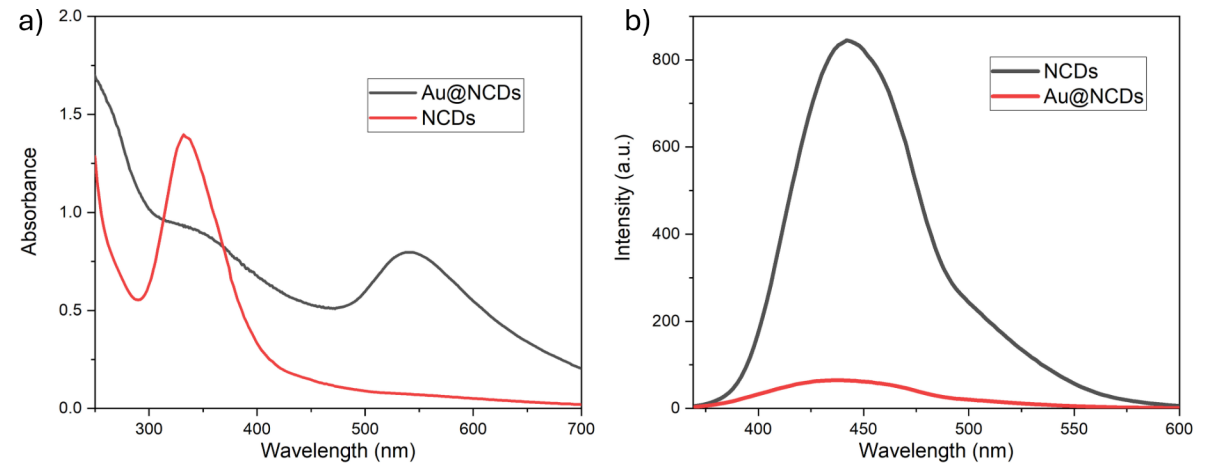


Figure 7: (a) Absorption and (b) photoluminescence spectra of NCDs and Au@NCDs (λ_{ex} = 355 nm).

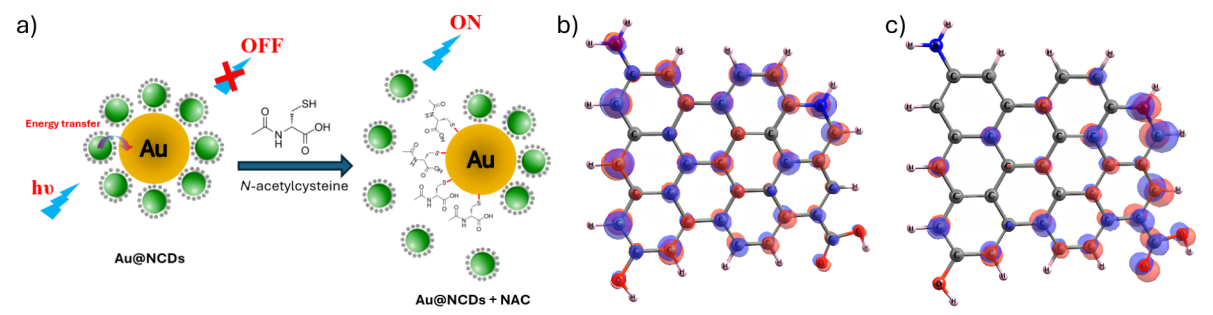


Figure 8: (a) Schematic illustration of the NAC detection mechanism of the Au@NCDs probe, (b, c) spatial distributions of the HOMO and LUMO of NCDs.

frontier orbital energies of NCDs show that the HOMO and LUMO are located at −8.5746 and −8.0600 eV, respectively, corresponding to a relatively small energy gap (≈0.51 eV), which facilitates photoexcitation under mild conditions.

The spatial distribution of the frontier orbitals further reveals that the HOMO is mainly localized on the π-conjugated carbon framework, while the LUMO is more delocalized and extends toward surface functional groups containing heteroatoms such as oxygen and nitrogen, consistent with previous reports on heteroatom-doped carbon dots (Figure 8b,c). This redistribution of electron density upon excitation suggests a partial intramolecular charge transfer character, enhancing the photoactive nature of NCDs and supporting their role as effective energy donors [61]. Rather than undergoing direct electron transfer, the excitation energy is transferred to Au nanoparticles via a non-radiative energy transfer process, likely mediated by plasmonic coupling or dipole–metal interactions. Notably, Au NPs exhibit a near-zero HOMO–LUMO gap, reflecting their metallic electronic structure and quasi-continuous density of states, which renders a discrete frontier orbital description inappropriate. Therefore, Au NPs function as efficient energy acceptors, where the transferred excitation energy is rapidly dissipated through non-radiative relaxation pathways, leading to fluorescence quenching (OFF state).

Upon the introduction of NAC, a ligand exchange process is proposed to occur, in which NAC molecules displace NCDs from the Au NPs surface. This behavior can be attributed to the stronger binding affinity of NAC toward Au. This proposed mechanism is further supported and rationalized by quantum chemical calculations. The computed interaction energies for Au NPs interacting with NCD and NAC provide molecular-level insight into their relative binding strengths, confirming the preferential adsorption of NAC on the Au NPs surface. These results offer a deeper understanding of the microscopic origin of the ligand exchange process and its role in modulating the fluorescence response of the Au@NCDs probe. The interaction energy E_{int} is defined as:

$$E_{int} = E(\text{Au NPs} + \text{substrate}) - E(\text{Au NPs}) - E(\text{substrate}),$$

where (E(Au NPs + substrate), E(Au NPs), E(substrate) denote the total energies of the Au NPs bound to the substrate (NCD, NAC, NCD^-, or NAC^-), the isolated Au NPs, and the isolated substrate molecules (NCD, NAC, NCD^-, or NAC^-), respectively.

First, the interaction between Au NPs and NCD was evaluated. Owing to the presence of several functional groups on its surface, Au NPs can interact with NCD at multiple sites, namely, via the –COOH group (forming AuNCD–COOH), via the $–NH_2$ group (forming AuNCD–NH_2), via the –OH group (forming AuNCD–OH), and through interaction with the deprotonated NCD^- species, assuming proton dissociation from the –COOH group to form AuNCD–COO^-. The optimized structures along with the corresponding E_{int} are presented in Figure 9.

Among the considered configurations, the deprotonated carboxyl group ($–COO^-$) exhibits the strongest interaction with the Au surface, with an E_{int} of −4.270 eV, which can be attributed to enhanced electrostatic attraction and strong Au–O coordination. The relatively short interaction distances (2.19–2.25 Å) further support the formation of stable binding in this configuration. In comparison, the neutral –COOH and $–NH_2$ groups show moderate interaction strengths, suggesting coordination interactions through lone pair donation from O or N atoms to the Au surface. The –OH group exhibits the weakest interaction (E_{int} = −1.467 eV). These results demonstrate that NCDs can bind to Au NPs through multiple functional groups with varying affinities, depending on their chemical state. Importantly, this moderate and tunable binding suggests that the NCD layer on Au NPs may be susceptible to displacement by ligands with stronger binding affinity, which will be further discussed in comparison with NAC.

Building upon the analysis of Au NPs and NCD interactions, it is essential to further examine the binding behavior of NAC on the Au surface in order to understand the ligand exchange mechanism. The optimized structures, together with their corresponding interaction energies (Figure 10), provide detailed insight into the binding characteristics of NAC on the Au NPs surface.

Among these configurations, the thiol group (–SH) plays a dominant role in anchoring NAC onto Au NPs. Even when the –COOH group is initially oriented toward the surface, structural optimization consistently leads to a configuration in which NAC binds through the thiol group, with an interaction energy of approximately −2.575 eV. This value is weaker than the configuration in which NAC simultaneously interacts with the Au surface via both the –SH and –COOH groups, which yields a stronger interaction energy of −3.306 eV. It is noted that, the deprotonated thiolate form ($–S^-$) exhibits significantly stronger binding, with an interaction energy of −6.378 eV, due to enhanced electron donation and stronger Au–S coordination, often accompanied by multipoint bonding interactions with the Au surface. These results clearly indicate that NAC interacts predominantly and most strongly with Au NPs through the sulfur head group. Importantly, when compared with the NCD system, NAC consistently exhibits more negative interaction energies,

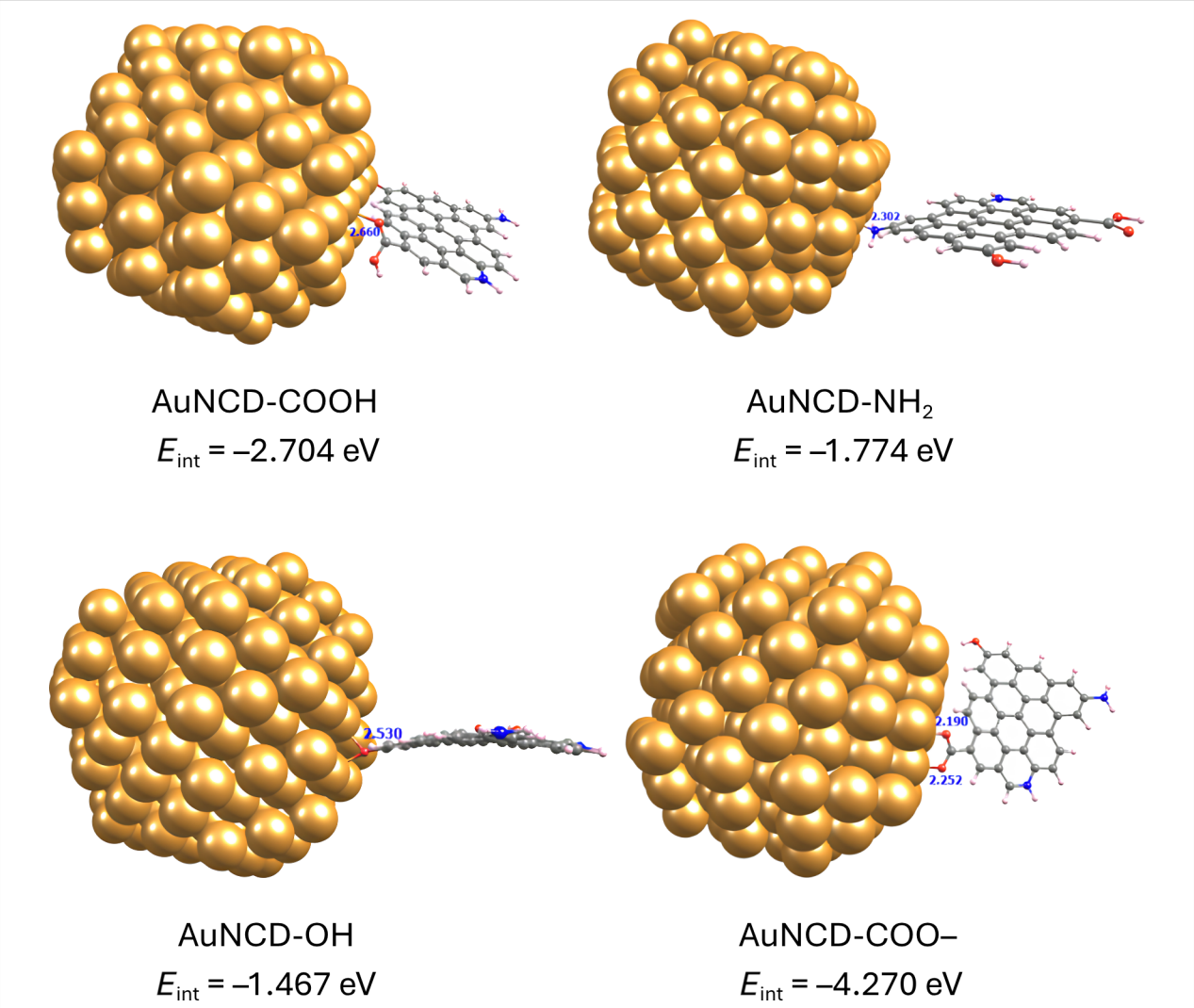


Figure 9: Optimized structures of the binding modes between Au NPs and NCD, along with the corresponding interaction energies.

indicating a stronger binding affinity toward Au NPs. This difference provides a thermodynamic driving force for the ligand exchange process, in which NAC molecules effectively displace NCDs from the Au surface. As a consequence, the displacement of NCDs disrupts the energy transfer pathway between NCDs and Au NPs, thereby restoring the fluorescence signal (ON state) of the sensing system. These results clearly indicate that NAC interacts predominantly and most strongly with Au NPs through the sulfur head group. Importantly, when compared with the NCD system, NAC consistently exhibits more negative interaction energies, indicating a stronger binding affinity toward Au NPs. This difference provides a thermodynamic driving force for the ligand exchange process, in which NAC molecules effectively displace NCDs from the Au surface. The stronger adsorption of NAC increases the separation between NCDs and Au nanoparticles, thereby disrupting the non-radiative energy transfer pathway responsible for fluorescence quenching. Because this energy transfer is highly dependent on the close proximity between NCDs and Au nanoparticles, weakening their interaction suppresses the quenching process and restores the fluorescence emission of NCDs, giving rise to the characteristic OFF–ON fluorescence response. This mechanistic interpretation establishes a direct correlation between the DFT-calculated interaction energies and the experimental photoluminescence results. The proposed ligand exchange mechanism and the associated fluorescence recovery are further supported by experimental evidence from PL spectra (Figure 11).

As shown, pristine NCDs exhibit strong fluorescence emission, whereas the emission intensity is significantly quenched upon formation of Au@NCDs, confirming the effective non-radiative energy transfer from NCDs to Au NPs (OFF state). Upon the introduction of NAC, the fluorescence intensity is partially

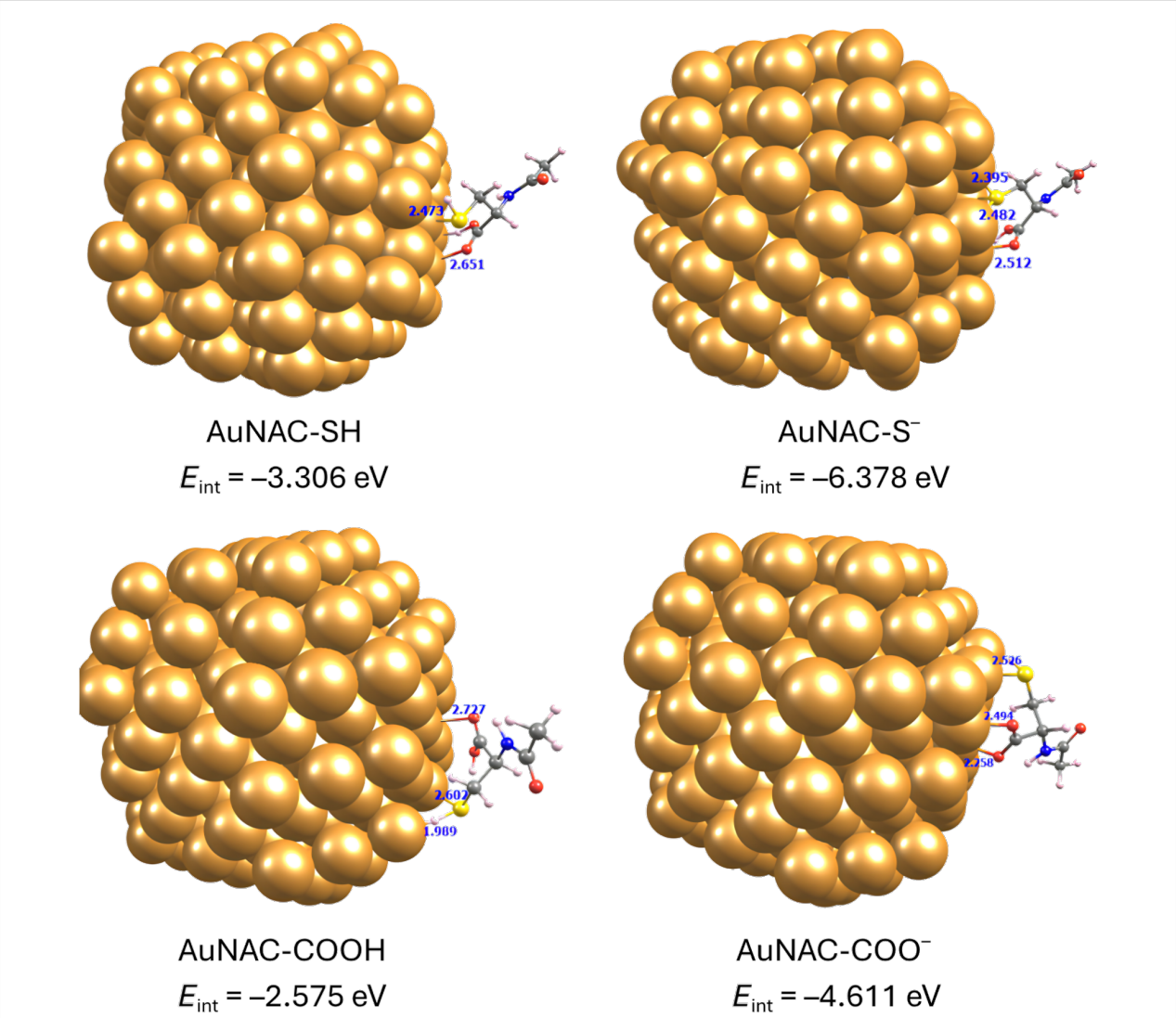


Figure 10: Optimized structures of the binding modes between Au NPs and NAC, along with the corresponding interaction energies.

restored, indicating disruption of the NCD–Au interaction and suppression of the energy transfer pathway. This recovery (ON state) is consistent with the displacement of NCDs from the Au surface by NAC molecules, as suggested by the stronger binding affinity of NAC revealed in the theoretical calculations. Furthermore, previous studies have reported that gold nanocomposites exhibit good selectivity toward NAC, suggesting that the proposed CD@Au nanocomposite is also likely to be selective for NAC [11].

Additional evidence supporting the proposed sensing mechanism can be obtained from Raman spectroscopy (Figure S3 in Supporting Information File 1). In the presence of NAC, the Raman intensity corresponding to the C–H bending (δ_{CH}) vibrations decreases, which can be attributed to the recovery of NCD fluorescence. This behavior is consistent with the fluorescence–Raman interplay, where enhanced fluorescence emission can partially suppress Raman signals. Taken together, both the PL and Raman results are in good agreement with the theoretical findings, providing complementary evidence for the ligand exchange-driven sensing mechanism and the associated OFF–ON fluorescence response of the Au@NCDs probe.

Effect of organic solvent

Figure 12a illustrates the fluorescence response of the Au@NCDs probe in a 25 mg/L NAC solution comprising water and an organic solvent (75:25 v/v). The results indicated the ON fluorescence intensity varied with the solvent environment. The fluorescence response is likely influenced by specific solvation and solvent–surface interactions. Among the tested solvents, the highest fluorescence recovery was observed in the presence of DMF. This behavior was consistently demonstrated through

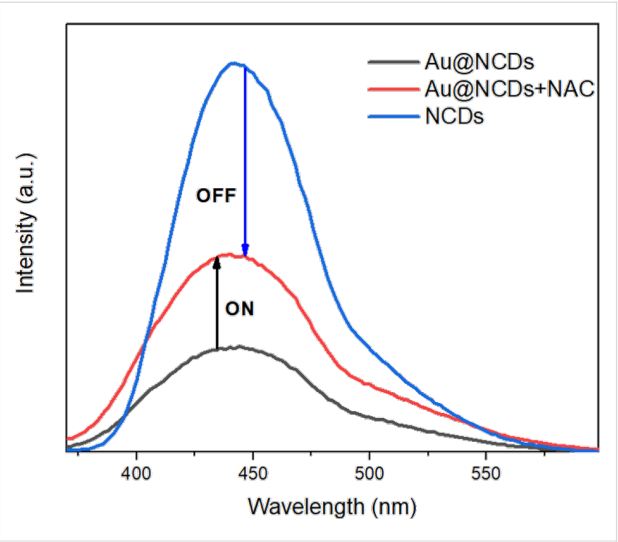


Figure 11: Photoluminescence spectra of NCDs, Au@NCDs, and Au@NCDs after adding NAC.

fluorescence measurements. To minimize the organic solvent usage in the assay, the DMF ratio was investigated across a range of 5% to 25%. As depicted in Figure 12b, a reduction in the DMF percentage led to a diminished recovered fluorescence intensity. Consequently, a DMF ratio of 25% was maintained constant throughout the study.

Spectrofluorimetric determination of *N*-acetylcysteine

As shown in Figure 13a, the fluorescence intensity of the Au@NCDs probe increased progressively with increasing NAC concentration. A good linear relationship was obtained over the concentration range of 4.0–20.0 mg/L (Figure 13b), which is described by the regression equation:

$$\Delta I = 0.8770 \times C_{\mathrm{NAC}} + 0.2068 \left(R^2 = 0.9978\right),$$

where ΔI is the fluorescence intensity change and C_{NAC} is the NAC concentration (mg/L). At concentrations higher than 20.0 mg/L, the fluorescence recovery gradually approached saturation, resulting in a reduced analytical sensitivity.

The limit of detection (LOD) and limit of quantitation (LOQ) of the proposed assay were determined based on the validated calibration range, according to the following equations:

$$\mathrm{LOD} = 3.3 \times \left(\sigma / S\right),$$

$$\mathrm{LOQ} = 10 \times \left(\sigma / S\right).$$

Here, S is the slope of the linear calibration curve, and σ represents the standard deviation of the response (ΔI). The estimated LOD and LOQ were 0.863 mg/L and 2.615 mg/L, respectively. Since the validated calibration range of the proposed method extends from 4.0 to 20.0 mg/L, the calculated LOD and LOQ should be regarded as statistical estimates of the detection and quantification capabilities based on the standard response. Reliable quantitative determination is therefore supported within the validated calibration range, while extension of the calibration curve to lower concentrations would be required to experimentally verify the practical lower limit of quantification. The analytical performance of the proposed assay is comparable to that of previously reported spectrofluorimetric methods for NAC determination [11]. Nevertheless, additional matrix-spike experiments are required for complete method validation and should be included in future studies.

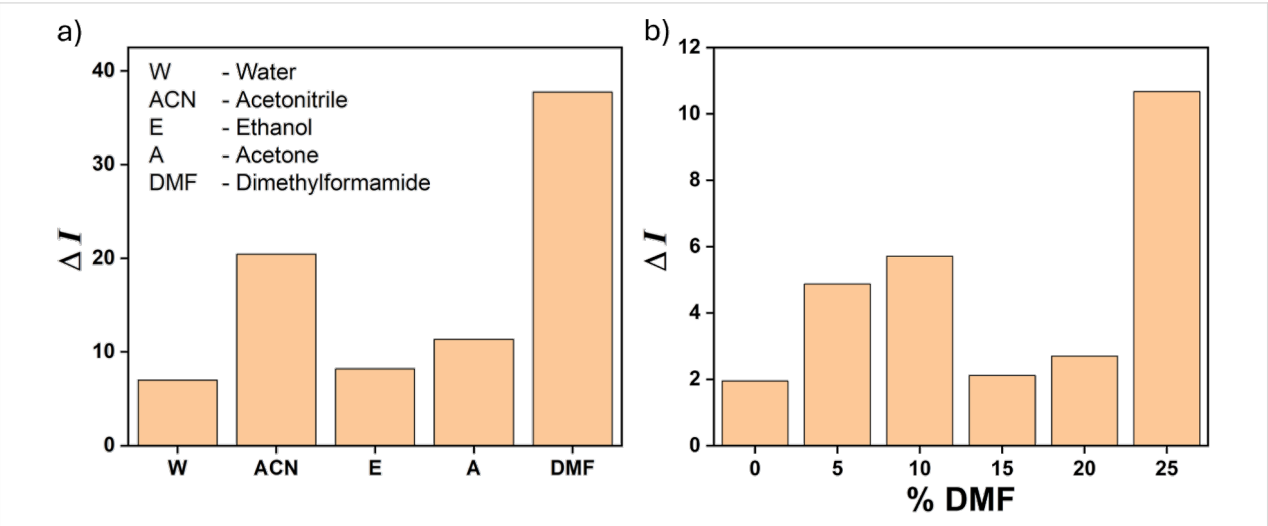


Figure 12: (a) Effect of organic solvent and (b) amount of DMF solvent ratio.

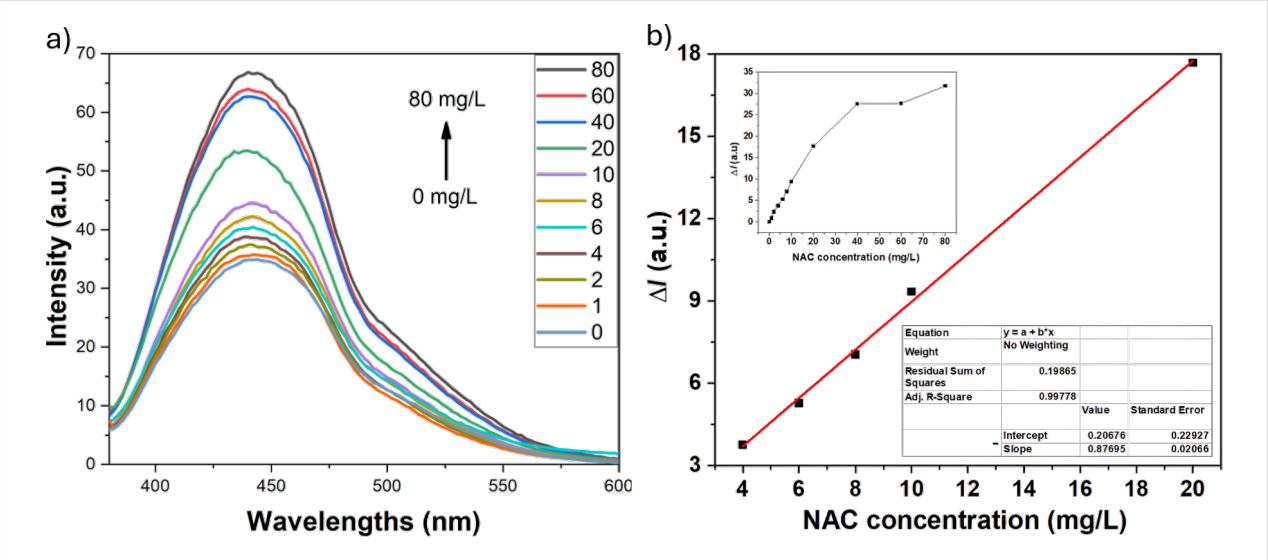


Figure 13: (a) The fluorescence spectra of Au@NCDs + NAC (0–80 mg/L); (b) calibration curve.

Conclusion

NCDs were successfully synthesized via a facile green process based on modified hydrothermal method from fresh lemon juice and urea as precursors. These NCDs function as both reducing and stabilizing agents in the subsequence synthesis of Au@NCDs. The results demonstrate the OFF–ON fluorescence behavior of the Au@NCDs in the absence and presence of *N*-acetylcysteine, a phenomenon attributed to a combination of energy transfer and ligand exchange. This proposed method holds potential for the quantitative determination of *N*-acetylcysteine.

Supporting Information

Supporting Information File 1

Additional information.
[https://www.beilstein-journals.org/bjnano/content/supplementary/2190-4286-17-75-S1.pdf]

Funding

This research is funded by the Ministry of Education and Training of Vietnam under grant number B2025-BKA-15.

Conflict of Interest

The authors declare no competing financial interests.

Author Contributions

Thuy-Huong Nguyen: data curation; formal analysis; investigation; writing – original draft. Van-Nghia Nguyen: funding acquisition; writing – original draft. Ha Thi Thu Nguyen: data curation; formal analysis; investigation; writing – original draft. Ha Ngoc Nguyen: formal analysis. Anh Duc Nguyen: data curation; formal analysis. Tuyen Viet Nguyen: data curation; formal analysis; investigation. Truong Xuan Nguyen: conceptualization; data curation; formal analysis; investigation; methodology; project administration; resources; software; supervision; validation; visualization; writing – review & editing.

ORCID® iDs

Thuy-Huong Nguyen - https://orcid.org/0009-0002-3409-6074
Van-Nghia Nguyen - https://orcid.org/0000-0001-6553-8176
Ha Thi Thu Nguyen - https://orcid.org/0000-0002-9979-2399
Ha Ngoc Nguyen - https://orcid.org/0000-0003-2480-4209
Truong Xuan Nguyen - https://orcid.org/0000-0003-0201-7212

Data Availability Statement

All data that supports the findings of this study is available in the published article and/or the supporting information of this article.

References

1. Prescott, L. F.; Ballantyne, A.; Proudfoot, A. T.; Park, J.; Adriaenssens, P. *Lancet* **1977,** *310,* 432–434. doi:10.1016/s0140-6736(77)90612-2
2. Jones, A. L. *J. Toxicol., Clin. Toxicol.* **1998,** *36,* 277–285. doi:10.3109/15563659809028022
3. Bateman, D. N.; Dear, J. W. *Toxicol. Res. (Oxford, U. K.)* **2019,** *8,* 489–498. doi:10.1039/c9tx00002j
4. Papi, A.; Alfano, F.; Bigoni, T.; Mancini, L.; Mawass, A.; Baraldi, F.; Aljama, C.; Contoli, M.; Miravitlles, M. *Arch. Bronconeumol.* **2024,** *60,* 269–278. doi:10.1016/j.arbres.2024.03.010
5. Douša, M. *J. Pharm. Biomed. Anal.* **2018,** *156,* 1–7. doi:10.1016/j.jpba.2018.04.007

6. Concha-Herrera, V.; Torres-Lapasió, J. R.; García-Alvarez-Coque, M. C. *J. Liq. Chromatogr. Relat. Technol.* **2004,** *27,* 1593–1609. doi:10.1081/jlc-120034094
7. Giljanović, J.; Brkljača, M.; Prkić, A. *Molecules* **2011,** *16,* 7224–7236. doi:10.3390/molecules16097224
8. Kukoc-Modun, L.; Radić, N. *Int. J. Anal. Chem.* **2011,** *2011,* 140756. doi:10.1155/2011/140756
9. Martinović Bevanda, A.; Arapović, A.; Vasilj, M.; Pušić, A.; Talić, S.; Ivanković, A. *Chem. Pap.* **2024,** *78,* 4261–4268. doi:10.1007/s11696-024-03386-6
10. Zhang, H.; Xu, P.; Zhang, X.; Cao, X.; Han, W.; Liu, M.; Liu, X.; Zeng, W. *Chin. Chem. Lett.* **2020,** *31,* 1083–1086. doi:10.1016/j.cclet.2019.10.005
11. Rastegarzadeh, S.; Hashemi, F. *Anal. Methods* **2015,** *7,* 1478–1483. doi:10.1039/c4ay01961j
12. Kuyumcu Savan, E. *Sens. Actuators, B* **2019,** *282,* 500–506. doi:10.1016/j.snb.2018.11.092
13. Mohammadzadeh Jahani, P.; Tajik, S.; Garkani, F. *J. Electrochem. Sci. Eng.* **2024,** *14,* 61–73. doi:10.5599/jese.2039
14. Keyvanfard, M.; Karimi-Maleh, H.; Karimi, F.; Opoku, F.; Kiarii, E. M.; Govender, P. P.; Taghavi, M.; Fu, L.; Aygun, A.; Sen, F. *Sci. Rep.* **2021,** *11,* 18060. doi:10.1038/s41598-021-97725-2
15. Hien, N. K.; Van Bay, M.; Vo, Q. V.; Ngo, S. T.; Nhan, D. T.; Nam, P. C.; Quang, D. T. *RSC Adv.* **2025,** *15,* 46925–46950. doi:10.1039/d5ra07368e
16. Mandani, S.; Sharma, B.; Dey, D.; Sarma, T. K. *Nanoscale* **2015,** *7,* 1802–1808. doi:10.1039/c4nr05424e
17. Ozyurt, D.; Al Kobaisi, M.; Hocking, R. K.; Fox, B. *Carbon Trends* **2023,** *12,* 100276. doi:10.1016/j.cartre.2023.100276
18. Pillar-Little, T. J.; Wanninayake, N.; Nease, L.; Heidary, D. K.; Glazer, E. C.; Kim, D. Y. *Carbon* **2018,** *140,* 616–623. doi:10.1016/j.carbon.2018.09.004
19. Bian, Z.; Gomez, E.; Gruebele, M.; Levine, B. G.; Link, S.; Mehmood, A.; Nie, S. *Chem. Sci.* **2025,** *16,* 4195–4212. doi:10.1039/d4sc05843g
20. Zhang, X.; Jiang, M.; Niu, N.; Chen, Z.; Li, S.; Liu, S.; Li, J. *ChemSusChem* **2018,** *11,* 11–24. doi:10.1002/cssc.201701847
21. Chen, R.; Wang, Z.; Pang, T.; Teng, Q.; Li, C.; Jiang, N.; Zheng, S.; Zhang, R.; Zheng, Y.; Chen, D.; Yuan, F. *Adv. Mater. (Weinheim, Ger.)* **2023,** *35,* 2302275. doi:10.1002/adma.202302275
22. Lan, Y.; Zhou, X.; Zheng, R.; Li, J.; Wang, M.; Wang, D.; Li, S.; Xiao, Y.; Hu, J.; Yang, M.; Li, L.; Wang, M.; Wu, J.; Gao, D. *Mater. Res. Bull.* **2026,** *194,* 113730. doi:10.1016/j.materresbull.2025.113730
23. Sahu, S.; Behera, B.; Maiti, T. K.; Mohapatra, S. *Chem. Commun.* **2012,** *48,* 8835. doi:10.1039/c2cc33796g
24. Yan, H.; Li, P.; Wen, F.; Xu, Q.; Guo, Q.; Su, W. *J. Mater. Res. Technol.* **2023,** *22,* 17–34. doi:10.1016/j.jmrt.2022.11.090
25. Ding, H.; Zhou, X.; Qin, B.; Zhou, Z.; Zhao, Y. *J. Lumin.* **2019,** *211,* 298–304. doi:10.1016/j.jlumin.2019.03.064
26. Kumawat, M. K.; Thakur, M.; Gurung, R. B.; Srivastava, R. *ACS Sustainable Chem. Eng.* **2017,** *5,* 1382–1391. doi:10.1021/acssuschemeng.6b01893
27. Khose, R. V.; Chakraborty, G.; Bondarde, M. P.; Wadekar, P. H.; Ray, A. K.; Some, S. *New J. Chem.* **2021,** *45,* 4617–4625. doi:10.1039/d0nj06259f
28. Shao, R.; Abbas, K.; Osipov, V. Y.; Zhu, H.; Li, Y.; Usama; Bi, H. *Acta Phys.-Chim. Sin.* **2026,** *42,* 100134. doi:10.1016/j.actphy.2025.100134
29. D'souza, S. L.; Chettiar, S. S.; Koduru, J. R.; Kailasa, S. K. *Optik (Munich, Ger.)* **2018,** *158,* 893–900. doi:10.1016/j.ijleo.2017.12.200
30. He, Z.; Yu, J.; Chen, X. *Alexandria Eng. J.* **2024,** *92,* 231–237. doi:10.1016/j.aej.2024.02.041
31. Munusamy, S.; Mandlimath, T. R.; Swetha, P.; Al-Sehemi, A. G.; Pannipara, M.; Koppala, S.; Shanmugam, P.; Boonyuen, S.; Pothu, R.; Boddula, R. *Environ. Res.* **2023,** *231,* 116046. doi:10.1016/j.envres.2023.116046
32. Qi, H.; Qiu, L.; Zhang, X.; Yi, T.; Jing, J.; Sami, R.; Alanazi, S. F.; Alqahtani, Z.; Aljabri, M. D.; Rahman, M. M. *RSC Adv.* **2023,** *13,* 2663–2671. doi:10.1039/d2ra07150a
33. Yuan, Z.; Hu, C.-C.; Chang, H.-T.; Lu, C. *Analyst* **2016,** *141,* 1611–1626. doi:10.1039/c5an02651b
34. Wang, Z.; Ma, L. *Coord. Chem. Rev.* **2009,** *253,* 1607–1618. doi:10.1016/j.ccr.2009.01.005
35. Lu, Z.; Giles, L. W.; Teo, B. M.; Tabor, R. F. *Colloid Interface Sci. Commun.* **2022,** *46,* 100571. doi:10.1016/j.colcom.2021.100571
36. Thakur, N.; Kandwal, P.; Pandey, R. *Ind. Eng. Chem. Res.* **2023,** *62,* 12864–12879. doi:10.1021/acs.iecr.3c01806
37. Lotfy, S.; Aboelnga, M. M.; Moawed, E. A.; Elbayoumy, E. *Nanoscale Adv.* **2026,** *8,* 2426–2449. doi:10.1039/d6na00019c
38. Liu, Y.; Cai, L.; Hao, W.; Cao, Y.; Fang, G.; Wang, S. *Food Chem.* **2026,** *517,* 149446. doi:10.1016/j.foodchem.2026.149446
39. Ma, H.-D.; Liu, J.-Y.; Chen, W.-H.; Wei, Z.; Li, Y.; Liu, Y.-F.; Du, C.-C. *J. Mol. Liq.* **2024,** *406,* 125124. doi:10.1016/j.molliq.2024.125124
40. Raji, F.; Peng, Y. *Adv. Colloid Interface Sci.* **2025,** *345,* 103644. doi:10.1016/j.cis.2025.103644
41. Fernando, A.; Aikens, C. M. *J. Phys. Chem. C* **2015,** *119,* 20179–20187. doi:10.1021/acs.jpcc.5b06833
42. Zhong, J.; Tang, X.; Tang, J.; Su, J.; Pei, Y. *J. Phys. Chem. C* **2015,** *119,* 9205–9214. doi:10.1021/jp511615r
43. Haque, M. H.; Koh, K.; Sohn, H. *Macromolecules* **2023,** *56,* 6396–6406. doi:10.1021/acs.macromol.2c02193
44. Fu, C.; Feng, X.; Tian, H.; Zhang, Y.; Zhai, Z.; Qiu, P.; Hu, C.; Liu, J.; Wang, J. *Appl. Surf. Sci.* **2025,** *702,* 163380. doi:10.1016/j.apsusc.2025.163380
45. Ha, N. T. T.; Thao, V. T.; Ha, N. N. *Photochem. Photobiol. Sci.* **2026,** *25,* 1035–1047. doi:10.1007/s43630-026-00900-5
46. Wang, S.; Huo, X.; Zhao, H.; Dong, Y.; Cheng, Q.; Li, Y. *Chem. Phys. Impact* **2022,** *5,* 100112. doi:10.1016/j.chphi.2022.100112
47. Hinterberger, V.; Damm, C.; Haines, P.; Guldi, D. M.; Peukert, W. *Nanoscale* **2019,** *11,* 8464–8474. doi:10.1039/c9nr01029g
48. Oliveira, A. E. F.; Pereira, A. C.; Resende, M. A. C.; Ferreira, L. F. *Analytica* **2023,** *4,* 250–263. doi:10.3390/analytica4020020
49. García, A.; Papior, N.; Akhtar, A.; Artacho, E.; Blum, V.; Bosoni, E.; Brandimarte, P.; Brandbyge, M.; Cerdá, J. I.; Corsetti, F.; Cuadrado, R.; Dikan, V.; Ferrer, J.; Gale, J.; García-Fernández, P.; García-Suárez, V. M.; García, S.; Huhs, G.; Illera, S.; Korytár, R.; Koval, P.; Lebedeva, I.; Lin, L.; López-Tarifa, P.; Mayo, S. G.; Mohr, S.; Ordejón, P.; Postnikov, A.; Pouillon, Y.; Pruneda, M.; Robles, R.; Sánchez-Portal, D.; Soler, J. M.; Ullah, R.; Yu, V. W.-z.; Junquera, J. *J. Chem. Phys.* **2020,** *152,* 204108. doi:10.1063/5.0005077
50. Perdew, J. P.; Burke, K.; Ernzerhof, M. *Phys. Rev. Lett.* **1997,** *78,* 1396. doi:10.1103/physrevlett.78.1396
51. Ehlert, S. *J. Open Source Software* **2024,** *9,* 7169. doi:10.21105/joss.07169
52. Grimme, S.; Hansen, A.; Brandenburg, J. G.; Bannwarth, C. *Chem. Rev.* **2016,** *116,* 5105–5154. doi:10.1021/acs.chemrev.5b00533

53. Hieu, N. H.; Huyen, N. T.; Thoai, N. D.; Ha, N. N.; Ha, N. T. T. *J. Nanopart. Res.* **2026,** *28,* 49. doi:10.1007/s11051-026-06567-4
54. Tran, T.-Q.; Tran, H.-M.; Nguyen, X.-T.; Nguyen, D.-T.; Giang, P.-L. T.; Nguyen, N.-T. *Top. Catal.* **2023,** *66,* 104–116. doi:10.1007/s11244-022-01732-0
55. Nguyen, N. T.; Nguyen, X. T.; Nguyen, D.-T.; Tran, H. M.; Nguyen, T. M.; Tran, T. Q. *Adsorpt. Sci. Technol.* **2021,** *2021,* 5906248. doi:10.1155/2021/5906248
56. Simões, E. F. C.; Leitão, J. M. M.; da Silva, J. C. G. E. *Microchim. Acta* **2016,** *183,* 1769–1777. doi:10.1007/s00604-016-1807-6
57. Li, X.; Hu, Q.; Yang, K.; Zhao, S.; Zhu, S.; Wang, B.; Zhang, Y.; Yi, J.; Song, X.; Lan, M. *Sens. Actuators, B* **2022,** *371,* 132534. doi:10.1016/j.snb.2022.132534
58. Qin, X.; Lu, Y.; Bian, M.; Xiao, Z.; Zhang, Y.; Yuan, Y. *Anal. Chim. Acta* **2019,** *1091,* 119–126. doi:10.1016/j.aca.2019.09.031
59. Vervald, A. M.; Laptinskiy, K. A.; Chugreeva, G. N.; Burikov, S. A.; Dolenko, T. A. *J. Phys. Chem. C* **2023,** *127,* 21617–21628. doi:10.1021/acs.jpcc.3c05231
60. Korram, J.; Dewangan, L.; Nagwanshi, R.; Karbhal, I.; Ghosh, K. K.; Satnami, M. L. *New J. Chem.* **2019,** *43,* 6874–6882. doi:10.1039/c9nj00555b
61. Kim, N.; Lee, J.; Gu, M.; Kim, B.-S. *Carbon Energy* **2021,** *3,* 590–614. doi:10.1002/cey2.115

License and Terms

This is an open access article licensed under the terms of the Beilstein-Institut Open Access License Agreement (https://www.beilstein-journals.org/bjnano/terms), which is identical to the Creative Commons Attribution 4.0 International License (https://creativecommons.org/licenses/by/4.0). The reuse of material under this license requires that the author(s), source and license are credited. Third-party material in this article could be subject to other licenses (typically indicated in the credit line), and in this case, users are required to obtain permission from the license holder to reuse the material.

The definitive version of this article is the electronic one which can be found at:
https://doi.org/10.3762/bjnano.17.75

BEILSTEIN JOURNAL OF NANOTECHNOLOGY

Room-temperature NO_2 sensing performance of $ZnO/Ti_3C_2T_x$ heterojunctions

Ngo Thi Chau[1,2,3], Quoc Vinh Ho[1,2], Dai Hai Nguyen[1,2], Phan Khanh Thinh Nguyen[*4] and Qui Thanh Hoai Ta[*1,2]

Full Research Paper

Open Access

Address:
[1]Institute of Advanced Technology, Vietnam Academy of Science and Technology, 1B TL29 Street, An Phu Dong Ward, Ho Chi Minh City 700000, Vietnam, [2]Graduate University of Science and Technology, Vietnam Academy of Science and Technology, 18 Hoang Quoc Viet Street, Hanoi 100000, Vietnam, [3]Faculty of Pharmacy, Nguyen Tat Thanh University, 300A Nguyen Tat Thanh Street, Ho Chi Minh City 700000, Vietnam and [4]School of Chemical, Biological, and Battery Engineering, Gachon University, 1342 Seongnamdaero, Sujeong-gu, Seongnam-si, Gyeonggi-do, 13120, Republic of Korea

Email:
Ngo Thi Chau - ntchau@ntt.edu.vn;
Quoc Vinh Ho - hovinh34@gmail.com;
Dai Hai Nguyen - nguyendaihai0511@gmail.com;
Phan Khanh Thinh Nguyen* - thinhnpk@gachon.ac.kr;
Qui Thanh Hoai Ta* - tathanhhoaiqui2292@gmail.com

* Corresponding author

Keywords:
gas sensor; room temperature; $ZnO/Ti_3C_2T_x$ composites

Beilstein J. Nanotechnol. **2026,** *17,* 1159–1169.
https://doi.org/10.3762/bjnano.17.79

Received: 30 April 2026
Accepted: 22 July 2026
Published: 19 August 2026

This article is part of the thematic issue "Innovative nanomaterials for next-generation bio- and chemosensing".

Guest Editor: Q. T. Duong



© 2026 Chau et al.; licensee Beilstein-Institut.
License and terms: see end of document.

Abstract

In recent years, metallic $Ti_3C_2T_x$ MXenes have garnered considerable attention in the realm of gas sensors owing to their distinctive characteristics, including high conductivity, inherent hydrophilicity, and abundant surface termination groups. Nonetheless, $Ti_3C_2T_x$-based sensing composites encounter challenges related to response/recovery time and low sensitivity, thereby limiting their applicability across diverse environmental conditions. Addressing these limitations, we present the synthesis of $ZnO/Ti_3C_2T_x$ nanocomposites via a facile method for gas sensing applications. The optimized composite exhibits a notable response of around 6.1% to 5 ppm NO_2, coupled with remarkable selectivity at ambient temperatures. Moreover, the sensor demonstrates exceptional reproducibility across multiple testing iterations. The observed enhancement in gas sensing performance is attributed to the abundance of oxygen vacancies and surface functional groups within the $ZnO/Ti_3C_2T_x$ composites, which facilitate robust interactions with NO_2 molecules. These findings underscore the efficacy of $ZnO/Ti_3C_2T_x$ nanocomposites as a viable strategy for enhancing the gas sensing properties of $Ti_3C_2T_x$-based sensors.

Introduction

Nowadays, increasing attention is paid to the early detection and prevention of chemical leaks and accidental releases, highlighting the importance of identifying trace-level chemicals in gaseous emissions [1-3]. Notably, a significant subset of such accidents involves the leakage of toxic gases and combustible substances, including carbon monoxide (CO), sulfur dioxide (SO_2), carbon dioxide (CO_2), ammonia (NH_3), and nitrogen dioxide (NO_2) [4-6]. Of these, NO_2 stands out as a ubiquitous emission arising from daily activities and vehicular operations, primarily attributed to fossil fuel combustion and engine emissions. Instances of NO_2 exposure at low concentrations (≈10 ppm) have been associated with adverse health effects, including nasal and ocular irritation as well as throat discomfort [7,8]. Prolonged exposure to elevated NO_2 concentrations can bring about severe respiratory ailments such as pulmonary edema and asthma, with fatal outcomes observed at concentrations exceeding 100 ppm. Furthermore, the release of NO_2 into the natural environment poses a significant risk, potentially leading to soil and water contamination through acid rain deposition [9-11].

In recent decades, research on two-dimensional (2D) layered materials has grown significantly owing to their unique physicochemical properties. Materials such as graphene, black phosphorus, transition metal dichalcogenides, and MXenes have attracted considerable attention for a wide range of applications [12-14]. MXenes have emerged as particularly promising candidates in the realm of gas sensing owing to their distinctive attributes [15]. The discovery of $Ti_3C_2T_x$ MXene in 2011, achieved through the selective etching of Ti_3AlC_2 using LiF and HCl, marked a pivotal milestone in the exploration of MXene-based gas sensors [16,17]. $Ti_3C_2T_x$ MXene has exhibited commendable sensor performance at ambient temperatures, characterized by a low signal-to-noise ratio and high electron conductivity, rendering it a subject of extensive investigation in sensing applications. Nonetheless, the inherent limitations of MXenes, including suboptimal sensitivity and long recovery times, necessitate remediation prior to broader application [18,19].

In particular, the amalgamation of $Ti_3C_2T_x$ MXene with metal oxide semiconductors has garnered considerable attention as a strategy to augment the NO_2 sensing capabilities of $Ti_3C_2T_x$-based gas sensors, attributed to the formation of Schottky barriers and the increase of surface area [20,21]. For instance, Choi et al. synthesized a TiO_2@$Ti_3C_2T_x$ composite utilizing an in situ oxidation technique and modulating oxidation parameters to regulate the formation of Schottky barriers; the composite exhibited superior NO_2 responsiveness compared to pristine $Ti_3C_2T_x$ MXene [22]. Ta et al. reported promising results with a heterostructure comprising Si and MXene-derived TiO_2, demonstrating robust NO_2 sensing performance [23]. Similarly, Sun et al. employed Co_3O_4 nanoparticle-based polyethyleneimine-functionalized $Ti_3C_2T_x$ nanosheets, showcasing exemplary sensing response characteristics and rapid response/recovery times towards NO_2 gas [24].

Furthermore, n-type ZnO has garnered significant traction as a NO_2 sensor owing to its wide bandgap energy (3.37 eV), abundant oxygen vacancies, and exceptional chemical stability [25,26]. Moon et al. [27] synthesized a rGO/ZnO composite for NO_2 detection at room temperature, while Song et al. [28] employed a hydrothermal approach to fabricate ZnO nanofibers, yielding enhanced NO_2 sensing performance. Notably, ultraviolet (UV) irradiation has emerged as an efficacious strategy to enhance the recovery kinetics of gas-sensitive materials by facilitating desorption reactions. Zhang et al. demonstrated the efficacy of TiO_2/SnO_2 under UV illumination, manifesting superior response/recovery kinetics compared to sensors based solely on TiO_2 nanostructures [9]. In other words, the synergistic integration of $Ti_3C_2T_x$ MXene with metal oxide semiconductors, alongside innovative strategies such as combination, Schottky barriers, and UV irradiation, holds promise for advancing the development of robust and efficient NO_2 sensing platforms, thereby contributing to enhanced environmental monitoring and public health safeguards [29-31]. Further research endeavors aimed at refining sensor materials and elucidating underlying mechanisms are warranted to realize the full potential of these novel sensing architectures in real-world applications. Motivated by the promising outcomes observed with n-type ZnO nanomaterials, the integration of $Ti_3C_2T_x$ MXene and ZnO offers a compelling avenue to capitalize on the synergistic effects of Schottky junction formation, leveraging the distinctive sensing properties inherent in both components to enhance NO_2 sensing performance.

In this work, we describe a simple synthesis approach for fabricating ZnO/$Ti_3C_2T_x$ composite materials, involving the physical combination of ZnO nanostructures and $Ti_3C_2T_x$ MXene. This simplified technique serves to mitigate the oxidation tendencies of MXene while promoting the formation of interactions with ZnO nanorods. The optimized heterostructures exhibit enhanced NO_2 sensing activity at ambient temperatures, presenting a viable strategy for advancing gas sensing technologies.

Results and Discussion

Crystal structural and morphological studies

Figure 1a displays the XRD patterns of pure $Ti_3C_2T_x$ MXene and ZnO/$Ti_3C_2T_x$ composite. The XRD pattern of pristine $Ti_3C_2T_x$ MXene exhibits a strong characteristic (002) reflection

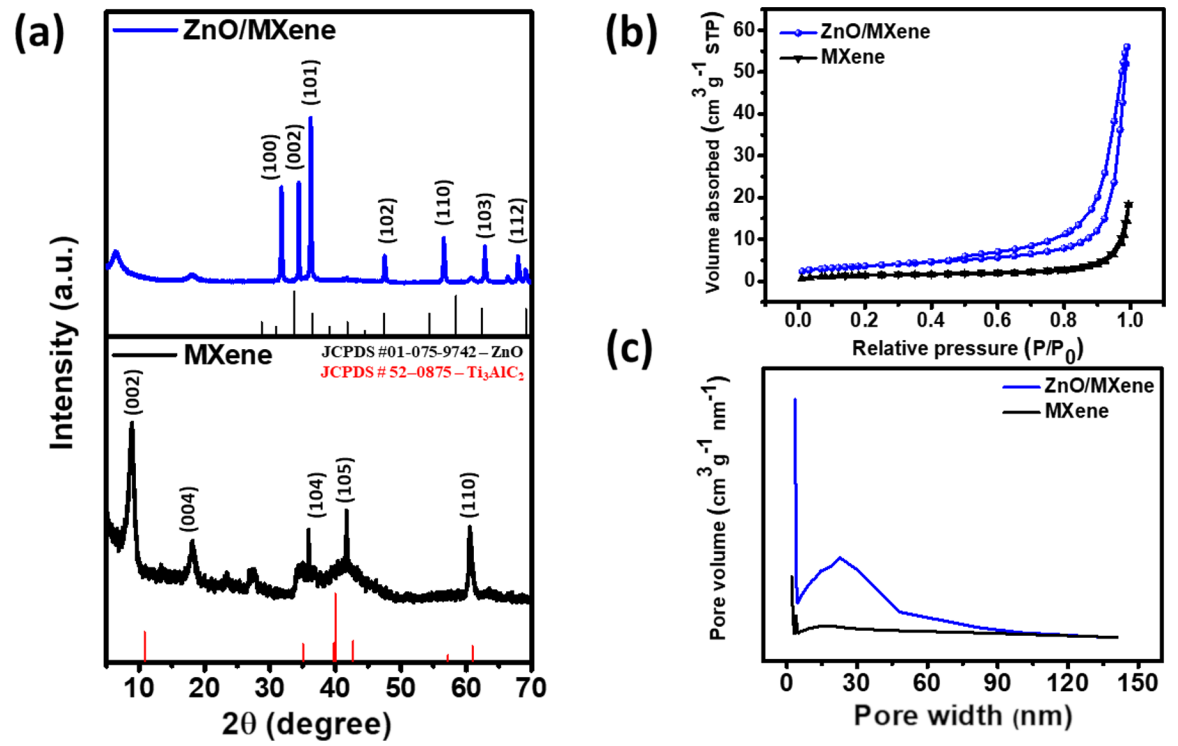


Figure 1: (a) XRD patterns, (b) nitrogen adsorption/desorption isotherms, and (c) pore-size distributions of pure $Ti_3C_2T_x$ MXene and ZnO/$Ti_3C_2T_x$ composites.

at 2θ = 8.9°, together with weaker diffraction peaks at approximately 18.2°, 36.0°, 41.1°, and 60.8°, corresponding to the (004), (104), (105), and (110) planes of $Ti_3C_2T_x$, respectively (JCPDS no. 52-0875). The intense (002) peak, accompanied by the absence of the characteristic Ti_3AlC_2 MAX phase reflections, confirms the selective removal of the Al atomic layers during the etching process and the formation of $Ti_3C_2T_x$ MXene. For the ZnO/$Ti_3C_2T_x$ composite, the prominent diffraction peaks located at 2θ = 31.7°, 34.4°, and 36.2° are indexed to the (100), (002), and (101) planes of hexagonal wurtzite ZnO (JCPDS no. 01-075-9742), while the remaining reflections are also in good agreement with the standard ZnO pattern, confirming the crystallization of ZnO nanostructures [32-34]. Notably, the characteristic (002) peak of $Ti_3C_2T_x$ shifts from 8.9° to 6.7° after ZnO loading and becomes broader. According to Bragg's law, this shift toward a lower diffraction angle corresponds to an increase in the interlayer spacing, suggesting that ZnO nanostructures are effectively intercalated between adjacent MXene nanosheets. The enlarged interlayer distance suppresses the restacking of $Ti_3C_2T_x$ layers, exposes more accessible active sites, and facilitates charge transport and ion diffusion within the composite structure. Moreover, no additional diffraction peaks associated with impurity phases or reaction by-products are detected, demonstrating the phase purity of the synthesized ZnO/$Ti_3C_2T_x$ composite.

The pore size distribution and specific surface area (SSA) of selected samples were further determined using nitrogen adsorption/desorption, as shown in Figure 1b. The plots illustrate a type-IV isotherm at relative pressures from 0.6 to 1.0 with a hysteresis cycle. The SSA of the composite analyzed by the BET method is 12.8 m^2/g, which is more than twice that of pure $Ti_3C_2T_x$ (5.1 m^2/g). This substantial enhancement in SSA can be attributed to the introduction of ZnO nanostructures within the MXene layers as well as to synergistic effects of the composite constituents, which provide more active sites for interaction with gas molecules. The pore size distribution of the composite ranged from approximately 2 to 120 nm, ascribing a hierarchical porous structure composed of both mesopores (2–50 nm) and macropores (>50 nm) (Figure 1c).

Figure 2 displays FESEM images of the pure $Ti_3C_2T_x$ MXene, pristine ZnO nanostructures, and ZnO/$Ti_3C_2T_x$ composites. The pure MXene shows a characteristic accordion-like morphology, in which both few-layered nanosheets and multilayered stacked lamellae with enlarged interlayer spacing were observed, which is typical of etched MXene materials (Figure 2a). ZnO prepared by the chemical bath deposition method displays a flower-like morphology consisting of radially assembled rod-like nanostructures (Figure 2b). After composite formation, the ZnO/$Ti_3C_2T_x$ composite retains the structure of MXene, while

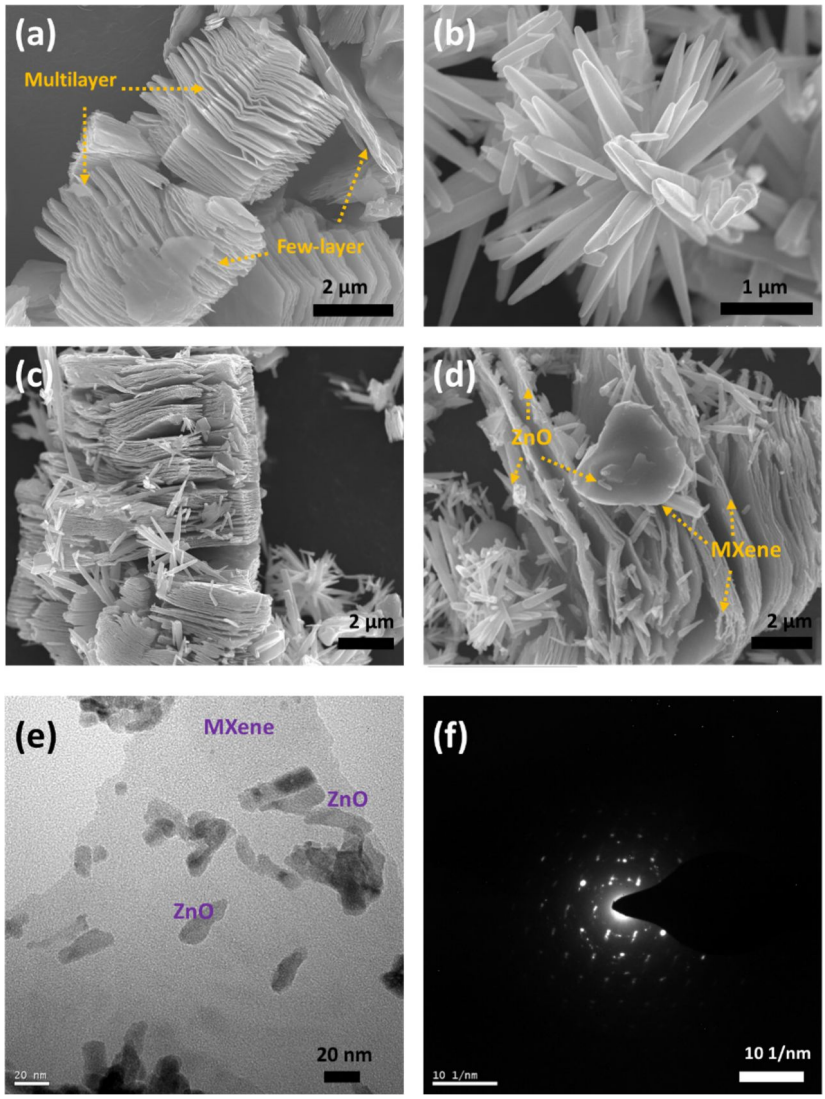


Figure 2: FESEM images of (a) pure $Ti_3C_2T_x$ MXene, (b) pristine ZnO, and (c, d) ZnO/$Ti_3C_2T_x$ composites. (e) TEM image and (f) corresponding selected-area electron diffraction pattern of ZnO/$Ti_3C_2T_x$ composites.

ZnO nanostructures are randomly anchored onto the surface and interlayer spaces of the MXene sheets (Figure 2c,d). Such an intimate interfacial contact is expected to facilitate efficient charge transfer and provide abundant active sites for gas sensing. The TEM image further confirms the decoration of ZnO nanostructures on a locally exfoliated $Ti_3C_2T_x$ MXene nanosheet, indicating that partial exfoliation of the MXene occurred during sample preparation. Moreover, the corresponding selected-area electron diffraction pattern displays distinct diffraction rings, indicating the crystalline nature of ZnO/$Ti_3C_2T_x$ composite (Figure 2e,f).

In the hierarchical structure, ZnO plays an important role as a catalytic component. We analyzed the structure of ZnO/$Ti_3C_2T_x$ using SEM-EDS mapping to observe the decoration of ZnO relative to $Ti_3C_2T_x$ MXene. As shown in Figure 3, the elemental mapping of the composite shows that $Ti_3C_2T_x$ nanosheets constitute the framework, and ZnO nanostructures were finely decorated throughout the bulk system. The elements Zn, O, Ti, and C appear in the spectra, which further confirms that ZnO nanostructures are effectively contained in the composite.

Optical properties

Raman spectroscopy was performed on selected samples to study their characteristic vibrational modes, as shown in Figure 4a,b. For the ZnO sample, strong peak intensities are observed at 327 and 415 cm^{-1}, confirming the presence of wurtzite-phase ZnO, with multiple-phonon scattering E_g and the high-frequency E_2 mode, respectively [35]. Peaks located around 230 cm^{-1} (ω_1), 405 cm^{-1} (ω_2), and 607 cm^{-1} (ω_3) are

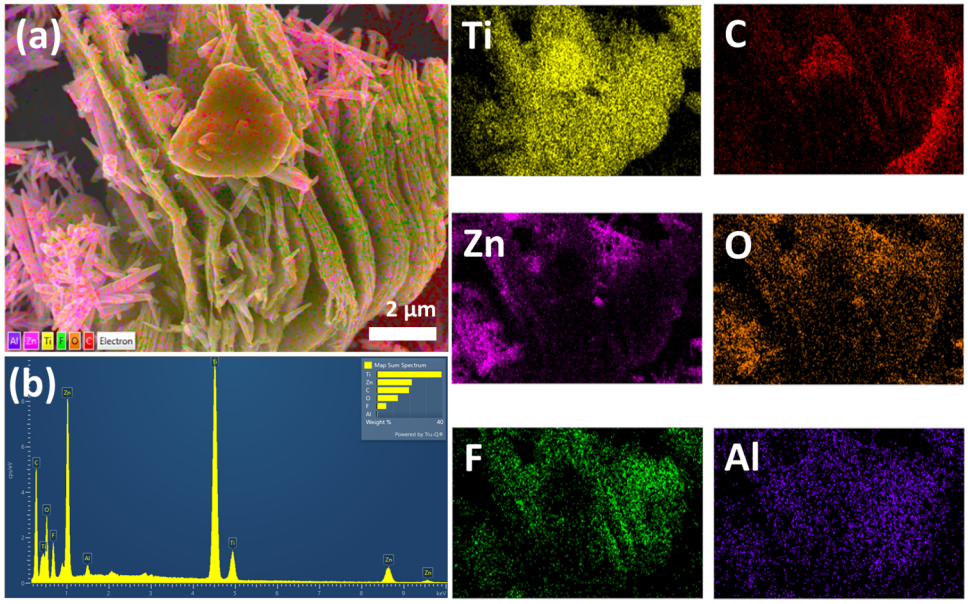


Figure 3: (a) Elemental mapping images, (b) EDS images of ZnO/$Ti_3C_2T_x$ composites.

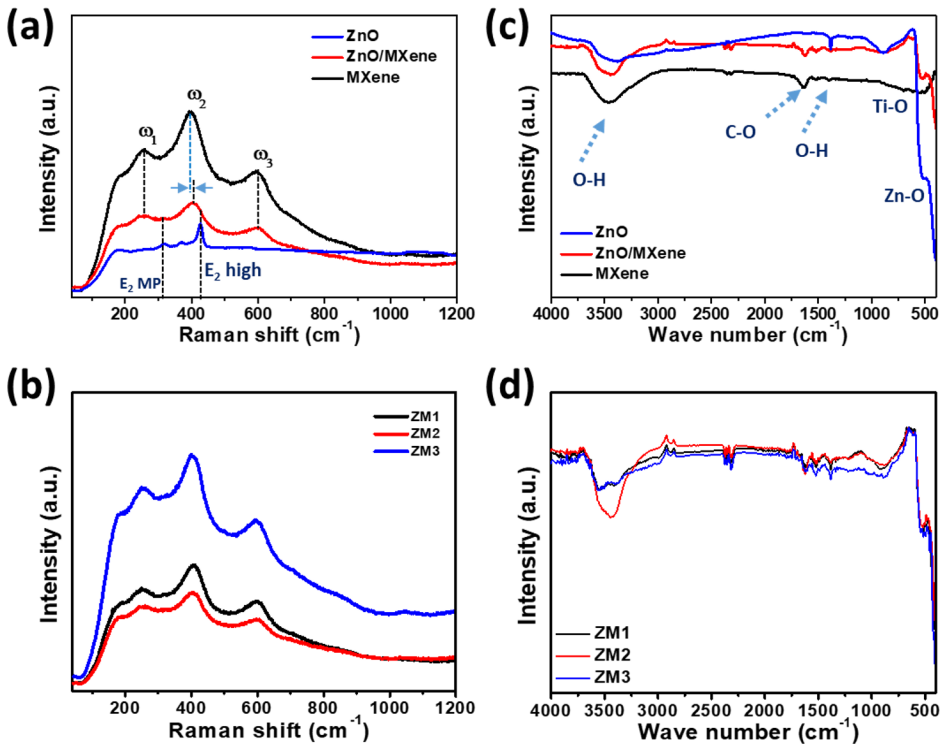


Figure 4: (a,b) Raman spectra, and (c,d) FTIR of synthesized samples.

attributed to titanium carbide vibrational modes in the ZnO/MXene composite, while the vibrational modes at 327 and 415 cm^{-1} overlap with those of ZnO [36]. Notably, with the introduction of ZnO, the highest Raman signal for MXene in the composite exhibited a slight shift towards higher wavenumbers compared to pure MXene, preliminarily suggesting the formation of Ti–O–Zn and Zn–Ti bonds, which could act as diffusion bridges to facilitate electron transport [37,38].

In addition, FTIR measurements were conducted for the synthesized samples, as shown in Figure 4c,d. The spectrum of pure ZnO exhibits characteristic bands at 400 cm^{-1}, corresponding to Zn–O bonds in ZnO, and at 3500 cm^{-1}, indicating the stretching vibration of the O–H groups. For $Ti_3C_2T_x$, the presence of Ti–O bending groups with mode A_{2u} (550 cm^{-1}), O–H bending (1450 cm^{-1}), and O–H stretching (3490 cm^{-1}) is observed [39]. After the introduction of ZnO onto the surface of the $Ti_3C_2T_x$ MXene composite, all corresponding peaks are clearly visible in the spectra. These results confirm the successful growth of ZnO within the composite.

The surface chemical states and binding energies of the optimized sample were analyzed using X-ray photoelectron spectroscopy. As shown in Figure 5a, the survey spectrum of ZnO/$Ti_3C_2T_x$ confirms the coexistence of Ti, C, Zn, and O on the surface of the composite, consistent with the EDS mapping results. For the Ti 2p region (Figure 5b), the main peak at 454.1 eV is assigned to Ti–C bonds, while the peaks at 458.2 and 460.3 eV correspond to Ti–O bonds, respectively [40,41]. The C 1s spectrum (Figure 5c) displays binding energies of 280.8, 284.2, and 288.1 eV, corresponding to Ti–C, C–Ti–$(OH)_y$, and C=O/C–F bonds, respectively [42]. The high-resolution Zn 2p spectra (Figure 5d) exhibit spin–orbit doublets at 1021.2 eV (Zn $2p_{3/2}$) and 1044.1 eV (Zn $2p_{1/2}$), which are characteristic of Zn^{2+} in ZnO [43]. The O 1s spectrum revealed components attributed to chemisorbed oxygen species (531.6 eV), lattice oxygen (529.8 eV), and oxygen vacancies (530.7 eV), suggesting the presence of abundant hydrophilic surface terminations (T_x) [44] (Figure 5e). These enriched oxygen species are expected to provide active sites for target gas interactions, thereby enhancing the sensor response.

Gas sensing activities

Gas sensing measurements were carried out using the as-prepared samples. Figure 6a depicts the response and recovery value of pure $Ti_3C_2T_x$ and ZnO/$Ti_3C_2T_x$ sensors to 5 and 10 ppm NO_2 at room temperature. No response was obtained for pure MXene, ascribing its metallic properties. In contrast, the ZnO/$Ti_3C_2T_x$ sensor revealed a higher response to NO_2 in comparison with the pure $Ti_3C_2T_x$ sensor under the same conditions. The response value of ZM1, ZM2, and ZM3 exposed to concentrations of 5 ppm (10 ppm) NO_2 were calculated around 2.5 (4.5%), 6.2 (12.1%), and 3.1 (3.6 %), respectively. ZM2 was identified as the optimal ratio for sensor performance and thus selected for subsequent testing. The NO_2 sensing ability of pristine ZnO was difficult to assess due to its large resistance at room temperature. ZM2 was exposed to various concentrations of NO_2 at room temperature, and the response value of ZM2 increased with the increase of NO_2 concentration from 5 to 100 ppm. The sensor response increased progressively with increasing NO_2 concentration and exhibited an approximately linear trend (R^2 = 0.857). A slight deviation from linearity was observed at NO_2 concentration above 50 ppm, suggesting the onset of response saturation (Figure 6b).

Figure 6c depicts the three-cycle test for the optimized ZnO/$Ti_3C_2T_x$ sensor (ZM2) to 25 ppm NO_2, demonstrating good

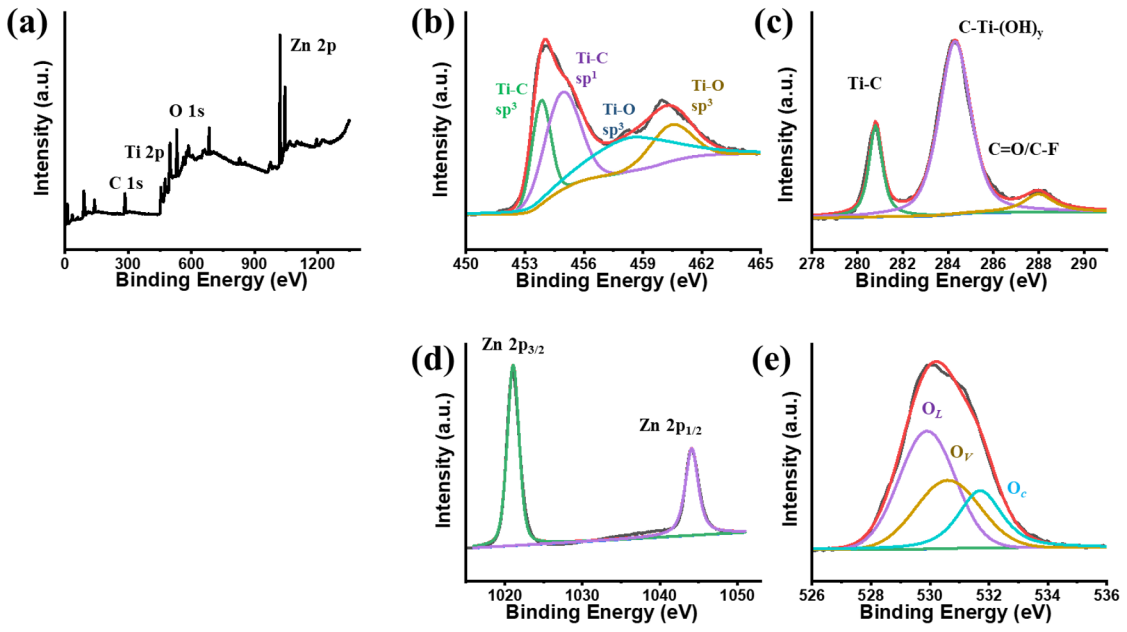


Figure 5: (a) The XPS spectra of selected ZnO/$Ti_3C_2T_x$ composite, (b) Ti 2p, (c) C 1s, (d) Zn, (e) O 1s.

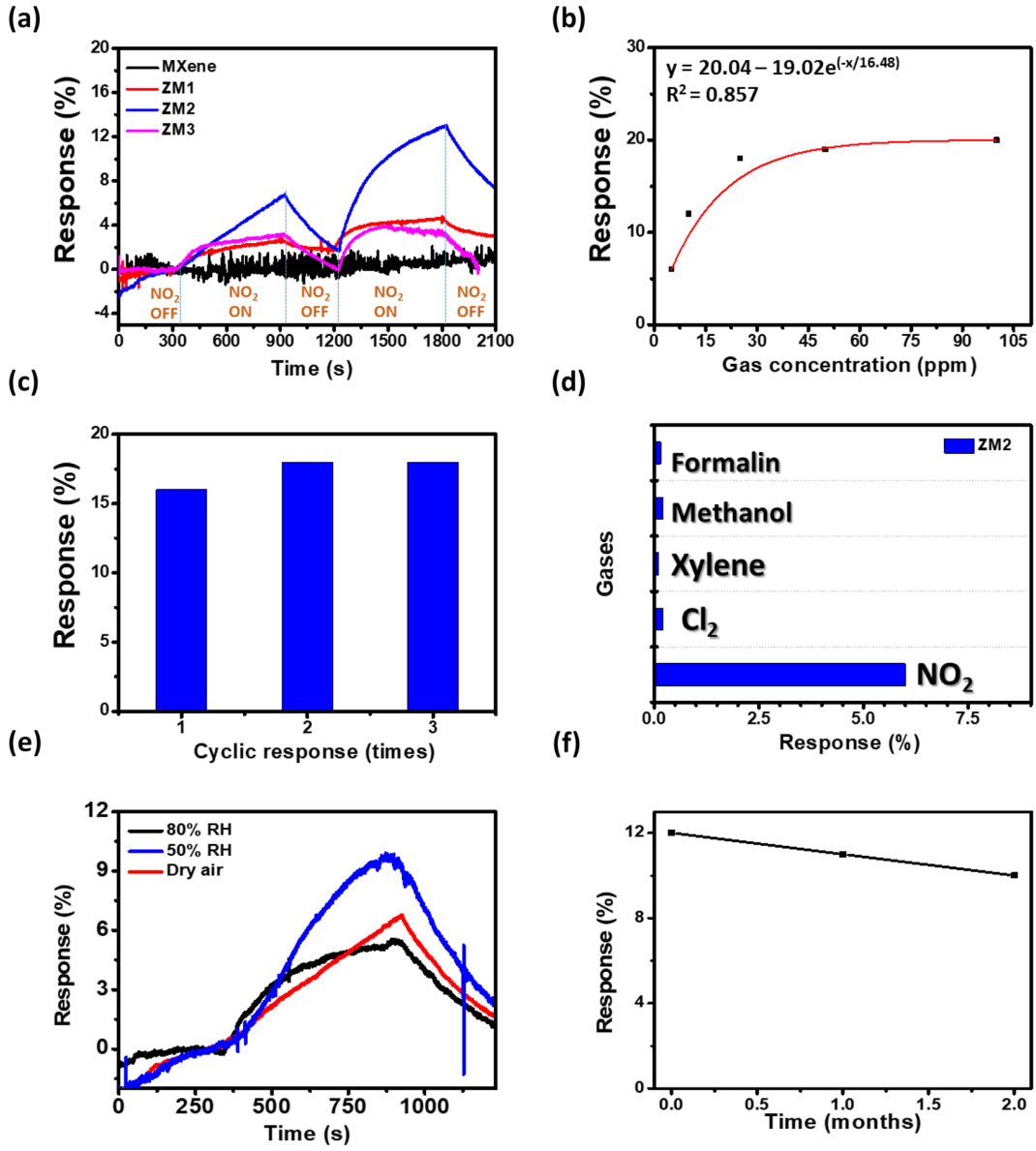


Figure 6: Gas sensing performance of (a) synthesized samples toward NO_2 (5–10 ppm), (b) response value of ZM2 at different concentrations (5–100 ppm), (c) stability test of ZM2 toward NO_2 (25 ppm), (d) selectivity properties of ZM2 sensor using different gases (5 ppm). Response value of ZM2 at (e) different relative humidity of NO_2 (5 ppm) and (f) after 2 months of storage toward NO_2 (10 ppm).

reproducibility without any prominent change. Moreover, the selectivity of ZM2 sensor to different gases was conducted for various gases, including NO_2, Cl_2, xylene, methanol and formalin, under similar conditions (5 ppm). As shown in Figure 6d, the ZM2 sensor exhibited high selectivity for NO_2 molecules compared to other gases.

Relative humidity (RH) plays a critical role in gas sensing performance. Therefore, the response of the ZM2 composite under varying humidity levels was evaluated, as illustrated in Figure 6e. The ZM2 sensor exhibited the highest response at 50% RH for 5 ppm NO_2. At low RH, the excellent humidity tolerance of the composite is attributed to its functional groups, which form weak hydrogen bonds with H_2O molecules and provide –OH and –O groups that facilitate electron transport through the inherent hydrophilicity of the surface functional groups. As RH increases, the response value gradually decreases. This decline is ascribed to the physisorption of H_2O molecules on the sensor surface, which hinders NO_2 adsorption. Moreover, the interaction between H_2O and NO_2 molecules impedes the direct interaction between chemisorbed oxygen species and the target gas, thereby modulating ionic conduction within the sensing material and ultimately reducing the gas response. As shown in Figure 6f, the sample exhibits a slight

decrease in sensing performance after two months of storage. This degradation can be attributed to surface oxidation and the deactivation of active sites on the sample surface.

The sensor response performance of previously reported NO_2 sensors is compared in Table 1. Although the ZM2 sensor developed in this study does not exhibit the highest response, it remains a promising candidate for NO_2 detection at room temperature.

Plausible mechanism

The $ZnO/Ti_3C_2T_x$ composite exhibited enhanced NO_2 sensing performance in comparison with pure ZnO and $Ti_3C_2T_x$ MXene. Since the pristine $Ti_3C_2T_x$ sensor displayed a negligible response toward NO_2, the enhanced sensing performance of the heterostructures can be ascribed to the synergistic interfacial interactions of components. First, $Ti_3C_2T_x$ possesses a higher work function (4.2 eV) than ZnO (3.8 eV) [54], so electrons spontaneously flow from ZnO to $Ti_3C_2T_x$ MXene site until Fermi level equilibrium is established. This charge redistribution induces upward band bending in ZnO and leading to the formation of an interfacial electron depletion layer at the $ZnO/Ti_3C_2T_x$ interface.

When the $ZnO/Ti_3C_2T_x$ composites were exposed to synthetic air, oxygen molecules were chemisorbed on the sensor surface. As a result, O_2 molecules could trap the free electrons from the $ZnO/Ti_3C_2T_x$ to create a series of oxygen ionic species (O_2^- and O^{2-}) [55]. In synthetic air, the extraction of electrons further widens the electron depletion layer, resulting in an increase in the electrical resistance of sensing layer.

NO_2 acts as strong electron acceptor; the NO_2 molecules tend to react with adsorbed oxygen and withdraw electrons, resulting in the electron depletion layer becoming wider, upward band bending in ZnO, and an increase in the sensor's resistance (Figure 7). In addition, the oxygen vacancies of ZnO could facilitate the adsorption process, which supports oxygen adsorp-

Table 1: NO_2 sensor performance of MXene-based composites.

Composites	Response	Gas concentration	Operation temperature	Ref.
ZnO MOF/$Ti_3C_2T_x$	46.3%	500 ppb	180 °C	[45]
CuO/TiO_2/$Ti_3C_2T_x$	25%	100 ppm	UV irradiation	[46]
CuO/$Ti_3C_2T_x$	57%	100 ppm	RT	[47]
CuO/TiO_2/$Ti_3C_2T_x$	15.3%	10 ppm	RT	[48]
Cr_2O_3/TiO_2/$Ti_3C_2T_x$	no response	10 ppm	RT	[49]
N doped $Ti_3C_2T_x$	1.5%	100 ppm	RT	[50]
In_2O_3/$Ti_3C_2T_x$	4%	5 ppm	RT	[51]
SnO_2/Nb_2CT_x	13.5%	100 ppm	RT	[52]
SnS_2/$Ti_3C_2T_x$	5.9%	10 ppm	RT	[53]
$ZnO/Ti_3C_2T_x$	12.1%	10 ppm	RT	this work

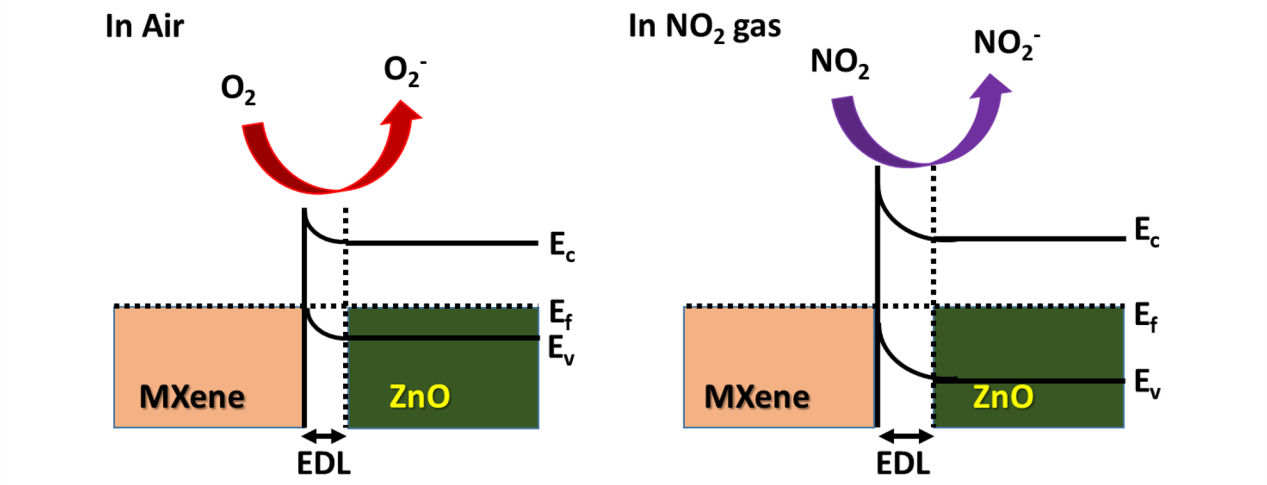


Figure 7: Band structures of $ZnO/Ti_3C_2T_x$ heterostructure in air and in NO_2.

tion and facilitates charge transfer. Moreover, the functional groups of MXene (–O, –OH, –F) offer abundant favorable sites for NO_2 through hydrogen bonding, thereby facilitating NO_2 adsorption and interfacial charge transfer [56]. The adsorbed NO_2 molecules further withdraw electrons from MXene, contributing to the enlargement of the electron depletion layer of the sensor layer [45,57]. The gas sensing reactions can be summarized as follows:

$$O_2(g) \rightarrow O_2(ads)$$
$$O_2(ads) + e^- \rightarrow O_2^-(ads)$$
$$NO_2(g) + e^- \rightarrow NO_2^-(ads)$$

Conclusion

In summary, we developed a synthesis method for the facile preparation of a ZnO/$Ti_3C_2T_x$ composite with a lamellar structure for gas sensing. The enhanced sensitivity and stability of the NO_2 sensors are attributed to an increased electron density transfer between NO_2 molecules and the sensing layers. The underlying sensing mechanism responsible for the observed improvements in NO_2 sensing performance was systematically examined, providing valuable insights into the complex interactions between the composite materials and NO_2 molecules. This understanding of the sensing mechanism offers guidance for the design and optimization of future MXene-based gas sensors, promoting the development of highly efficient and reliable platforms for environmental monitoring and industrial applications.

Experimental

Synthesis of pure $Ti_3C_2T_x$ MXene and ZnO/$Ti_3C_2T_x$ nanocomposites

Typically, 0.4 g of LiF (Sigma) was dissolved in 5 mL of 9 M HCl (China chem, 36 wt %) aqueous solution under vigorous stirring for 30 min. Then, a certain amount of Ti_3AlC_2 MAX phase (100 mesh, purchased from Sigma) was slowly added into the mixture solution and kept at 50 °C in an oil bath. After one day, the reaction solution was filtered and washed using vacuum filtration and centrifuged at 3500 rpm with DI water until pH ≈ 7.0. Finally, the $Ti_3C_2T_x$ MXene was collected and freeze-dried for further fabrication.

The ZnO/$Ti_3C_2T_x$ heterojunction was prepared via a facile self-assembly process, as displayed in Figure 8. In brief, a certain amount of $Ti_3C_2T_x$ MXene (10, 20, and 30 mg) was well dispersed in 50 mL of deionized water by ultrasonication. Subsequently, 0.744 g of zinc nitrate hexahydrate ($Zn(NO_3)_2{\cdot}6H_2O$) was added to the $Ti_3C_2T_x$ MXene suspension under vigorous magnetic stirring for 30 min to ensure complete dissolution and homogeneous mixing. Then, 0.350 g of hexamethylenetetramine (HMTA, $C_6H_{12}N_4$) was added to the mixture solution under continuous stirring. The resulting suspension was maintained in an oil bath at 70 °C for 2 h. After completion of the reaction, the precipitate was collected and washed several times with DI water to remove residual reactants and by-products. Subsequently, the obtained product was aged at 100 °C under a nitrogen atmosphere to facilitate the formation of a stable ZnO/$Ti_3C_2T_x$ interface while minimizing the oxidation of $Ti_3C_2T_x$ during the post-synthesis process. The composites prepared with 10, 20, and 30 mg of $Ti_3C_2T_x$ MXene were designated as ZM1, ZM2, and ZM3, respectively. For comparison, pure ZnO nanostructures were synthesized following the same procedure without the addition of $Ti_3C_2T_x$ MXene.

Materials characterization

The morphology and elemental analysis of the selected samples were recorded by scanning electron microscopy (SEM, JEOL, IT200 Japan). The phase structure of samples was obtained by an X-ray diffractometer (XRD, D8 Advance Eco, Bruker AXS Germany) with 2θ ranging from 5° to 70° and Cu Kα irradiation (λ = 0.154056 nm). The porous structure was analyzed by nitrogen adsorption/desorption isothermals using the

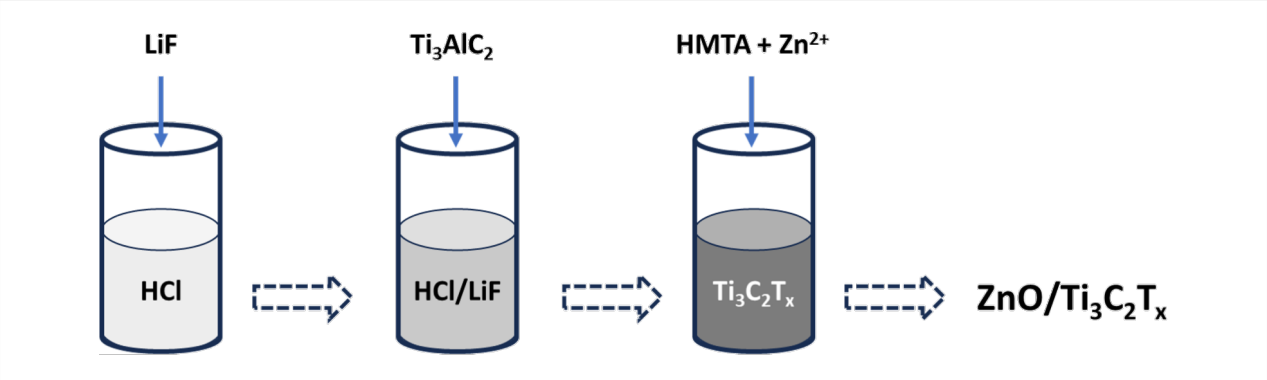


Figure 8: Schematic illustration of the synthesis of ZnO/$Ti_3C_2T_x$ composites.

Brunner–Emmett–Teller method (BET, TriStar II Plus 3030, Micromeritics USA).

Gas sensing measurements

The gas sensors were composed of a glass substrate and a thin layer of as-synthesized composites. In brief, the precise amounts of prepared samples were first dispersed in ethanol and well-sonicated for 15 min. Then, 5 µL dispersion was drop-cast onto the cleaned glass substrate. Finally, the sensors underwent aging in a vacuum furnace to remove ethanol and improve the bonding between the substrate and gas sensing material.

For gas sensing measurements, the substrate was located in a stainless steel chamber. The signal was analyzed using a source meter instrument (Keithley 2400). The gas flow rate was set to 500 sccm and adjusted by mass flow controllers. The ratio of synthetic air to target gas was changed to obtain the desired gas concentration. Moreover, the sensor response is defined as $S = (R_g/R_a - 1) \times 100\%$, where R_a is the resistance under synthetic air after stabilization, and R_g is the resistance under target gas. The response/recovery time is calculated as the time taken for composites to achieve 90% of the maximum resistance change.

Funding

This work was funded by the Vietnam Academy of Science and Technology (VAST) under Grant Number THTEXS.02/24-26.

Competing Interest

The authors declare that they have no competing financial interests or personal relationships that could have influenced the work reported in this study.

Author Contributions

Ngo Thi Chau: conceptualization; data curation; formal analysis. Quoc Vinh Ho: investigation; methodology. Dai Hai Nguyen: project administration; resources; software. Phan Khanh Thinh Nguyen: validation; visualization; writing – original draft. Qui Thanh Hoai Ta: supervision; validation; visualization; writing – original draft; writing – review & editing.

ORCID® iDs

Quoc Vinh Ho - https://orcid.org/0009-0005-3057-2303
Dai Hai Nguyen - https://orcid.org/0000-0003-3501-7390
Phan Khanh Thinh Nguyen - https://orcid.org/0000-0002-8204-6701
Qui Thanh Hoai Ta - https://orcid.org/0000-0002-0387-6281

Data Availability Statement

Data generated and analyzed during this study is available from the corresponding author upon reasonable request.

References

1. Yang, H.; Feng, Q.; Xu, W.; Tang, Y.; Bai, G.; Liu, Y.; Liu, Z.; Xia, S.; Wu, Z.; Zhang, Y. *Eco-Environ. Health* **2024,** *3,* 208–226. doi:10.1016/j.eehl.2024.01.001
2. Walker, J. M.; Akbar, S. A.; Morris, P. A. *Sens. Actuators, B* **2019,** *286,* 624–640. doi:10.1016/j.snb.2019.01.049
3. Benson, C.; Obasi, I. C.; Akinwande, D. V.; Ile, C. *Heliyon* **2024,** *10,* e23604. doi:10.1016/j.heliyon.2023.e23604
4. Kwiatkowski, S.; Polat, M.; Yu, W.; Johnson, M. S. Industrial Emissions Control Technologies: Introduction. In *Air Pollution Sources, Statistics and Health Effects;* Goodsite, M. E.; Johnson, M. S.; Hertel, O., Eds.; Encyclopedia of Sustainability Science and Technology Series; Springer US: New York, NY, 2021; pp 477–511. doi:10.1007/978-1-0716-0596-7_1083
5. Patel, A. K.; Chaudhary, H. H.; Patel, K. S.; Sen, D. J. *World J. Pharm. Sci.* **2014,** *2,* 729–744.
6. Saxena, P.; Sonwani, S. *Criteria Air Pollutants and Their Impact on Environmental Health;* Springer: Singapore, 2019. doi:10.1007/978-981-13-9992-3
7. Niza, I. L.; de Souza, M. P.; da Luz, I. M.; Broday, E. E. *Indoor Built Environ.* **2024,** *33,* 218–236. doi:10.1177/1420326x231191079
8. Norbäck, D.; Hashim, J. H.; Hashim, Z.; Ali, F. *Sci. Total Environ.* **2017,** *592,* 153–160. doi:10.1016/j.scitotenv.2017.02.215
9. Zhang, S.; Zhao, L.; Huang, B.; Li, X. *Sens. Actuators, B* **2020,** *319,* 128264. doi:10.1016/j.snb.2020.128264
10. Lascola, K. M.; Wilkins, P. A.; Wong, D.; Dunkel, B.; Sponseller, B.; Fintl, C.; Bedenice, D. Respiratory Disorders. In *Equine Neonatal Medicine;* Wong, D. M.; Wilkins, P. A., Eds.; John Wiley & Sons, Inc.: Hoboken, U.S.A., 2024; pp 153–223. doi:10.1002/9781119617228.ch8
11. Manisalidis, I.; Stavropoulou, E.; Stavropoulos, A.; Bezirtzoglou, E. *Front. Public Health* **2020,** *8,* 14. doi:10.3389/fpubh.2020.00014
12. Yadav, S.; Kumar, B.; Kaushik, S. *Appl. Surf. Sci. Adv.* **2023,** *18,* 100512. doi:10.1016/j.apsadv.2023.100512
13. Rehman, A.; Park, S.-J. J. *J. Ind. Eng. Chem. (Amsterdam, Neth.)* **2020,** *89,* 28–46. doi:10.1016/j.jiec.2020.06.009
14. Zhang, H.; Chhowalla, M.; Liu, Z. *Chem. Soc. Rev.* **2018,** *47,* 3015–3017. doi:10.1039/c8cs90048e
15. Sai Bhargava Reddy, M.; Aich, S. *Coord. Chem. Rev.* **2024,** *500,* 215542. doi:10.1016/j.ccr.2023.215542
16. Gogotsi, Y. *MXenes: From Discovery to Applications of Two-Dimensional Metal Carbides and Nitrides;* Jenny Stanford Publishing, 2023. doi:10.1201/9781003306511
17. Alhabeb, M.; Maleski, K.; Anasori, B.; Lelyukh, P.; Clark, L.; Sin, S.; Gogotsi, Y. *Chem. Mater.* **2017,** *29,* 7633–7644. doi:10.1021/acs.chemmater.7b02847
18. Atkare, S.; Rout, C. S.; Jagtap, S. *Mater. Adv.* **2024,** *5,* 1440–1453. doi:10.1039/d3ma00890h
19. Mashangva, T. T.; Goel, A.; Bagri, U.; Prasher, S.; Sharma, A.; Kumar, M.; Singh, P. K. *Appl. Mater. Today* **2024,** *38,* 102163. doi:10.1016/j.apmt.2024.102163
20. Bhardwaj, R.; Hazra, A. *J. Mater. Chem. C* **2021,** *9,* 15735–15754. doi:10.1039/d1tc04085e
21. Fard, N. E.; Raeisi, I.; Yousefipour, Z.; Mosavin, R. *ACS Appl. Nano Mater.* **2024,** *7,* 5698–5728. doi:10.1021/acsanm.3c05455
22. Choi, J.; Kim, Y.; Cho, S.; Park, K.; Kang, H.; Kim, S. J.; Jung, H. *Adv. Funct. Mater.* **2020,** *30,* 2003998. doi:10.1002/adfm.202003998

23. Ta, Q. T. H.; Tran, N. M.; Tri, N. N.; Sreedhar, A.; Noh, J.-S. *Chem. Eng. J.* **2021,** *425,* 131437. doi:10.1016/j.cej.2021.131437
24. Sun, B.; Lv, H.; Liu, Z.; Wang, J.; Bai, X.; Zhang, Y.; Chen, J.; Kan, K.; Shi, K. *J. Mater. Chem. A* **2021,** *9,* 6335–6344. doi:10.1039/d0ta11392a
25. Hamada, A. M.; Radi, A. A.; Al-Kahtany, F. A.; Farghaly, F. A. *J. Plant Nutr.* **2024,** *47,* 656–679. doi:10.1080/01904167.2023.2280127
26. Bhapkar, A. R.; Bhame, S. *J. Environ. Chem. Eng.* **2024,** *12,* 112553. doi:10.1016/j.jece.2024.112553
27. Moon, D.-B.; Bag, A.; Lee, H.-B.; Meeseepong, M.; Lee, D.-H.; Lee, N.-E. *Sens. Actuators, B* **2021,** *345,* 130373. doi:10.1016/j.snb.2021.130373
28. Song, Y.; Chen, F.; Zhang, Y.; Zhang, S.; Liu, F.; Sun, P.; Yan, X.; Lu, G. *Sens. Actuators, B* **2019,** *287,* 191–198. doi:10.1016/j.snb.2019.01.146
29. Li, S.; Yu, L.; Zhang, Y.; Zhang, C.; Cao, L.; Nan, N.; Fan, X.; Wang, H. *Sens. Actuators, B* **2024,** *413,* 135890. doi:10.1016/j.snb.2024.135890
30. Yao, L.; Tian, X.; Cui, X.; Zhao, R.; Chen, T.; Xiao, X.; Wang, Y. *Appl. Phys. Rev.* **2023,** *10,* 031414. doi:10.1063/5.0138182
31. Liu, T.; Jia, X.; Qiao, L.; Yang, J.; Wang, S.; Li, Y.; Shao, D.; Feng, L.; Song, H. *Sens. Actuators, B* **2023,** *390,* 133908. doi:10.1016/j.snb.2023.133908
32. Le, T. K. O.; Mapari, M. G.; Kim, T. *ACS Omega* **2024,** *9,* 40790–40800. doi:10.1021/acsomega.4c05574
33. Ieamviteevanich, P.; Kim-Lohsoontorn, P.; Seeharaj, P. *Res. Chem. Intermed.* **2025,** *51,* 1863–1881. doi:10.1007/s11164-025-05516-5
34. Nguyen Van, C. H.; Nguyen, H. K.; Huynh, H. Q.; Pham, H. A.; Dinh, T. M.; Luong, H. N.; Phan, B. T.; Tran, C. K.; Dang, V. Q. *Adv. Nat. Sci.: Nanosci. Nanotechnol.* **2020,** *11,* 015002. doi:10.1088/2043-6254/ab6290
35. Singhal, I.; Balaji, B. S. *IOP Conf. Ser.: Mater. Sci. Eng.* **2021,** *1059,* 012060. doi:10.1088/1757-899x/1059/1/012060
36. Sarycheva, A.; Gogotsi, Y. *Chem. Mater.* **2020,** *32,* 3480–3488. doi:10.1021/acs.chemmater.0c00359
37. Pei, J.; Wan, X.; Guo, M.; Mi, J.; Wu, W.; Hong, Y.; Hu, P.; Chen, P.; Chen, L.; Xiang, S.; Zhang, Q.; Zeng, H.; Liu, L.; Fan, X.; Yu, B. *Chem. Eng. J.* **2025,** *523,* 168624. doi:10.1016/j.cej.2025.168624
38. Liu, Y.; Dang, A.; Liu, X.; Wang, X.; Zada, A.; Chen, J.; Fan, X.; Zhao, T.; Li, J.; Li, T. *Sens. Actuators, B* **2025,** *422,* 136685. doi:10.1016/j.snb.2024.136685
39. Parker, T.; Zhang, Y.; Shevchuk, K.; Zhang, T.; Khokhar, V.; Kim, Y.-H.; Kadagishvili, G.; Bugallo, D.; Tanwar, M.; Davis, B.; Kim, J.; Fakhraai, Z.; Hu, Y.-J.; Jiang, D.-e.; Talapin, D. V.; Gogotsi, Y. *ACS Nano* **2025,** *19,* 22228–22239. doi:10.1021/acsnano.5c03810
40. Xie, Y.; Sun, F.; Yang, Y.; Li, X.; Wang, H.; Sang, L.; Zhao, W.; Wang, T.; Jia, F.; Zhou, T.; Yin, G.; Wang, X. *Chem. Eng. J.* **2025,** *519,* 165339. doi:10.1016/j.cej.2025.165339
41. Nhiem, L. T.; Mao, J.; Hoai Ta, Q. T.; Seo, S. *Nanoscale Adv.* **2025,** *7,* 1452–1463. doi:10.1039/d4na00927d
42. Hu, X.; Zhang, K.; Li, R.; Cao, Y.; Tian, D.; Zhu, Z. *Chem. Eng. J.* **2025,** *519,* 165401. doi:10.1016/j.cej.2025.165401
43. Cai, Z.; Hou, J.; Kim, J.-H.; Li, G.; Lee, C. H.; Kim, H.; Hilal, M. *Ceram. Int.* **2025,** *51,* 40637–40647. doi:10.1016/j.ceramint.2025.06.302
44. Seekaew, Y.; Traiwatcharanon, P.; Kamlue, T.; Wongchoosuk, C. *Mater. Sci. Semicond. Process.* **2025,** *199,* 109821. doi:10.1016/j.mssp.2025.109821
45. Chen, L.; Chen, X.; Wang, F.; Tong, Y.; Zhang, K.; Han, Z.; Zhang, M. *Sens. Actuators, B* **2026,** *447,* 138802. doi:10.1016/j.snb.2025.138802
46. Hou, M.; Jiang, G.; Guo, S.; Gao, J.; Shen, Z.; Wang, Z.; Ye, X.; Yang, L.; Du, Q.; Yi, J.; Zeng, H.; Briois, P. *Arabian J. Chem.* **2023,** *16,* 104808. doi:10.1016/j.arabjc.2023.104808
47. Guo, F.; Feng, C.; Zhang, Z.; Zhang, L.; Xu, C.; Zhang, C.; Lin, S.; Wu, H.; Zhang, B.; Tabusi, A.; Huang, Y. *Sens. Actuators, B* **2023,** *375,* 132885. doi:10.1016/j.snb.2022.132885
48. Zhou, M.; Hu, X.; Liu, Z.; Qin, W.; Tan, L.; Yang, J.; Yu, D.; Mu, Q.; Bao, A.; Bi, Y.; Yu, W.; Zhang, W. *Chem. Eng. J.* **2025,** *522,* 167089. doi:10.1016/j.cej.2025.167089
49. Yao, Y.; Wang, Z.; Han, Y.; Xie, L.; Zhao, X.; Shahrokhian, S.; Barsan, N.; Zhu, Z. *Sens. Actuators, B* **2023,** *381,* 133412. doi:10.1016/j.snb.2023.133412
50. Fan, C.; Yang, J.; Ni, W.; Wu, J.; Liu, X.; Li, Z.; Zhang, Y.; Quan, W.; Zeng, M.; Hu, N.; Fang, H.; Wang, T.; Yang, Z. *ACS Sens.* **2024,** *9,* 4870–4878. doi:10.1021/acssensors.4c01394
51. Liu, M.; Wang, J.; Song, P.; Ji, J.; Wang, Q. *Sens. Actuators, B* **2022,** *361,* 131755. doi:10.1016/j.snb.2022.131755
52. Zhang, J.; Li, P.; Zhu, Z.; Sun, X.; Wang, Z.; Sun, F.; Zhou, H. *Ceram. Int.* **2025,** *51,* 49349–49358. doi:10.1016/j.ceramint.2025.08.176
53. Tang, L.; Zhou, K.; Su, H.; Tang, J.; Wu, Q.; Luo, L.; Guo, X.; Zeng, D. *ACS Appl. Nano Mater.* **2025,** *8,* 4636–4648. doi:10.1021/acsanm.4c07128
54. Shin, K. Y.; Mirzaei, A.; Oum, W.; Kim, E. B.; Kim, H. M.; Moon, S.; Kim, S. S.; Kim, H. W. *Sens. Actuators, B* **2024,** *409,* 135605. doi:10.1016/j.snb.2024.135605
55. Xu, X.; Ma, W.; Jiang, H.; Wang, X.; Liu, W.; Wang, M.; Sun, G.; Ma, N.; Ma, S.; Wang, J.; Chang, G. *Sens. Actuators, B* **2025,** *422,* 136595. doi:10.1016/j.snb.2024.136595
56. Li, D.; Zhang, Z.; Jiao, M.; Dong, Y.; Yu, S.; Li, C.; He, H.; Jiang, J.; Liu, K.; Li, Z. *Small* **2025,** *21,* 2409716. doi:10.1002/smll.202409716
57. Sun, S.; Wang, M.; Chang, X.; Jiang, Y.; Zhang, D.; Wang, D.; Zhang, Y.; Lei, Y. *Sens. Actuators, B* **2020,** *304,* 127274. doi:10.1016/j.snb.2019.127274

License and Terms

This is an open access article licensed under the terms of the Beilstein-Institut Open Access License Agreement (https://www.beilstein-journals.org/bjnano/terms), which is identical to the Creative Commons Attribution 4.0 International License (https://creativecommons.org/licenses/by/4.0). The reuse of material under this license requires that the author(s), source and license are credited. Third-party material in this article could be subject to other licenses (typically indicated in the credit line), and in this case, users are required to obtain permission from the license holder to reuse the material.

The definitive version of this article is the electronic one which can be found at:
https://doi.org/10.3762/bjnano.17.79

BEILSTEIN JOURNAL OF NANOTECHNOLOGY

Gold bipyramids as a promising alternative to gold nanorods for analytical and biomedical applications

Andrey M. Burov[1], Sergey V. Zarkov[1,2], Arina V. Drozd[1], Igor V. Borisov[1], Elena G. Zavyalova[3] and Nikolai G. Khlebtsov[*1,4,§]

Full Research Paper

Open Access

Address:
[1]Institute of Biochemistry and Physiology of Plants and Microorganisms, "Saratov Scientific Centre of the Russian Academy of Sciences", 13 Entuziastov Pr., Saratov 410049, Russia, [2]Institute of Precision Mechanics and Control, "Saratov Scientific Centre of the Russian Academy of Sciences", 24 Rabochaya Str., Saratov 410028, Russia, [3]Lomonosov Moscow State University, Faculty of Chemistry, Leninskie Gory 1-3, Moscow 119991, Russia and [4]Saratov State University, 83 Astrakhanskaya Str., Saratov 410012, Russia

Email:
Nikolai G. Khlebtsov[*] - khlebtsov@ibppm.ru

* Corresponding author
§ Cell phone: +7 (905)3256536

Keywords:
bacteria; gold nanoparticles; nanobipyramids and nanorods; photothermal therapy; plasmon resonance; plasmonics; SERS; surface-enhanced Raman scattering

Beilstein J. Nanotechnol. **2026,** *17,* 1170–1184.
https://doi.org/10.3762/bjnano.17.80

Received: 19 May 2026
Accepted: 07 August 2026
Published: 25 August 2026

This article is part of the thematic issue "Innovative nanomaterials for next-generation bio- and chemosensing".

Guest Editor: T.-D. Nguyen

© 2026 Burov et al.; licensee Beilstein-Institut.
License and terms: see end of document.

Abstract

Gold nanobipyramids and nanorods of comparable dimensions were synthesized to evaluate and contrast their plasmonic, analytical, and photothermal performance. The bipyramids exhibited a markedly higher absorption spectral quality factor than the nanorods. For surface-enhanced Raman scattering comparison, both nanoparticle types were functionalized with thiolated nitrobenzene molecules, revealing an approximately fourfold higher enhancement factor for the bipyramids. Their analytical sensitivity was further assessed by monitoring the plasmon resonance wavelength shift in response to changes in the external refractive index, as well as variations in the thickness and refractive index of a nanoscale coating. In all cases, the bipyramids outperformed the nanorods. Additionally, both experimental and theoretical analyses confirmed the superior efficiency of bipyramids as photothermal agents for converting laser irradiation into heat. Effective photothermal inactivation of *Escherichia coli* was achieved under resonant laser excitation using either particle type. Given the recent advances in their synthesis, gold bipyramids emerge as highly promising alternatives to nanorods for a broad range of analytical and biomedical applications.

Introduction

Anisotropic metal nanoparticles [1-5] are actively researched and utilized due to their flexible tunability of the plasmon resonance (PR) across a broad UV–vis–NIR range [6], significantly larger scattering and absorption cross sections [7], and enhanced local field effects [8] compared to plasmonic nanospheres. Modern methods of colloidal chemical synthesis [9]

enable the production of a wide variety of anisotropic nanoparticles, including gold–silver nanocages [10], silver nanocubes [11], gold nanostars [12], triangular nanoprisms [13], flat particles [14], gold–silver nanorods [15], as well as particles with field enhancement in gaps (gap-enhanced Raman tags) [16]. However, the most well-known and widely used are conventional gold nanorods [17] with approximately hemispherical ends and a cylindrical or pentagonal cross section. To date, the synthesis and application protocols for gold nanorods are well established [18-21], which explains the consistently high annual number of publications on these nanoparticles (according to SCOPUS, over 180 articles in 2025 alone have titles containing the phrase "gold nanorods").

Compared to nanorods, pentagonal gold nanobipyramids (BPs) are far less studied [22], despite having similar plasmon resonance tunability [23] (with an aspect ratio change from 2 to 6, the plasmon resonance wavelength shifts from approximately 600 to 1100 nm) and thermoplasmonic properties [24-26]. Regarding the differences, BPs possess five uniformly distributed twinning planes at the vertices and sharp tips [27], whereas nanorods are single crystals with roughly hemispherical ends. These morphological differences result in distinct local plasmonic properties, higher resonance sensitivity to the dielectric environment [28-30], and higher quality factors of the plasmonic absorption and scattering peaks in BPs. Despite these apparent advantages, BPs remain, in our opinion, undeservedly less popular due to their non-trivial synthesis [23,31-35] and functionalization [36]. Furthermore, simulating the optical properties of BPs (especially when coated with functional molecules) requires numerical methods [37,38] as until very recently there were no simple and sufficiently accurate analytical models for plasmonic nanoparticles with a dielectric coating [39].

In this work, we investigate how differences in the morphology of gold nanorods and bipyramids lead to vast differences in local field distribution and, through these differences, to multimodal enhancements in extinction quality spectra, surface-enhanced Raman scattering (SERS), sensing, and photothermal response. Specifically, we present a comparative theoretical and experimental study of UV–vis extinction spectra, SERS, refractive index sensitivity, thermoplasmonic properties of gold BPs and nanorods with similar PR wavelengths, and plasmonic photothermal killing of bacteria in water suspensions. In contrast to published similar studies (see, e.g., [40,41]), we compared the normalized quantities that are proportional to the SERS intensity per adsorbed molecule. For comparison of thermoplasmonic experiments, we introduced the normalized absorption efficiency, which is proportional to the absorbed power per unit volume at a constant mass/volume concentration of particles. Finally, our analysis of analytical sensitivity includes two different options, that is, (1) the usual sensitivity to the refractive index of the surrounding medium and (2) an original analysis of the analytical response to an adsorbed layer of analytes with different nanometer-scale thicknesses.

Using the chemical etching method [42], we synthesized a set of nanorod samples with PR ranging from 600 to 950 nm, including a sample with a PR close to that of the BP sample. To calculate the plasmonic properties of the nanoparticles, we used a previously described 2.5D finite element method [43,44] implemented in the commercial software package COMSOL Multiphysics 5.1 (Wave Optics module), applicable to axially symmetric particles. Also, we used our recently developed analytical method [39].

We demonstrate that BP properties, including the quality factor of extinction spectra, SERS signal enhancement, the analytical sensitivity of the PR wavelength to the local dielectric environment, and the efficiency of light-to-heat conversion, surpass those of gold nanorods with comparable dimensions and PR wavelengths. Experiments also demonstrate effective photothermal killing of *Escherichia coli* DH5α bacteria under laser irradiation at a wavelength near the PR.

Methods

Theoretical methods

In the 2.5D formalism [43,44], the incident and scattered fields are expanded in cylindrical harmonics, and the response of each harmonic is computed separately, leading to significant savings in computational resources in terms of memory and processing time [45]. Compared to conventional 3D modeling, the 2.5D formalism substantially reduces the computational time per spectral data point and enables averaging cross-sectional spectra over random particle orientations with acceptable computational costs. The dielectric function of gold was calculated using a spline interpolation [46] of the data from [47]. In all calculations presented hereafter, the correction of the bulk dielectric function for the finite particle size was performed using the volume-equivalent sphere radius as the effective electron surface scattering length and the scattering constant $A_s = 0.33$ [48,49]. The refractive index of the shell, $n_2 = \sqrt{\varepsilon_2} = 1.5$, was chosen to be close to that of many biopolymers and typical stabilizers, such as cetyltrimethylammonium bromide (CTAB) or cetyltrimethylammonium chloride (CTAC). In all calculations, the dielectric function of water [44] $\varepsilon_m(\lambda) = n_m^2(\lambda)$ was used as the external medium dielectric function. The thickness of the CTAB stabilizer shell was set to 3 nm based on the data from [50]. The employed analytical method MEM+DEM [39] is based on a combination of the modal expansion method (MEM) [51] and the dipole equivalence method (DEM) [52]. Hereafter,

for brevity, we will refer to the MEM+DEM method simply as MEM. The primary theoretical models considered were pentagonal bipyramids with tip rounding radii specified in [51] and cylindrical nanorods with hemispherical ends. We also employed an inscribed bicone as a bipyramid model, following the approach in [38].

Experimental methods

The following reagents were used in this study: hydrogen tetrachloroaurate(III) trihydrate ($HAuCl_4{\cdot}3H_2O$), cetyltrimethylammonium bromide (CTAB, 98%), cetyltrimethylammonium chloride (CTAC, 25% solution in water), sodium borohydride ($NaBH_4$, 99%), silver nitrate ($AgNO_3$, 99%), hydrochloric acid (concentrated HCl), L-ascorbic acid (AA, 99.9%), citric acid (CA, 99%), 4-nitrothiophenol (NBT, 97%), and hydroquinone (HQ, 99%). Ultrapure deionized water obtained using a Milli-Q Integral 5 system was used in all experimental syntheses.

Extinction spectra were measured using a Specord 300 spectrophotometer (Analytik Jena, Germany). The Raman spectra of composite labels were recorded using a combined setup comprising a Leica MD 2500 microscope, a SeekerPro785 spectrometer from Ocean Optics (USA), and a 785 nm laser operating at 30 mW. The surface potentials (charges) of the nanoparticles were measured using a Zetasizer NanoSeries NT dynamic light scattering spectrometer (Malvern Instruments, UK). Nanoparticle images were obtained with a Libra-120 transmission electron microscope (TEM) (Carl Zeiss, Jena, Germany) at the "Symbiosis" Center for the Collective Use of Research Equipment (IBPPM RAS). A diode laser with a wavelength of 795–810 nm, fiber optic output, and a maximum continuous output power of 2 W (Opto Power Corp., USA) was used to heat nanoparticle suspensions. The temperature in the cuvette was measured using a Guide PC210 thermal imager (China).

Gold nanobipyramids were obtained by overgrowth of polycrystalline seeds in a CTAB medium [32]. In the first, preliminary stage, gold thermal seeds were synthesized. For this, 10 mL of 0.25 mM $HAuCl_4{\cdot}3H_2O$ were reduced with 0.25 mL of 25 mM sodium borohydride under vigorous stirring in a 20 mL flask, in an aqueous solution containing 50 mM CTAC and 5 mM citric acid. The reaction mixture changed color from yellow to brown. After 2 min, the solution was transferred to a silicone bath at 80 °C and stirred for 90 min. During the reaction, the solution turned deep red. In the second stage, the obtained seeds, cooled to room temperature, were added under vigorous stirring to a solution containing 50 mL of 100 mM CTAB, 2.5 mL of 10 mM $HAuCl_4{\cdot}3H_2O$, 500 µL of 10 mM silver nitrate, 1 mL of 1 M hydrochloric acid, and 400 µL of 100 mM ascorbic acid. The mixture was kept at 30 °C for about 2 h. The resulting bipyramids were centrifuged several times (10,000 rpm) and redissolved in 1 mM CTAC. The synthesis yielded gold bipyramids with an average longitudinal size of 75 ± 3 nm, a transverse size of 25 ± 2 nm, and a plasmon resonance maximum around 753 nm.

Gold nanorods were obtained using a modified protocol [53] that enabled the synthesis of thin, long rods. Gold seeds were prepared by adding an aqueous sodium borohydride solution (10 mM, 0.6 mL) to an aqueous solution containing CTAB (0.1 M, 10 mL) and $HAuCl_4$ (10 mM, 0.25 mL). Silver nitrate (3.5 mL, 0.1 M) was added to a solution of $HAuCl_4$ (500 mL, 0.5 mM) in 0.1 M CTAB, followed by the addition of an aqueous hydroquinone solution (25 mL, 0.1 M). Note that silver nitrate plays multiple, intertwined roles in the seed-mediated synthesis of single-crystalline gold nanorods [54,55]. Its functions span three critical areas, namely, (1) symmetry breaking and nucleation kinetics, (2) anisotropic growth directionality and aspect ratio control, and (3) shape and facet regulation via surface passivation.

The resulting mixture was stirred manually until it became clear. Then, 8 mL of the seeds were added, and the mixture was stirred and left overnight at 30 °C without stirring. A significant drawback of the protocol [53] is the high impurity particle content (10–15%). In this work, we used a modified version [56] with a purification step: the colloid was centrifuged at 10,000 rpm for 20 min, and the pellet was redissolved in 30 mL of 200 mM CTAC and left undisturbed for 1 h. The nanorods aggregated at the bottom and the walls of the tube, forming a brown film. The supernatant, containing particles of other shapes, was removed. The nanorods were redissolved in 50 mM CTAB to a concentration corresponding to an optical density of 2 at the longitudinal resonance at 945 nm, measured in a 2 mm path length cuvette. To completely remove impurity particles, the purification procedure was repeated twice. TEM analysis of the samples revealed the presence of thin nanorods with an average thickness of about 20 nm and a length of about 95 nm. A distinctive feature of our protocol is the practically zero percentage of non-target particles (0.5%) and the high quality of the extinction spectrum, as measured by the extinction ratio at the longitudinal and transverse PR wavelengths (>6).

To obtain AuNR samples with different longitudinal plasmon resonance (LPR) wavelengths, 50 mL of AuNR colloid in 50 mM CTAB was titrated with a 2 mM $HAuCl_4$ solution (adding 20 µL aliquots every 10 min). Before each addition, the extinction spectrum was measured, and if the desired LPR wavelength was reached, the required amount of sample (typically 3 mL) was taken from the colloid.

For the functionalization of gold nanorods and bipyramids with 4-nitrothiophenol (NBT) molecules, 10 µL of a 2 mM ethanolic NBT solution was added to 1.5 mL of the colloid. The mixture was incubated for 30 min. The nanoparticles were then centrifuged at 10,000 rpm for 5 min and resuspended in 2 mL of 10 mM CTAC.

For photothermal experiments, a 24-hour bacterial culture of *Escherichia coli* DH5α (from the collection of IBFPM RAS) with an optical density A_6 = 1 in a 1 cm cuvette and gold nanorod and nanobipyramid suspensions with an optical density of A_{80} = 5 were used. A 0.01 M PBS buffer with pH 7.5 was used as the dilution medium. For the Alamar Blue assay [57], a resazurin solution at 0.55 mg·mL^{-1} was used. Fluorescence spectra were recorded on a Cary Eclipse spectrofluorimeter (Agilent) over 590–610 nm, with a slit width of 5 nm and an excitation wavelength of 530 nm.

Results and Discussion

1 Extinction spectra and geometrical parameters of nanoparticles

In Figure 1A, solid lines represent the extinction spectra of four nanorod samples with LSPR at 945, 844, 735, and 644 nm (curves 1–4), as well as the spectrum of gold bipyramids (5); the inset shows a TEM image of the bipyramids. Additional and statistical data can be found in Supporting Information File 1 (Figures S1–S5). Dashed lines show the spectra of the same samples after functionalization with the Raman reporter molecule NBT. Figure 1B–E shows TEM images of the initial 944 nm nanorods and of samples obtained through chemical length etching with virtually no change in thickness. The geometric parameters of the particles, based on statistical analysis of TEM images, are given below in Table 1.

As shown in Table 1, during the etching process, the length of the nanorods decreases from 95 to 45 nm, and the aspect ratio decreases on average from approximately 4.85 to 2.4, while the nanorod diameter remains practically constant at 19 ± 0.8 nm. Accordingly, the plasmon resonance wavelength shifts from the infrared (945 nm) to the visible (640 nm) region. The spectra in Figure 1 were measured at approximately equal molar concentrations of gold (0.1 mM), as determined using the method described in [58].

In Table 1, the theoretical AR_P values were calculated by the linear equation

$$\lambda_{PR}\,(\mathrm{nm}) = 111 \times \mathrm{AR} + 393, \qquad (1)$$

which was obtained as the average of T-matrix simulations for bare AuNRs and COMSOL simulations [39] for AuNRs

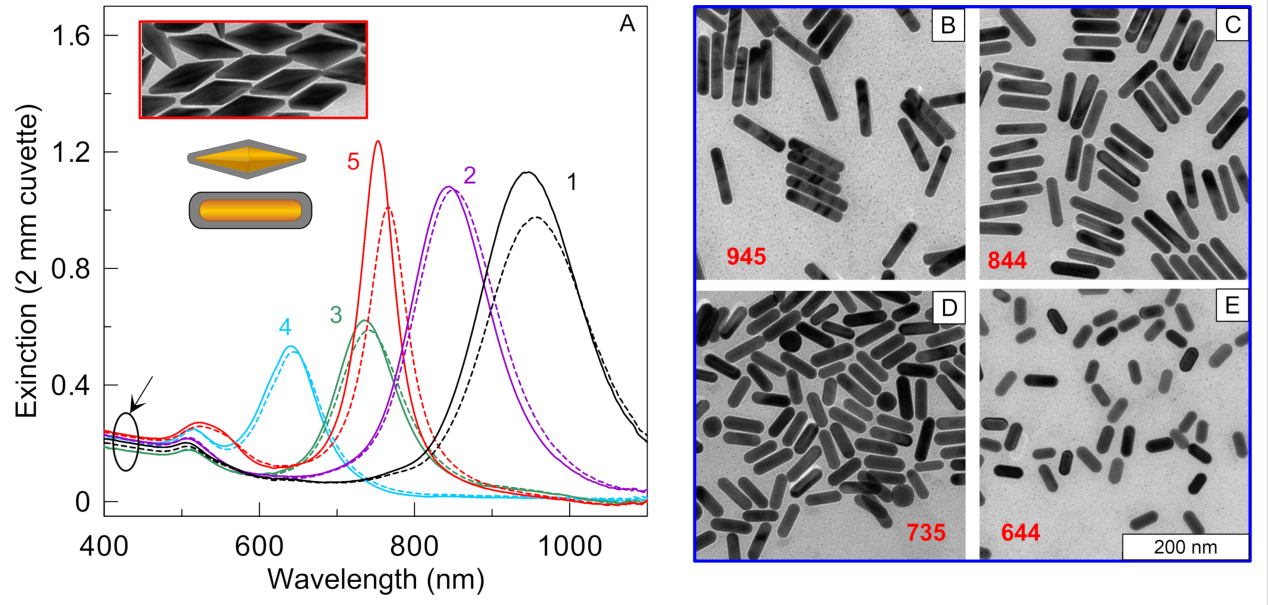


Figure 1: Extinction spectra (measured in a 2 mm cuvette, panel A) and TEM images (panels B–E) of gold nanorods with plasmon resonances at 945 (1), 844 (2), 735 (3), and 644 (4) nm, and of gold bipyramids (inset in panel A) with a plasmon resonance at 753 nm (5). The arrow indicates the approximate equal extinction of all samples at 400 nm, corresponding to equal molar (or mass/volume) concentrations of gold. The inset shows a TEM image of the bipyramids. The dashed curves show the extinction spectra of the composite particles after functionalization with NBT molecules (AuNR@NBT, AuBP@NBT). Panel E shows a 200 nm scale bar applicable to all images.

Table 1: Geometric and optical parameters of the synthesized nanoparticles (length, diameter, aspect ratio, surface area to volume ratio (S/V)), the normalized plasmon resonance bandwidth (FWHM/λ_P), shift of the plasmon resonance after functionalization with NBT molecules (PR shift), measured SERS signal intensity (I_{1347}), and the value proportional to the intensity per molecule ($I_{1347}/(S/V)$). The ratio of the absorption efficiency factor to the radius of the equivalent volume sphere (Q_{abs}/R_{ev}) determines the photothermal efficiency of the particles at the plasmon resonance wavelength. The average length and aspect ratio were determined from TEM data (top numbers) and from the plasmon resonance wavelength, assuming a constant average diameter of 19 nm (bottom numbers). The aspect ratios in parentheses are calculated according to [59].

Sample	L_{TEM} L_{PR} (nm)[a]	d_{TEM} (nm)[a]	AR_{TEM} AR_{PR} (a.u.)[a]	S/V (nm^{-1})	FWHM/λ_{PR} (a.u.)[b]	PR shift (nm)[b]	I_{1347} (a.u.)[b]	$I_{1347}/(S/V) \times 10^{-3}$ (a.u.)[b]	Q_{abs}/R_{ev} (nm^{-1})
NR-644	44 ± 5.8 44 ± 4.0	19.0 ± 1.2	2.30 ± 0.16 2.26 ± 0.20 (2.14)	0.246	0.14 ± 0.01	3 ± 0.5	415 ± 72	1.7 ± 0.30	0.337
NR-735	62.2 ± 6.1 60 ± 4.9	19.0 ± 1.4	3.27 ± 0.09 3.14 ± 0.13 (3.08)	0.234	0.13 ± 0.01	4 ± 0.5	570 ± 108	2.4 ± 0.45	0.547
NR-844	82.3 ± 7.0 78 ± 5.2	18.9 ± 1.4	4.35 ± 0.07 4.10 ± 0.2 (4.21)	0.229	0.14 ± 0.01	6 ± 0.7	526 ± 85	2.3 ± 0.37	0.683
NR-945	90.2 ± 8.7 94 ± 6.1	18.7 ± 1.4	4.85 ± 0.13 4.97 ± 0.12 (5.25)	0.229	0.16 ± 0.02	7 ± 0.7	265 ± 59	1.2 ± 0.27	0.778
BP-753	75 ± 2.5	26.3 ± 1.2	2.85 ± 0.04	0.222	0.066 ± 0.008	13 ± 1.2	2150 ± 234	9.7 ± 0.90	0.996

[a]SD values from statistical analysis of 200 particles; [b]SD values from three independent measurements.

covered by a typical 3 nm CTAB layer [50]. The corresponding length L_P was obtained by multiplying AR_{PR} by the average rod diameter of 19 nm. There is a close agreement between the nanorods aspect ratios derived from TEM images and from PR wavelength through Equation 1. Recently, Engel et al. [59] reported a similar linear relation between the PR wavelength and the nanorods' aspect ratio $\lambda_{PR}(nm) = 97 \times AR + 436$. The corresponding AR values are indicated in parentheses of the fourth column. We note that Equation 1 agrees somewhat better with TEM data.

The average plasmon resonance bandwidth of the nanorods, expressed in terms of the standard parameter full width at half maximum (FWHM), remains approximately constant (around 0.14) for nanorods samples. When comparing with the extinction spectrum of bipyramids (curve 5 in Figure 1A), the remarkably high quality of their spectrum, with an FWHM parameter of 0.066, half that of all nanorods values, immediately stands out. This observation agrees with a small SD value for the aspect ratio length/width = 2.85 ± 0.04 derived from TEM measurements.

Further confirmation of the high quality of the bipyramids' extinction spectra comes from comparing experimental and theoretical extinction spectra (Figure 2). For randomly oriented gold nanorods, extinction spectra were calculated using the T-matrix method. For the bipyramids, the longitudinal excitation spectrum is presented, calculated using MEM (practically coinciding with the COMSOL results). From Figure 2, it follows that the experimental nanorod spectra are significantly

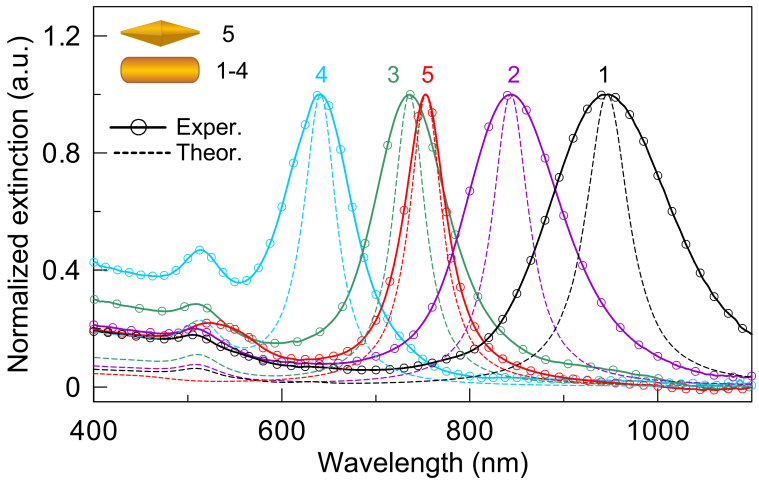


Figure 2: Experimental and theoretical (dashed lines) normalized extinction spectra for the five samples listed in Table 1. The theoretical particle aspect ratios AR_P were used as fitting parameters to match the calculated and measured plasmon resonance wavelength.

broader than the theoretical ones, as the latter do not account for particle size (aspect ratio) distribution. Quantitatively, this spectral broadening, expressed as the ratio of the experimental to the theoretical FWHM value, is 2.5 for the nanorods. In contrast, for the bipyramids, the same ratio is half of that, approximately 1.25, even though the theoretical model also did not account for particle size distribution.

After functionalization with the Raman reporter molecule NBT, the plasmon resonance maximum of all particles decreases in magnitude and shifts, as is typical, to the red region. It is clear that these changes are most pronounced in the bipyramids compared to the nanorods. Quantitatively, the plasmon resonance shift after functionalization for bipyramids is 2–4 times greater than that for nanorods. This is related to the higher analytical sensitivity of the bipyramids' plasmon resonance to the dielectric environment, which will be discussed below.

In addition to the usual geometric particle parameters L and AR, Table 1 also provides the average surface area-to-volume ratio (S/V). For nanorods with hemispherical ends, S/V = 12AR/[d(3AR – 1)], and for bipyramids modeled as inscribed bicones, $S/V = 6\sqrt{\mathrm{AR}^2+1}/(d\cdot\mathrm{AR})$. For rounded bicones, the numerical S/V value is slightly less than the analytical one. As shown in Table 1, this parameter varies within a narrow range of 0.222–0.246. In the next section, we will use this parameter to estimate the SERS signal intensity per NBT reporter molecule.

The last column of Table 1 presents the theoretical value of Q_{abs}/R_{ev}, which is the ratio of the absorption efficiency factor Q_{abs} to the radius of the equivalent volume sphere R_{ev}. This parameter determines the photothermal efficiency of plasmonic nanoparticles per unit volume at a constant concentration c (g·mL^{-1}), or, in other words, the photothermal efficiency per unit mass of nanoparticles. Indeed, the absorbed power per unit volume equals the product of the incident intensity I (W·cm^{-2}) and the numerical concentration N (cm^{-3}) multiplied by the absorption cross section $C_{abs}(cm^2) = \pi R_{ev}^2 Q_{abs}$:

$$P_{abs}\left(\mathrm{W/cm^3}\right) = I\times N\times C_{abs} = I\times\frac{c}{\frac{4}{3}\pi R_{ev}^3\rho}\times\pi R_{ev}^2 Q_{abs} = I\frac{3c}{4\rho}\times\frac{Q_{abs}}{R_{ev}}, \quad (2)$$

where ρ is the metal density. From Equation 2, it follows that the absorbed power per unit volume is proportional to the ratio Q_{abs}/R_{ev} at a constant mass/volume concentration of particles c (g·mL^{-1}).

2 Comparison of SERS spectra for nanorods and nanobipyramids

Figure 3 shows the SERS spectra of functionalized gold nanorods and bipyramids. The most intense line at 1347 cm^{-1} was used as a reference. Comparison of the spectra reveals a more intense peak for the functionalized bipyramids. Even for NR-735 nanorods, which are close to resonant excitation, the peak intensity is almost four times lower, even though the extinction peaks are comparable in magnitude and the mass/volume concentration of nanoparticles was the same.

To give some insight into the data of Figure 3B, we use a simple estimate based on experimental extinction spectra, SERS spectra, and particle geometric parameters from TEM data. As mentioned earlier, the extinction and SERS spectra were recorded at approximately the same molar concentration of 0.1 mM or, correspondingly, at a mass/volume concentration of gold 19.7 × 10^{-6} g·mL^{-1}. For numerical estimates, we will assume that the number of molecules per particle is proportional to their surface area. Since functionalization was carried out with an excess of NBT, this assumption implies monolayer adsorption of SERS-active molecules, and the number of molecules on a single particle is proportional to the ratio of the particle's surface area to the effective footprint area of one molecule $N_1 = S/S_1$. The total number of particles in 1 mL of colloid equals the ratio of the mass/volume concentration of gold to the mass of a single particle $N = m/m_1 = c/m_1$. The gold concentration was constant in all experiments (0.1 mM = 19.7 × 10^{-6} g·mL^{-1}), therefore, the number of SERS-active molecules in 1 mL of colloid is

$$N_R = N_1\times N = \frac{S}{S_1}\frac{c}{m_1} = \frac{S}{S_1}\frac{c}{\rho V} = \left(\frac{c}{S_1\rho}\right)\frac{S}{V} = K\frac{S}{V}, \quad (3)$$

where, for our comparative estimates, the K constant can be set to 1. Thus, under our experimental conditions, the number of molecules per particle is proportional to the ratio of its surface area to its volume.

It should be emphasized that our final Equation 3 involves only one experimental parameter, the particle surface-to-volume ratio (S/V), whereas other adsorption parameters and the number concentration of particles are not considered. This simple and important result is based on several simplifying assumptions. Our main assumption is that the number of SERS-active NBT molecules N_R is roughly proportional to the particle surface area. This assumption does not necessarily imply a monolayer or any specific arrangement of the adsorbed layer. The only requirement is that the total number of adsorbed SERS-active mole-

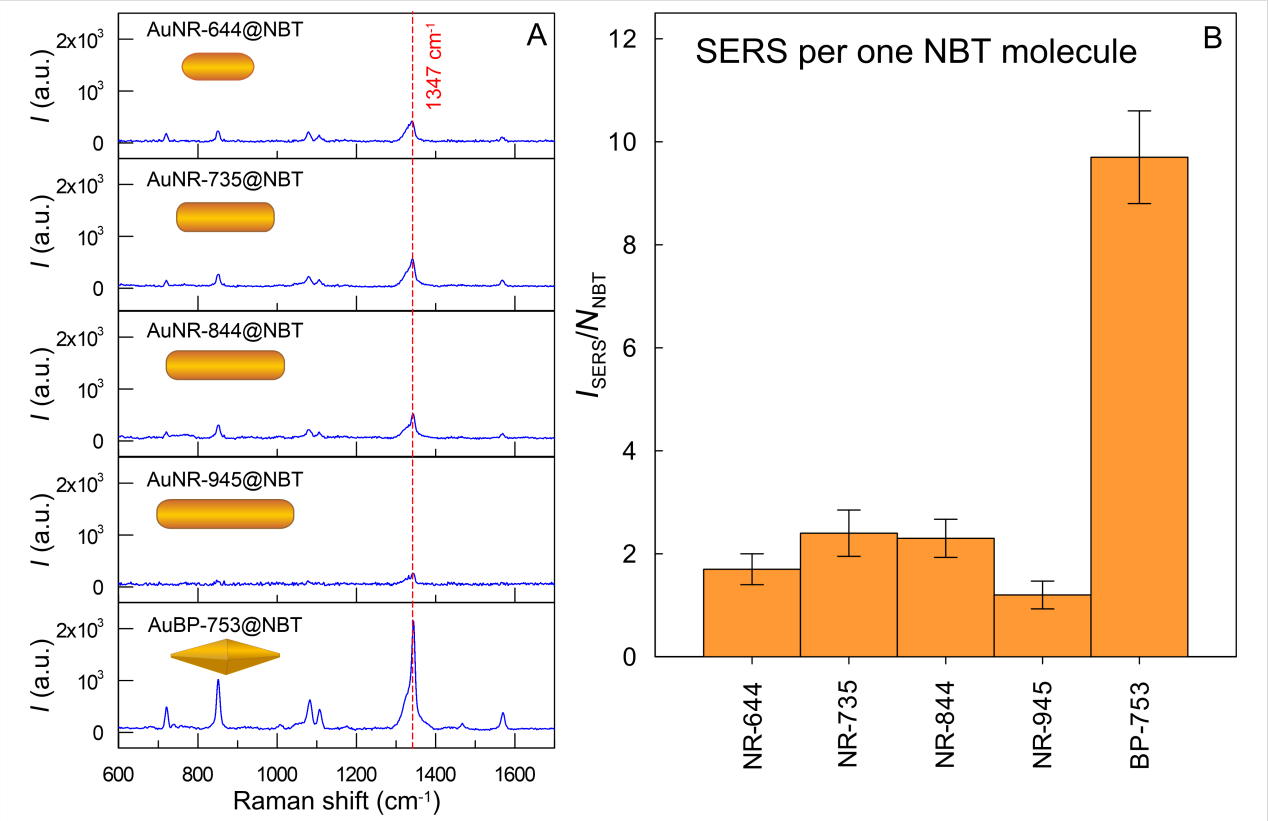


Figure 3: SERS spectra measured for functionalized samples of nanorods and bipyramids (A). The red dashed line indicates the most intense characteristic spectral line at 1347 cm^{-1}. Panel B shows the intensities (a. u.) per one adsorbed NBT molecule. For bipyramids, this parameter is almost four times higher than that for nanorods. In panel B, bars are SD values from three independent measurements.

cules be proportional to the particle surface area. In other words, the number of SERS-active molecules should be distinguished from the total number of adsorbed molecules. Indeed, as the local field decreases strongly with increasing distance from the particle surface and the SERS intensity is roughly proportional to the fourth power of the exciting field [60], only surface-adsorbed molecules make the main contribution to the detected SERS signal. This means that other adsorption parameters such as accessible surface area and adsorption affinity probably play a minor role. Moreover, an accurate experimental assessment of these parameters is not straightforward and would require a separate investigation. To the best of our knowledge, no studies of this type have been reported for gold nanobipyramids. In summary, we believe that our Equation 3 provides a reasonable estimate of the number of SERS-active molecules in comparative experiments with a fixed mass/volume concentration of particles having different sizes, shapes, and morphologies.

Figure 3B presents the normalized SERS intensity $I/(S/V)$ values, which, as explained above, are proportional to the average SERS intensity from a single adsorbed NBT molecule. In this sense, this parameter provides a comprehensive, averaged characteristic of the efficiency of a plasmonic nanoparticle as an SERS platform. As shown in the figure, the SERS efficiency of bipyramids is approximately four times higher than that of nanorods.

3 Analytical sensitivity of plasmon resonance to the dielectric environment

The sensitivity of PR to the dielectric environment is utilized for various analytical tasks aimed at determining target substances based on PR shifts [61]. Sensors based on this principle are somewhat similar to total internal reflection sensors, although the physical mechanism is entirely different in this case. In recent years, the most popular trend has been the development of fiber-optic sensors with a plasmonic nanostructure at the tip [29]. Theoretically, there are two approaches to estimating the analytical sensitivity of a PR sensor. In the most straightforward approach, the plasmonic response (e.g., the PR wavelength) is typically analyzed in a homogeneous dielectric medium with a varying refractive index (usually from 1.334 (water) to 1.6), and the sensitivity of different platforms is compared in terms of the derivative of the response with respect to the refractive index. For example, in the case of the PR wavelength, parameters such as $S_{PR} = \Delta\lambda_{PR}/\Delta n_m$ [62,63] are com-

pared. Within the dipole approximation, the polarizability of a particle of any shape and structure can be written as [52,64]:

$$\alpha = \frac{3V}{4\pi}\frac{\varepsilon_{av}-\varepsilon_m}{\varepsilon_{av}+\varphi\varepsilon_m} = a_0^3\frac{\varepsilon_{av}-\varepsilon_m}{\varepsilon_{av}+\varphi\varepsilon_m}, \quad (4)$$

where ε_{av} is the average dielectric permittivity of particles with a complex structure, calculated using the DEM. The function φ also depends on the shape and structure, and ε_m is the dielectric permittivity of a homogeneous medium. Here are three simple examples: (1) a metal sphere with the dielectric permittivity $\varepsilon_{metal} = \varepsilon(\omega)$ in a homogeneous medium with dielectric permittivity $\varepsilon_m(\omega)$: $\varepsilon_{av} = \varepsilon(\omega)$, $\varphi = 2$; (2) a metal ellipsoid with the dielectric permittivity $\varepsilon_{metal} = \varepsilon(\omega)$ in a homogeneous medium $\varepsilon_m(\omega)$: $\varepsilon_{av} = \varepsilon(\omega)$, $\varphi = L_{a,b,c}^{-1} - 1$, where $L_{a,b,c}$ are the geometrical depolarization factors along the axes a, b, and c, $\sum_{i=a,b,c} L_i = 1$. For a sphere $L_i = L = 1/3$; and (3) a two-layered sphere with a metal core $\varepsilon_{metal} = \varepsilon_1(\omega)$ covered by a dielectric shell of thickness s with a dielectric permittivity $\varepsilon_s = \varepsilon_2(\omega)$ in a homogeneous medium $\varepsilon_m(\omega)$:

$$\varepsilon_{av} = \varepsilon_2\frac{1+2f_{12}\alpha_{12}}{1-f_{12}\alpha_{12}},\ \varphi = 2, \quad (5)$$

where $\alpha_{12} = (\varepsilon_1 - \varepsilon_2)/(\varepsilon_1 + 2\varepsilon_2)$, $f_{12} = a_1^3/a_2^3 = a_1^3/(a_1+s)^3$. It follows from Equation 4 that the PR resonance condition reads:

$$\mathrm{Re}(\varepsilon_{av}) = -\varphi\varepsilon_m. \quad (6)$$

In the Drude approximation, the metal dielectric function is given by

$$\varepsilon(\omega) = \varepsilon_{ib}(\omega) - \frac{\omega_p^2}{\omega(\omega + i\gamma_b)}, \quad (7)$$

where $\varepsilon_{ib}(\omega)$ accounts for the contribution of interband transitions, ω_p is the bulk metal plasma frequency (for gold, $\hbar\omega_p \approx 9$ eV), and the damping constant γ_b corresponds to a bulk sample. It does not account for additional damping mechanisms [64]. Combining Equation 6 and Equation 7, we find the plasmon resonance wavelength [52,64]:

$$\lambda_{PR} = \lambda_p\left[\varepsilon_{ib} + \varepsilon_m\varphi\right]^{1/2}. \quad (8)$$

Using Equation 8, one can obtain a theoretical estimate of the sensitivity of PR to changes in the refractive index of the external medium in the form of universal relations:

$$S_{PR} = \frac{\Delta\lambda_{PR}}{\Delta n_m} = \varphi\frac{\lambda_p n_m}{\sqrt{\varepsilon_{ib} + \varphi n_m^2}}, \quad (9)$$

$$\frac{\Delta\lambda_{PR}}{\lambda_{PR}} = \frac{\Delta n_m}{n_m}\left(1 - \frac{\lambda_p^2}{\lambda_{PR}^2}\varepsilon_{ib}\right), \quad (10)$$

where $\lambda_p = 2\pi\omega_p/c$ is the plasma wavelength (for gold, $\lambda_p \approx 130$ nm), and c is the velocity of light in vacuum.

Equation 9 explains the theoretically obtained [62,63] and experimentally observed linear dependencies $\lambda_{PR} = f(n_m)$ with a constant coefficient S_{PR}, since n_m usually changes within a narrow range of 1.3 to 1.5 (for water–glycerol mixtures). In this case, according to Equation 10, the relative change $\Delta\lambda_{PR}/\lambda_{PR}$ turns out to be proportional to the relative change $\lambda_{PR} = f(n_m)$ with an accuracy of approximately a constant coefficient (for gold in water, it is approximately 0.5 [65]). Equations 9 and 10 also explain that the structure and shape of a particle decisively influence the angular slope of the dependence $\lambda_{PR} = f(n_m)$ through the parameter φ in Equation 9.

For the theoretical evaluation of the analytical sensitivity of a plasmonic sensor, one can also calculate the change in the plasmonic response resulting from the formation of a dielectric layer on the particle surface, for example, due to antigen–antibody interactions [66]. This formulation of the problem seems more justified from the perspective of modeling real experimental situations, where the process of analyte molecule adsorption on the surface of a plasmonic nanosensor is detected by the shift in plasmon resonance. This modeling process itself can be carried out in two variants, namely, (1) analysis of the PR shift as a function of shell thickness with a constant refractive index and (2) analysis of the PR shift as a function of the shell's refractive index at its constant nanometer-scale thickness. The real situation is most likely a combination of these two variants since, as the thickness of the adsorbed biopolymer layer increases, the volume fraction of the aqueous buffer (or other solvent) will decrease. Below, we present comparative data for nanorods and BPs in a homogeneous, infinite medium and in a shell of variable thickness with a constant refractive index.

Figure 4 shows the dependence of the plasmon resonance wavelength shift $\Delta\lambda_{PR}$ on the refractive index of the external medium n_m for gold BPs and nanorods with a diameter of 15 nm and an aspect ratio of 3. For the bipyramids, calculations were performed using the 3D FEM COMSOL method under longitudinal excitation of the particles by an electric field. For the

nanorods, the calculation was performed on randomly oriented nanoparticles using the T-matrix method. We also performed an approximate averaging over the orientations of the bipyramids and confirmed that the result differs only slightly from that presented in Figure 4.

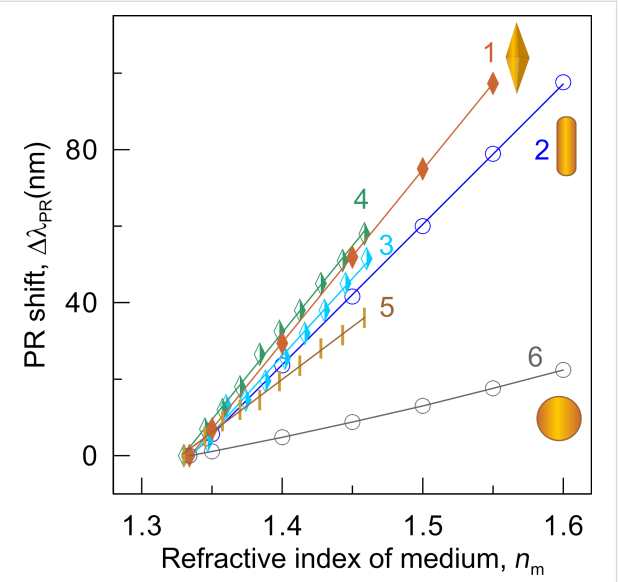


Figure 4: Dependence of the plasmon resonance wavelength shift $\Delta\lambda_{PR}$ on the refractive index of the external medium (n_m). Calculation for gold BPs (1, COMSOL) and nanorods (2, T-matrix method) with a diameter of 15 nm and an aspect ratio of 3. Experimental points 3 and 4 for gold BPs are reproduced from works by Chen et al. [28] (AR = 3.8) and by Fang et al. [30] (AR = 3.3), respectively. Experimental points (5) for gold nanorods with $AR_{TEM} \approx 4.8$ ($AR_{PR} = 4.2$) are reproduced from Fang et al. [30]. For comparison, the linear dependence (6) according to Mie theory for spheres with an equivolume diameter of 24 nm is also shown.

From Figure 4, it follows that for nanoparticles with identical geometric parameters, the analytical sensitivity of bipyramids, measured by the plasmon resonance shift, is higher than that of nanorods. It should be noted that both the FEM (COMSOL) and T-matrix methods yield identical results for axially symmetric particles such as nanorods (see, e.g., Figure S6 in Supporting Information File 1). Therefore, the difference in the slopes of lines 1 and 2 in Figure 3 arises from the distinct plasmonic sensitivities of the two particle types, rather than from any computational artifacts.

Additional confirmation of the strong influence of the particle is provided by line (6), obtained from Mie theory for spheres of equivalent diameter. For qualitative comparison with experimental data, we have reproduced in Figure 4 data from the work of Chen et al. [28] for bipyramids with an aspect ratio of AR = 3.8 and from Fang et al. [30] for bipyramids with an aspect ratio of AR = 3.3. The last data are in close agreement with our simulations. It should also be noted that the particle sizes and tip rounding radii in the Chen et al. [28] samples were significantly larger than those used in our calculation for dependence (1); therefore, this comparison should be considered qualitative. This is precisely why the experimental line (4) for bipyramids with an aspect ratio of 3.8 lies below the theoretical line for an aspect ratio of 3 and the experimental line (4) by Fang et al. [30] for an aspect ratio of 3.3. The experimental data [30] for nanorods confirm a lower angular slope than that for BPs. In general, we conclude that the theoretical estimates of the angular slope S_{PR} for BPs and nanorods are in qualitative agreement with the experimental data.

Now, let us discuss the data for the case where the analyte forms a shell on the surface of a plasmonic nanoparticle. Figure 5A shows the dependence of the plasmon resonance wavelength shift $\Delta\lambda_{PR}$ on the shell thickness s (curves 1, 2) or its volume fraction $g = V_s/(V_s + V_{Au})$ (curves 3, 4) for bipyramids, modeled as an inscribed bicone [38] with an aspect ratio of 3. For comparison, two particle diameters of 15 and 30 nm were chosen, which are close to the experimental conditions [38], with a typical refractive index of 1.5 for many biopolymers or silicon dioxide [67].

From plots 1 and 2, it can be seen that the main sharp plasmon resonance shift occurs when the shell thickness changes from 0 to 5–10 nm, at which point the shell volume fraction approaches 75–80%. Such a sharp dependence of PR shift on the shell thickness is closely related the strong localization of plasmonic field as explained below in Section 4. Figure 5B shows the dependencies of the plasmon resonance wavelength shift on the refractive index of the shell for two particle diameters, 15 and 30 nm, at shell thicknesses of 5 and 10 nm, which also differ by a factor of two. As shown, lines 1 and 2 are practically indistinguishable, which is explained by the approximately equal shell volume fractions in both nanocomposites. As mentioned above, increasing the shell thickness to that of an infinite homogeneous dielectric medium somewhat increases the angular slope of dependence (3). Still, it does not change the fundamental essence of the matter. Thus, the formation of dielectric analyte shells with a thickness of about 10 nm is essentially equivalent to the plasmon resonance shift when placed in an infinite analyte medium.

4 Physical mechanisms underlying the superior SERS and analytical responses of bipyramids over nanorods

The data presented in Sections 2 and 3, together with available literature data, indicate the key influence of particle shape and morphology (all other things being equal) on their SERS and analytical responses. In particular, the well-known decrease in the SERS signal from spherical particles of equal volume com-

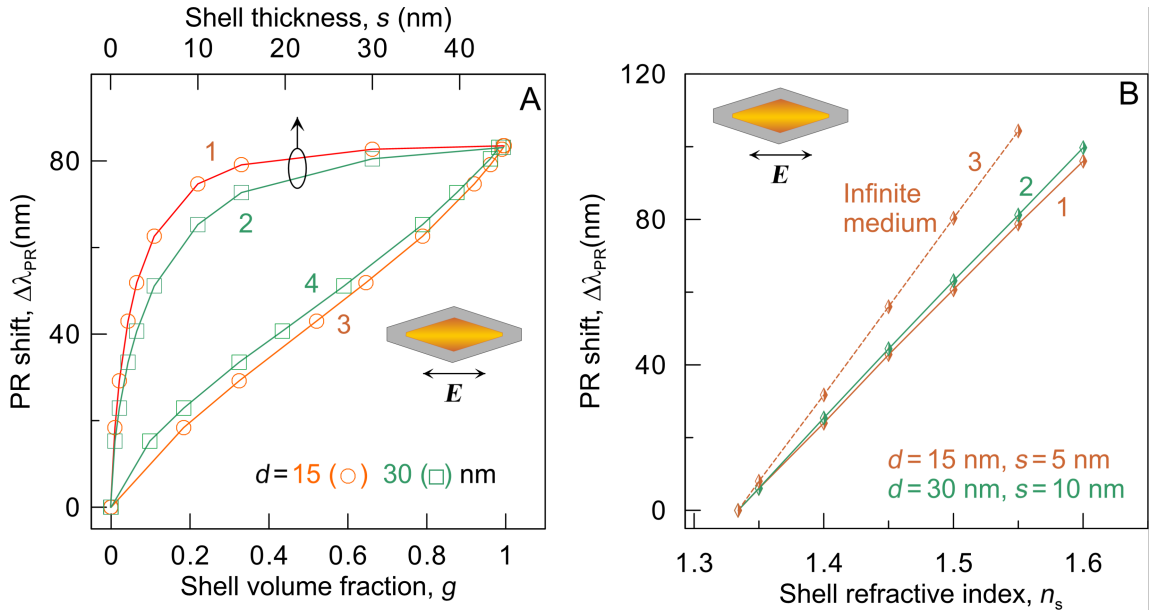


Figure 5: (A) Dependence of the plasmon resonance wavelength shift $\Delta\lambda_{PR}$ on shell thickness (1, 2) or its volume fraction (3, 4). Calculation based on the analytical MEM theory for composite nanoparticles consisting of gold bicones with diameters of 15 nm (1, 3) and 30 nm (2, 4), an aspect ratio AR = 3, and a dielectric shell thickness s ranging from zero to 45 nm. The refractive index of the shell is 1.5. (B) Dependence of the plasmon resonance wavelength shift $\Delta\lambda_{PR}$ of gold bicones on the refractive index of a dielectric shell with thicknesses of 5 nm (1) and 10 nm (2). For comparison, the dashed line (3) shows the dependence of the plasmon shift (1) for a particle in an infinite homogeneous medium. Particle diameters are 15 nm (1) and 30 nm (2), and the axial ratio is 3.

pared with nanorods [2], as well as the small plasmon resonance shift for equal-volume spheres (curve 6 in Figure 4), suggest that the underlying physical mechanism of the observed differences in SERS and analytical sensitivity is related to the features of particle shape and morphology, which lead to different local field distributions near the nanoparticle surface where the reporter molecules are located [2] (Figure 6).

To quantitatively assess the SERS efficiency of particles with different morphologies, theoretical estimates of the average fourth power of the local field amplitude near the particles $\langle|E(\omega)|^4\rangle$ are often used, or a slightly more rigorous estimate $\langle|E(\omega_L)|^2|E(\omega_R)|^2\rangle$ that accounts for the difference between the laser, ω_L, and Raman, ω_R, frequencies [68]. Here, we define two average quantities

$$\left\langle\left|E\left(\lambda_{PR}\right)\right|\right\rangle=\frac{1}{S}\int_S\left|E\left(\lambda_{PR}\right)/E_0\right|\mathrm{d}S, \tag{11}$$

$$\mathrm{EF}=\left\langle\left|E\left(\lambda_{PR}\right)\right|^4\right\rangle=\frac{1}{S}\int_S\left|E\left(\lambda_{PR}\right)/E_0\right|^4\mathrm{d}S, \tag{12}$$

where the integral is taken over the outer particle surface. The first integral provides a straightforward averaged estimate of the field on the surface near the particle, while the second integral gives an approximate average estimate of the plasmonic enhancement factor (EF) for the SERS signal. A more accurate

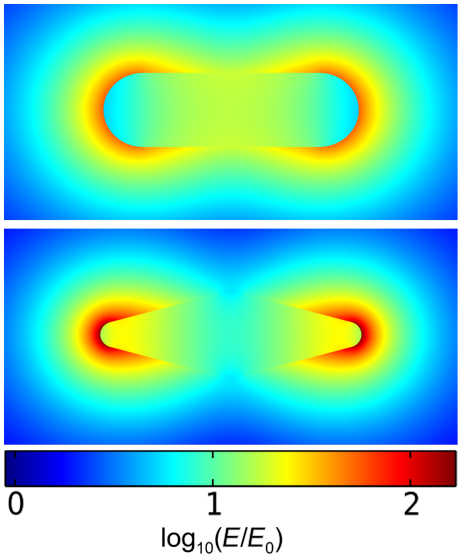


Figure 6: Calculated distribution of the logarithm of the field modulus ($\log_{10}|E|/|E_0|$) around the particle in water at the plasmon resonance wavelength for nanorods (top) and nano-bipyramids BP (bottom). The particle parameters correspond to the experimental ones (Table 1). The numbers on the color scale correspond to an order-of-magnitude change in the local field amplitude.

estimate of EF would also need to include the surface density of SERS-active molecules (with normalization $(1/S)\int_S n(S)\mathrm{d}S = 1$) and the difference between the Raman and laser frequencies:

$$\mathrm{EF} = \frac{1}{S}\int_S \left\langle \left|E(\omega_\mathrm{L})\right|^2 \left|E(\omega_\mathrm{R})\right|^2 \right\rangle \mathrm{n}(S)\,\mathrm{d}S. \qquad (13)$$

A detailed analysis of the theoretical SERS enhancement factor is given in [69]. Table 2 summarizes the average local field parameters for nanorods and bipyramids with sizes and shapes close to our experimental samples particles NR-735 and BP-753. The calculation details are given in Supporting Information File 1. Note the excellent agreement between calculated and measured PR wavelength.

Table 2: The local field parameters of nanorods NR-735 and bipyramids BP-753 at longitudinal excitation. Calculations by COMSOL for the normalized incident field at theoretical plasmon resonance wavelengths λ_{PR}. The angle bracket designate the averaging over the particle surface.

Sample	λ_{PR} (nm)	S/V (nm^{-1})	$\lvert\boldsymbol{E}\rvert_{max}$	$\langle\lvert\boldsymbol{E}\rvert\rangle_S$	$\langle\lvert\boldsymbol{E}\rvert^4\rangle_S \times 10^{-6}$
NR-735	740	0.235	50.2	25.9	1.91
BP-753	756	0.222	157	31.4	19.8

According to Table 2, the nanorods and bipyramid surfaces are similar, but the SERS enhancement factor of bipyramids is ten times higher. Experimentally (Figure 3), we obtained a much smaller enhancement ratio of about 4. As it has been explained in Section 2 and during derivation of Equation 3, this difference originates from a simplified estimation by Equation 13, which does not take into account many factors including the adsorption accessibility, affinity, and resulting surface density distributions of Raman NBT molecules. Obviously, the purely electromagnetic EF (Equation 12) overestimates the expected experimental parameter. Nevertheless, the simplified electromagnetic calculations by Equation 12 confirm the superior SERS efficiency of bipyramids compared to that of nanorods.

From Figure 4A, it follows that for nanoparticles with identical geometric parameters, the analytical sensitivity of bipyramids, measured by the plasmon resonance shift, is higher than that of nanorods. From a physical standpoint, this difference can be explained by the strong field localization near the vertices of the bipyramid (Figure 4B) and the resulting more substantial change in the dipole moment upon variation of the external refractive index compared to nanorods (Figure 4C). Qualitatively, the modulus of the local field near the bipyramid vertices is approximately an order of magnitude greater than the field near the ends of the nanorods. In accordance with the field distribution shown in Figure 6, this shell region precisely falls within the "hottest" area of the local electric field. Further increase in shell thickness has a smaller effect on the plasmon shift, which essentially becomes close to the PR shift in an infinite dielectric medium with the shell's refractive index (cf. dependencies 1 and 3 in Figure 5B). Interestingly, the average values of the local field modulus at the particle surface are similar for both particle types. This implies that the plasmonic shift induced by thin shell formation is not linearly dependent on the near field.

5 Comparison of thermoplasmonic properties for gold nanorods and nanobipyramids

To compare the efficiency of converting laser radiation into heat, an experiment was conducted (Figure 7A) comparing the

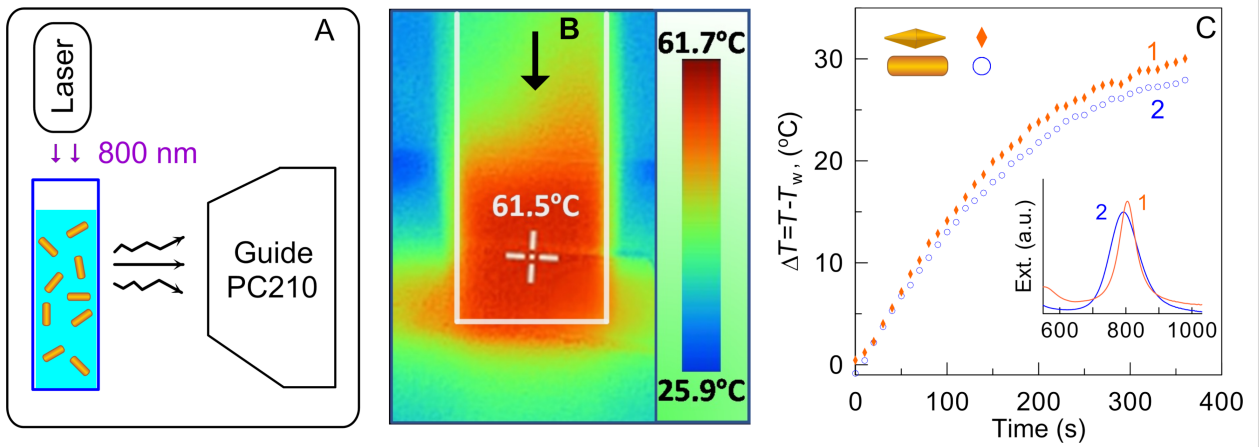


Figure 7: Schematic of irradiation and recording (A), temperature distribution (B) in a cuvette with an aqueous suspension, and temporal dependencies of the temperature difference between nanobipyramid suspension (1) and nanorod suspension (2) and water temperature ($\Delta T = T - T_w$) under identical irradiation conditions (C). The suspension volume in a 1 × 1 cm cuvette is 1 mL; the arrow in panel B indicates the direction of irradiation. The inset in panel C shows the extinction spectra of nanobipyramids (1) and nanorods (2) with equal extinction at 800 nm.

heating of gold BPs and nanorods with equal extinction at 800 nm, a wavelength close to the plasmon resonance wavelength of both nanoparticle types. The concentration of nanorods was 0.062 mM (12 μg·mL^{-1}), determined by absorbance at 400 nm. A 2 W laser with a wavelength of 800 nm was used for irradiation; the intensity of the expanded beam at the cuvette entrance was approximately 290 mW·cm^{-2}. Irradiation was performed from above into a 1 × 1 cm cuvette containing 1 mL of suspension, so the optical path length from the top to the bottom of the cuvette was 1 cm. The temperature distribution (Figure 7B) was recorded from the side using a thermal imager (Figure 7A). Irradiation and temperature measurement lasted about 6 min. Figure 7C shows the dependencies of the temperature increment (relative to the water temperature under the same irradiation conditions) on the irradiation time. It can be seen that after 5–6 min of irradiation, the temperature increment reaches an approximately steady-state value of around 30 °C. Although the heating kinetic curves are generally similar, we observe slightly higher efficiency for gold bipyramids, in agreement with the theoretical estimate of the Q_{abs}/R_{ev} ratio in the last column of Table 1. Thus, theoretical and experimental data show that, despite the smaller metal volume per particle, the photothermal efficiency of bipyramids is of the same order (or even slightly higher) as that of widely used nanorods.

6 Comparison of the photothermal killing of bacteria

For plasmonic photothermal therapy experiments with bacteria and nanoparticles, cells were mixed with nanoparticles in a 1:1 ratio, incubated for 15 min, and irradiated with a laser for 10 min. Four controls were used in the experiments, namely, (1) native bacteria without any treatment (B Cont), (2) bacteria without particles irradiated with the laser (B-Part+L), (3) bacteria with nanorods without laser irradiation (B+NR-L), and (4) bacteria with nanobipyramids without laser irradiation (B+BP-L). In the two positive experiments, that is, (5) (B+NR+L) and (6) (B+BP+L), bacteria were incubated with nanoparticles for 15 min, then irradiated with a laser intensity of 290 mW·cm^{-2} for 10 min. All experiments were conducted using a 96-well plate. Cell viability was assessed using the standard Alamar Blue test [57]. For this, 5 μL of resazurin was added to each 200 μL sample, and the mixture was incubated in a thermal chamber at 37 °C for 1 h. The results are presented in Figure 8 and Table 3. From the presented data, it can be seen that both types of nanoparticles are effective thermosensitizers, causing complete bacterial death after 10 min of irradiation at a very low intensity of about 0.3 W·cm^{-2}, which is an order of magnitude lower than the intensities typically used for photothermal therapy (2 W·cm^{-2}). A small 10% reduction in bacterial viability without laser irradiation could be explained by the possible contribution of residual CTAB/CTAC toxicity.

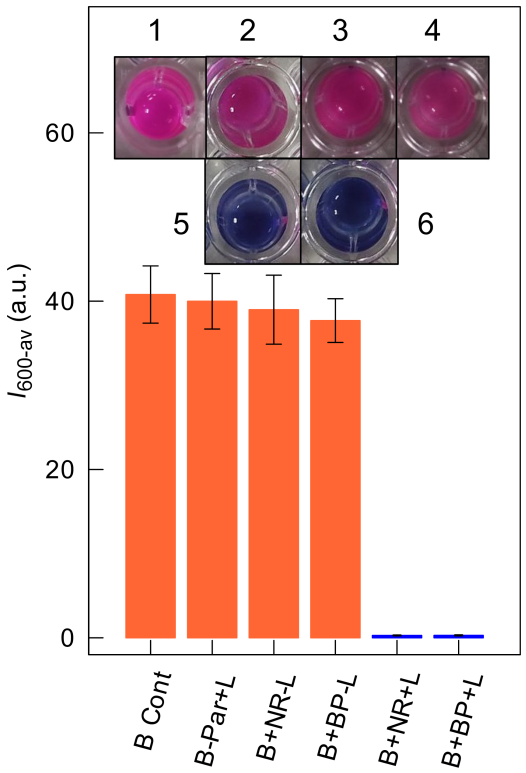


Figure 8: Photograph of six plate wells after the Alamar Blue test. The numbers correspond to the designations of controls and experiments as per the text: 1 – B Cont, 2 – B-Part+L, 3 – B+NR-L, 4 – B+BP-L, 5 – B+NR+L, and 6 – B+BP+L. Below is a histogram of the average luminescence intensity in the 590–610 nm range with excitation at a wavelength of 530 nm.

Table 3: Fluorescence intensities of the samples at 600 nm and assessment of cell viability.

Sample	Intensity I_{600} (a.u.)	Cell viability, %
1 – B Control	44.6	100
2 – B-Part+L	43.5	97.5
3 – B+NR-L	40.5	90.7
4 – B+BP-L	40.1	90
5 – B+NR+L	0.30	0.7
6 – B+BP+L	0.26	0.6

In conclusion to this section, it should be noted that, in addition to the thermal effect, nanoparticles can be potentially toxic [70] at high concentrations. Toxicity of gold nanoparticles was observed only in in vivo experiments at small sizes (2–5 nm), high concentrations, and in cases where cellular uptake was observed [71]. Toxicity of gold nanorods is also mainly manifested in in vivo experiments [72], and for nanorods, their toxicity is determined primarily not by size or shape, but by surface chemistry. First and foremost, the potential source of toxicity is the toxic surfactant stabilizer CTAB. In experiments with bacterial cells, cellular uptake of particles is not observed due to the

dense cell wall and the presence of an extracellular polymeric component. This is also consistent with our experiments, because in the control with the addition of nanoparticles but without laser heating, no reduction in cell viability was observed. The main effect is cellular adhesion of gold nanoparticles on the bacterial surface [73] rather than bacterial uptake. Therefore, the primary damaging mechanism in experiments with bacteria is precisely local heating of cells adsorbed on their surface.

Conclusion

In this work, we have presented experimental and theoretical data comparing several important plasmonic parameters of the most popular anisotropic particles, gold nanorods, and the less familiar, yet in our view, quite promising plasmonic gold bipyramid nanoparticles. Our goal was to draw researchers' attention to this new class of anisotropic plasmonic nanoparticles with a tunable plasmon resonance spanning 600–1200 nm. Due to their strong shape anisotropy, bipyramids generate a strong local field near their sharp tips when excited at their plasmon resonance wavelength. Such localization has important implications for potential biomedical applications. First, Raman reporter molecules located near these local-field hot spots emit a stronger SERS signal than conventional nanorods under the same conditions. Second, bipyramids exhibit greater analytical sensitivity to global or local dielectric environmental changes, leading to a larger plasmon resonance shift. Third, it can be expected that bipyramids will be promising nanoparticles as a plasmonic platform for bioimaging. Finally, thanks to their high absorption per unit mass of metal, bipyramids show promise as photothermal sensitizers that efficiently generate heat upon laser irradiation.

Supporting Information

Section S1. Additional TEM images and particle statistics; Section S2. Comparison of extinction spectra calculated by COMSOL and the T-matrix method; Section S3. Calculations of the average near field parameters.

Supporting Information File 1

Additional experimental and calculation data.
[https://www.beilstein-journals.org/bjnano/content/supplementary/2190-4286-17-80-S1.pdf]

Funding

The study of the photothermal properties of bipyramids and plasmon resonance-mediated bacterial killing was supported by the Russian Science Foundation grant no. 24-65-00015, https://rscf.ru/project/24-65-00015. The synthesis of nanoparticles, their characterization, SERS investigations, and theoretical analysis were performed within the framework of the state assignment of the Ministry of Science and Higher Education of the Russian Federation for the Federal Research Center "Saratov Scientific Center of the Russian Academy of Sciences", theme no. 121031700141-6.

Compliance with Ethical Standards

This work does not involve studies with human participants or animals.

Conflict of Interest

The authors of this work declare that they have no conflicts of interest.

Declaration of Generative AI and AI-Assisted Technologies

During the preparation of this work, the authors used DeepSeek v3 and Grammarly to check the English. After using these tools, the authors reviewed and edited the content as needed and take full responsibility for the content of the published article.

Author Contributions

Andrey M. Burov: investigation; methodology; visualization; writing – review & editing. Sergey V. Zarkov: investigation; software; visualization. Arina V. Drozd: investigation. Igor V. Borisov: investigation; methodology. Elena G. Zavyalova: funding acquisition; project administration. Nikolai G. Khlebtsov: conceptualization; data curation; formal analysis; methodology; project administration; software; supervision; visualization; writing – original draft; writing – review & editing.

ORCID® iDs

Andrey M. Burov - https://orcid.org/0000-0002-0469-8392
Arina V. Drozd - https://orcid.org/0009-0003-7675-1126
Igor V. Borisov - https://orcid.org/0000-0001-5181-1653
Nikolai G. Khlebtsov - https://orcid.org/0000-0002-2055-7784

Data Availability Statement

All modeling and experimental data are available from the authors upon request.

Preprint

A non-peer-reviewed version of this article has been previously published as a preprint: https://arxiv.org/abs/2605.20582

References

1. Liz-Marzán, L. M.; Grzelczak, M. *Science* **2017,** *356,* 1120–1121. doi:10.1126/science.aam8774
2. Reguera, J.; Langer, J.; Jiménez de Aberasturi, D.; Liz-Marzán, L. M. *Chem. Soc. Rev.* **2017,** *46,* 3866–3885. doi:10.1039/c7cs00158d

3. Zhuo, X.; Kumar, V.; Chow, T. H.; Wang, J.; Liz-Marzán, L. M. Synthesis and Functionalization of Anisotropic Silver Nanoparticles. In *Synthesis and Functionalization of Anisotropic Silver Nanoparticles;* Wang, J., Ed.; World Scientific Series in Nanoscience and Nanotechnology, Vol. 22; World Scientific, 2022; pp 349–396. doi:10.1142/9789811235221_0008
4. Ortiz-Castillo, J. E.; Gallo-Villanueva, R. C.; Madou, M. J.; Perez-Gonzalez, V. H. *Coord. Chem. Rev.* **2020,** *425,* 213489. doi:10.1016/j.ccr.2020.213489
5. Nguyen, Q. N.; Wang, C.; Shang, Y.; Janssen, A.; Xia, Y. *Chem. Rev.* **2023,** *123,* 3693–3760. doi:10.1021/acs.chemrev.2c00468
6. Khlebtsov, N. G.; Dykman, L. A.; Khlebtsov, B. N. *Russ. Chem. Rev.* **2022,** *91,* RCR5058. doi:10.57634/rcr5058
7. Jain, P. K.; Lee, K. S.; El-Sayed, I. H.; El-Sayed, M. A. *J. Phys. Chem. B* **2006,** *110,* 7238–7248. doi:10.1021/jp057170o
8. Lu, Z.; Ji, J.; Ye, H.; Zhang, H.; Zhang, S.; Xu, H. *Nat. Commun.* **2024,** *15,* 8803. doi:10.1038/s41467-024-53210-8
9. Liz-Marzán, L., Ed. *Colloidal Synthesis of Plasmonic Nanometals;* Jenny Stanford Publishing: New York City, NY, U.S.A., 2020. doi:10.1201/9780429295188
10. Xia, Y.; Li, W.; Cobley, C. M.; Chen, J.; Xia, X.; Zhang, Q.; Yang, M.; Cho, E. C.; Brown, P. K. *Acc. Chem. Res.* **2011,** *44,* 914–924. doi:10.1021/ar200061q
11. Panfilova, E. V.; Khlebtsov, B. N.; Khlebtsov, N. G. *Colloid J.* **2013,** *75,* 333–338. doi:10.1134/s1061933x13030149
12. Zhang, F.; Xu, L.; Wang, Y.; Wang, P. *Mater. Today Bio* **2025,** *33,* 102022. doi:10.1016/j.mtbio.2025.102022
13. Wang, J.; Fang, W.; Liu, H. *ChemPlusChem* **2023,** *88,* e202200464. doi:10.1002/cplu.202200464
14. Scarabelli, L.; Sun, M.; Zhuo, X.; Yoo, S.; Millstone, J. E.; Jones, M. R.; Liz-Marzán, L. M. *Chem. Rev.* **2023,** *123,* 3493–3542. doi:10.1021/acs.chemrev.3c00033
15. Jin, X.; Khlebtsov, B. N.; Khanadeev, V. A.; Khlebtsov, N. G.; Ye, J. *ACS Appl. Mater. Interfaces* **2017,** *9,* 30387–30397. doi:10.1021/acsami.7b08733
16. Khlebtsov, N. G.; Lin, L.; Khlebtsov, B. N.; Ye, J. *Theranostics* **2020,** *10,* 2067–2094. doi:10.7150/thno.39968
17. Zheng, J.; Cheng, X.; Zhang, H.; Bai, X.; Ai, R.; Shao, L.; Wang, J. *Chem. Rev.* **2021,** *121,* 13342–13453. doi:10.1021/acs.chemrev.1c00422
18. Vigderman, L.; Khanal, B. P.; Zubarev, E. R. *Adv. Mater. (Weinheim, Ger.)* **2012,** *24,* 4811–4841. doi:10.1002/adma.201201690
19. Lohse, S. E.; Murphy, C. J. *Chem. Mater.* **2013,** *25,* 1250–1261. doi:10.1021/cm303708p
20. Requejo, K. I.; Liopo, A. V.; Zubarev, E. R. *Langmuir* **2020,** *36,* 3758–3769. doi:10.1021/acs.langmuir.0c00302
21. Dement'eva, O. V.; Kartseva, M. E. *Colloid J.* **2023,** *85,* 500–519. doi:10.1134/s1061933x23700187
22. Chow, T. H.; Li, N.; Bai, X.; Zhuo, X.; Shao, L.; Wang, J. *Acc. Chem. Res.* **2019,** *52,* 2136–2146. doi:10.1021/acs.accounts.9b00230
23. Montaño-Priede, J. L.; Rao, A.; Sánchez-Iglesias, A.; Grzelczak, M. *Sci. Adv.* **2025,** *11,* eadx2299. doi:10.1126/sciadv.adx2299
24. Naik, A. M.; Sánchez-Iglesias, A.; Montaño-Priede, J. L.; D'souza, N. M.; Sancho-Parramon, J.; Mezzasalma, S. A.; Rao, A.; Grzelczak, M. *Adv. Opt. Mater.* **2025,** *13,* e01006. doi:10.1002/adom.202501006
25. Campu, A.; Brezestean, I. A.; Tripon, S.-C.; Astilean, S.; Focsan, M. *J. Mater. Chem. C* **2025,** *13,* 16378–16386. doi:10.1039/d5tc01502b
26. Alba-Molina, D.; Cano, M.; Blanco-Blanco, M.; Ortega-Llamas, L.; Jiménez-Gómez, Y.; Gonzalez-Lopez, A.; Perez-Perdomo, M.; Camacho, L.; Giner-Casares, J. J.; Gonzalez-Andrades, M. *J. Mater. Chem. B* **2025,** *13,* 3000–3010. doi:10.1039/d4tb02688h
27. Martín-Sánchez, C.; Sánchez-Iglesias, A.; Barreda-Argüeso, J. A.; Itié, J.-P.; Chauvigne, P.; Liz-Marzán, L. M.; Rodríguez, F. *Nano Lett.* **2025,** *25,* 3588–3596. doi:10.1021/acs.nanolett.4c06473
28. Chen, H.; Kou, X.; Yang, Z.; Ni, W.; Wang, J. *Langmuir* **2008,** *24,* 5233–5237. doi:10.1021/la800305j
29. Lu, M.; Wang, C.; Fan, R.; Lin, M.; Guang, J.; Peng, W. *Photonic Sens.* **2024,** *14,* 240202. doi:10.1007/s13320-024-0709-1
30. Fang, C.; Zhao, G.; Xiao, Y.; Zhao, J.; Zhang, Z.; Geng, B. *Sci. Rep.* **2016,** *6,* 36706. doi:10.1038/srep36706
31. Lee, J.-H.; Gibson, K. J.; Chen, G.; Weizmann, Y. *Nat. Commun.* **2015,** *6,* 7571. doi:10.1038/ncomms8571
32. Chateau, D.; Liotta, A.; Vadcard, F.; Navarro, J. R. G.; Chaput, F.; Lermé, J.; Lerouge, F.; Parola, S. *Nanoscale* **2015,** *7,* 1934–1943. doi:10.1039/c4nr06323f
33. Chateau, D.; Desert, A.; Lerouge, F.; Landaburu, G.; Santucci, S.; Parola, S. *ACS Appl. Mater. Interfaces* **2019,** *11,* 39068–39076. doi:10.1021/acsami.9b12973
34. Nguyen, A. L.; Griffin, Q. J.; Wang, A.; Zou, S.; Jing, H. *J. Phys. Chem. C* **2025,** *129,* 4303–4312. doi:10.1021/acs.jpcc.4c08818
35. Sánchez-Iglesias, A.; Grzelczak, M. *Small* **2025,** *21,* 2407735. doi:10.1002/smll.202407735
36. Salsabiila, N.; Morsin, M.; Nafisah, S.; Razali, N. L.; Mahmud, F.; Tukiran, Z.; Omar, M. A. *J. Adv. Res. Appl. Mech.* **2025,** *127,* 100–119. doi:10.37934/aram.127.1.100119
37. Marcheselli, J.; Chateau, D.; Lerouge, F.; Baldeck, P.; Andraud, C.; Parola, S.; Baroni, S.; Corni, S.; Garavelli, M.; Rivalta, I. *J. Chem. Theory Comput.* **2020,** *16,* 3807–3815. doi:10.1021/acs.jctc.0c00269
38. Montaño-Priede, J. L.; Sánchez-Iglesias, A.; Mezzasalma, S. A.; Sancho-Parramon, J.; Grzelczak, M. *J. Phys. Chem. Lett.* **2024,** *15,* 3914–3922. doi:10.1021/acs.jpclett.4c00582
39. Khlebtsov, N. G.; Zarkov, S. V. *J. Phys. Chem. C* **2025,** *129,* 10958–10974. doi:10.1021/acs.jpcc.5c01652
40. Li, Q.; Zhuo, X.; Li, S.; Ruan, Q.; Xu, Q.-H.; Wang, J. *Adv. Opt. Mater.* **2015,** *3,* 801–812. doi:10.1002/adom.201400505
41. Qi, Y.; Xing, T.-y.; Zhao, J.; Weng, G.-j.; Li, J.-j.; Zhu, J.; Zhao, J.-w. *J. Alloys Compd.* **2019,** *776,* 934–947. doi:10.1016/j.jallcom.2018.10.321
42. Khanadeev, V. A.; Khlebtsov, N. G.; Burov, A. M.; Khlebtsov, B. N. *Colloid J.* **2015,** *77,* 652–660. doi:10.1134/s1061933x15050117
43. Ciracì, C.; Urzhumov, Y.; Smith, D. R. *Opt. Express* **2013,** *21,* 9397–9406. doi:10.1364/oe.21.009397
44. Khlebtsov, N. G.; Zarkov, S. V. *J. Phys. Chem. C* **2024,** *128,* 15029–15040. doi:10.1021/acs.jpcc.4c03126
45. Gladyshev, S.; Pashina, O.; Proskurin, A.; Nikolaeva, A.; Sadrieva, Z.; Petrov, M.; Bogdanov, A.; Frizyuk, K. *ACS Photonics* **2024,** *11,* 404–418. doi:10.1021/acsphotonics.3c01166
46. Khlebtsov, N. G.; Zarkov, S. V.; Khanadeev, V. A.; Avetisyan, Y. A. *Nanoscale* **2020,** *12,* 19963–19981. doi:10.1039/d0nr02531c
47. Olmon, R. L.; Slovick, B.; Johnson, T. W.; Shelton, D.; Oh, S.-H.; Boreman, G. D.; Raschke, M. B. *Phys. Rev. B* **2012,** *86,* 235147. doi:10.1103/physrevb.86.235147
48. Novo, C.; Gomez, D.; Perez-Juste, J.; Zhang, Z.; Petrova, H.; Reismann, M.; Mulvaney, P.; Hartland, G. V. *Phys. Chem. Chem. Phys.* **2006,** *8,* 3540–3546. doi:10.1039/b604856k

49. Khlebtsov, B.; Khanadeev, V.; Pylaev, T.; Khlebtsov, N. *J. Phys. Chem. C* **2011,** *115,* 6317–6323. doi:10.1021/jp2000078
50. Mosquera, J.; Wang, D.; Bals, S.; Liz-Marzán, L. M. *Acc. Chem. Res.* **2023,** *56,* 1204–1212. doi:10.1021/acs.accounts.3c00101
51. Yu, R.; Liz-Marzán, L. M.; García de Abajo, F. J. *Chem. Soc. Rev.* **2017,** *46,* 6710–6724. doi:10.1039/c6cs00919k
52. Khlebtsov, N. G. *J. Quant. Spectrosc. Radiat. Transfer* **2013,** *123,* 184–217. doi:10.1016/j.jqsrt.2012.12.027
53. Vigderman, L.; Zubarev, E. R. *Chem. Mater.* **2013,** *25,* 1450–1457. doi:10.1021/cm303661d
54. Lohse, S. E.; Burrows, N. D.; Scarabelli, L.; Liz-Marzán, L. M.; Murphy, C. J. *Chem. Mater.* **2014,** *26,* 34–43. doi:10.1021/cm402384j
55. Tong, W.; Walsh, M. J.; Mulvaney, P.; Etheridge, J.; Funston, A. M. *J. Phys. Chem. C* **2017,** *121,* 3549–3559. doi:10.1021/acs.jpcc.6b10343
56. Khlebtsov, B. N.; Burov, A. M.; Zarkov, S. V.; Khlebtsov, N. G. *Phys. Chem. Chem. Phys.* **2023,** *25,* 30903–30913. doi:10.1039/d3cp04541b
57. Eremeev, A. V.; Pikina, A. S.; Vladimirova, T. V.; Bogomazova, A. N. *Genes Cells* **2023,** *18,* 5–21. doi:10.23868/gc312198
58. Khlebtsov, N. G.; Khlebtsov, B. N.; Kryuchkova, E. V.; Zarkov, S. V.; Burov, A. M. *J. Phys. Chem. C* **2022,** *126,* 19268–19276. doi:10.1021/acs.jpcc.2c05843
59. Engel, A.; Drault, F.; Demoustier-Champagne, S. M.; Hermans, S. *Langmuir* **2025,** *41,* 15805–15818. doi:10.1021/acs.langmuir.5c00326
60. Etchegoin, P. G.; Le Ru, E. C. *Phys. Chem. Chem. Phys.* **2008,** *10,* 6079–6089. doi:10.1039/b809196j
61. Mayer, K. M.; Hafner, J. H. *Chem. Rev.* **2011,** *111,* 3828–3857. doi:10.1021/cr100313v
62. Miller, M. M.; Lazarides, A. A. *J. Phys. Chem. B* **2005,** *109,* 21556–21565. doi:10.1021/jp054227y
63. Luo, X.; Qiao, L.; Xia, Z.; Yu, J.; Wang, X.; Huang, J.; Shu, C.; Wu, C.; He, Y. *Langmuir* **2022,** *38,* 6454–6463. doi:10.1021/acs.langmuir.2c00663
64. Khlebtsov, N. G. *Quantum Electron.* **2008,** *38,* 504. doi:10.1070/qe2008v038n06abeh013829
65. Khlebtsov, B. N.; Khanadeyev, V. A.; Ye, J.; Mackowski, D. W.; Borghs, G.; Khlebtsov, N. G. *Phys. Rev. B* **2008,** *77,* 035440. doi:10.1103/physrevb.77.035440
66. Khlebtsov, N. G.; Dykman, L. A.; Bogatyrev, V. A.; Khlebtsov, B. N. *Colloid J.* **2003,** *65,* 508–518. doi:10.1023/a:1025137322720
67. Khlebtsov, B. N.; Khanadeev, V. A.; Khlebtsov, N. G. *Langmuir* **2008,** *24,* 8964–8970. doi:10.1021/la8010053
68. Khlebtsov, B. N.; Khanadeev, V. A.; Burov, A. M.; Le Ru, E. C.; Khlebtsov, N. G. *J. Phys. Chem. C* **2020,** *124,* 10647–10658. doi:10.1021/acs.jpcc.0c00991
69. Le Ru, E. C.; Blackie, E.; Meyer, M.; Etchegoin, P. G. *J. Phys. Chem. C* **2007,** *111,* 13794–13803. doi:10.1021/jp0687908
70. Khlebtsov, N.; Dykman, L. *Chem. Soc. Rev.* **2011,** *40,* 1647–1671. doi:10.1039/c0cs00018c
71. Dykman, L. A.; Khlebtsov, N. G. *Chem. Rev.* **2014,** *114,* 1258–1288. doi:10.1021/cr300441a
72. AlGhosain, H. M.; Nie, J.; Liu, T.; Lee, J. *Toxicol. Res. (Cham, Switz.)* **2025,** *41,* 489–502. doi:10.1007/s43188-025-00295-y
73. Dykman, L.; Khlebtsov, N. *Chem. Soc. Rev.* **2012,** *41,* 2256–2282. doi:10.1039/c1cs15166e

License and Terms

This is an open access article licensed under the terms of the Beilstein-Institut Open Access License Agreement (https://www.beilstein-journals.org/bjnano/terms), which is identical to the Creative Commons Attribution 4.0 International License (https://creativecommons.org/licenses/by/4.0). The reuse of material under this license requires that the author(s), source and license are credited. Third-party material in this article could be subject to other licenses (typically indicated in the credit line), and in this case, users are required to obtain permission from the license holder to reuse the material.

The definitive version of this article is the electronic one which can be found at:
https://doi.org/10.3762/bjnano.17.80